8-2015

Fluorochlorozirconate Glass Ceramics for Photovoltaic and Computed Radiography Applications

Russell Lee Leonard
University of Tennessee - Knoxville, rleonard@utsi.edu

To the Graduate Council:

I am submitting herewith a dissertation written by Russell Lee Leonard entitled "Fluorochlorozirconate Glass Ceramics for Photovoltaic and Computed Radiography Applications." I have examined the final electronic copy of this dissertation for form and content and recommend that it be accepted in partial fulfillment of the requirements for the degree of Doctor of Philosophy, with a major in Biomedical Engineering.

Jacqueline A. Johnson, Major Professor

We have read this dissertation and recommend its acceptance:

Justin S. Baba, Laurence F. Miller, Charles L. Melcher

Accepted for the Council:
Dixie L. Thompson

Vice Provost and Dean of the Graduate School

(Original signatures are on file with official student records.)

Fluorochlorozirconate Glass Ceramics for Photovoltaic and Computed Radiography Applications

A Dissertation Presented for the

Doctor of Philosophy

Degree

The University of Tennessee, Knoxville

Russell Lee Leonard

August 2015

DEDICATION

I dedicate this work to my beloved wife, Coral.

ACKNOWLEDGEMENTS

I would like to give special thanks to my academic advisor, Dr. Jacqueline Johnson, for her guidance during this endeavor. She has challenged me to grow as a researcher and has shown great concern for my professional development. And we've had some laughs along the way, too!

I would like to thank Drs. Justin Baba, Charles Melcher, and Laurence Miller, for their participation in my Dissertation Committee. I appreciate their thoughtful questions and comments regarding this dissertation.

The research presented in this dissertation was a collaborative process that allowed me to work with many outstanding researchers. At the beginning of each experimental chapter, the specific contributions of each collaborator are acknowledged.

I am grateful for the time I have spent at UTSI. The faculty and staff here are outstanding. In particular, I would like to thank Dr. Brian Canfield, Dr. Lino Costa, Dr. William Hofmeister, Dr. Charles Johnson, Kathleen Lansford, Dr. George Murray, Dr. Deepak Rajput, Alexander Terekhov, Douglas Warnberg, and lab mates Jason Hah, Julie Swafford, and Adam Evans for their help throughout the years.

My time at UTSI has also given me the opportunity to work with many remarkable researchers from other institutions. Special mention goes to Dr. Amanda Petford-Long from Northwestern University, Dr. Sanjay Mishra from the University of Memphis, Dr. Richard Weber and Amit Tailor from Materials Development Inc., Dr. Lloyd Arrowood and Alex Moses from Consolidated Nuclear Security, L.L.C., Dr. Stefan Schweizer from Fachhochschule Südwestfalen and Fraunhofer-Anwendungszentrum für Anorganische Leuchtstoffe, and Drs. Charlotte Pfau and Christian Paßlick from Martin Luther University Halle-Wittenberg.

I would like to thank Dr. Carlos Alvarez from Northwestern University for the many informative conversations that we had while collaborating on our projects. His insight into FCZ glasses and glass ceramics led to many good ideas for process improvements in our lab at UTSI.

Dr. Richard Lubinsky from SUNY, Stony Brook has been a good friend and invaluable collaborator throughout this project. From New York City to Oak Ridge, I've enjoyed our travels together. I sure hope that one of our numerous "wacky ideas" will pay off some day.

Special mention must go to friend, collaborator, and occasional partner-in-crime, Sharon Gray. Sharon kept things upbeat even when the great, unpredictable gods of scientific research were not smiling upon us. She reminded me to recaffeinate when my coffee meter was running low, and kept our garbage extremely tidy with her aluminum foil.

I truly appreciate all the support and encouragement that my friends and family have given me while in graduate school. I can't thank my wife, Coral, enough for all of her patience and understanding during this time. She and my daughter Katherine (Katie-Bug) are my inspiration.

The project described in CHAPTER II: RARE EARTH DOPED DOWNSHIFTING GLASS CERAMICS FOR PHOTOVOLTAIC APPLICATIONS and portions of CHAPTER IV: EVALUATION OF A FLUOROCHLOROZIRCONATE GLASS-CERAMIC STORAGE PHOSPHOR PLATE FOR GAMMA-RAY COMPUTED RADIOGRAPHY were supported by the National Science Foundation under Grant Number DMR1001381.

ABSTRACT

Fluorochlorozirconate (FCZ) glass ceramics are versatile materials whose optical properties may be tuned through compositional or processing changes. For this work, FCZ glasses were synthesized, and then subsequently heat treated to create optically-active glass ceramics. The glasses and glass ceramics were characterized using a number of methods including differential scanning calorimetry, phosphorimetry, x-ray diffraction, and spectrophotometry. Samples were evaluated for applications in photovoltaics and computed radiography–especially those pertaining to intraoral dental radiography and portal imaging.

The ability of FCZ glass ceramics containing hexagonal barium chloride nanocrystals doped with the rare earth elements, holmium and europium, to downshift ultraviolet light to wavelengths more usable by polycrystalline silicon photovoltaic cells was investigated. The excitation spectra of FCZ glass ceramics doped or co-doped with divalent europium more closely match the solar spectrum at the earth's surface than an undoped sample. The addition of holmium gives rise to additional emission nearer to the band gap energy of polycrystalline silicon photovoltaic cells. These materials may increase the efficiency of photovoltaic cells in solar energy applications.

The sodium fluoride content in FCZ glass-ceramic storage phosphor plates was varied to determine the effect on sample properties, including photostimulated luminescence (PSL) light output for computed radiography applications, including intraoral dental radiography. The percentage of sodium fluoride used in each sample composition had a marked effect on glass stability, transparency, thermal characteristics, and PSL performance. The PSL light output of the samples may be suitable for nondestructive testing, where dose is not a primary concern.

An FCZ glass ceramic was evaluated for use as a storage phosphor in gamma-ray imaging. Test images were made at 2 MeV energies using gap and step wedge phantoms. Gaps as small as 101.6 μm [micrometers] in a 440 stainless steel phantom

were imaged using the sample imaging plate. Analysis of an image created using a depleted uranium step wedge phantom showed that PSL emission is proportional to incident energy at the sample and the estimated absorbed dose. The sample imaging plate has potential for nondestructive testing, as well as portal imaging applications, where it may provide geometric and dosimetric verification.

TABLE OF CONTENTS

LIST OF TABLES

LIST OF FIGURES

CHAPTER I: INTRODUCTION

Fluorochlorozirconate (FCZ) Glass Ceramics

Fluorochlorozirconate (FCZ) glass ceramics are composite materials consisting of an FCZ glass ceramic matrix with embedded crystallites, typically $BaCl_2$. The $BaCl_2$ crystallites serve as luminescent centers, making the materials optically active [1-5]. The luminescent properties of these materials may be enhanced through rare earth doping [6-13]. The dopants may remain in the matrix, or may be incorporated into the $BaCl_2$ crystals. In addition, the matrix has many desirable properties, typical for halide glasses, such as low phonon energy and high transmission in the infrared region of the electromagnetic spectrum [10, 14].

FCZ glass ceramics can be responsive to many types of radiation. They can be photoluminescent–capable of being excited by visible, UV, and/or infrared radiation (see Figure 1) [15-17]. With ionizing radiation, such as x-rays or gamma rays, the materials can behave as either scintillators or storage phosphors depending upon processing conditions [6, 7, 12, 18-21]. The versatility of these materials makes them suitable for a variety of applications, including medical imaging – particularly mammography or dental radiography (see Figures 2 and 3), nondestructive testing, radiation detection, and wavelength conversion/shifting for photovoltaic applications.

These materials are synthesized as a glass then subsequently heat treated to precipitate the $BaCl_2$ crystals within the matrix. Typical compositions are based upon ZBLAN (the fluorides of Zr, Ba, La, Al, and Na) with one or more substitutions to introduce Cl^- into the matrix, such as $BaCl_2$ for BaF_2 or NaCl for NaF [8, 21]. A small amount of InF_3 or SnF_4, whose cations are multivalent, is often added to the composition to stabilize the Zr in the +4 valence state, preventing inclusions in the glass caused by reduced species of Zr [22]; alternately a reactive atmosphere, such as H_2, may be used during synthesis [9]. Because these materials can be cast in a mold, a wide variety of shapes are possible.

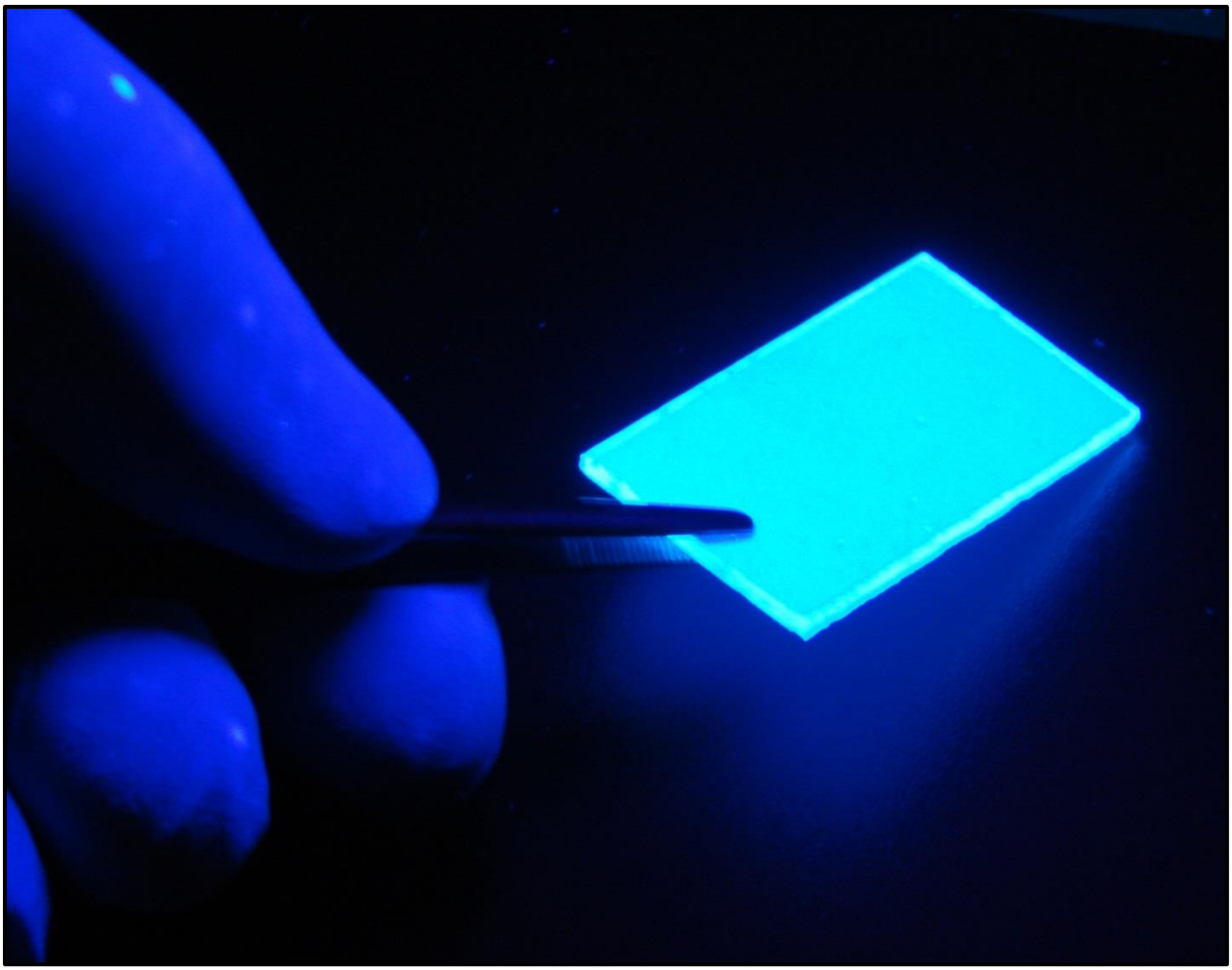

Figure 1. An FCZ glass ceramic exhibiting photoluminescence under UV excitation of 365 nm.

The heat treatment process is critical in the creation of FCZ glass ceramics. It controls the volume percentage, size, number, and phase of the $BaCl_2$ crystals present in the matrix [11, 12, 23-25]. At heat treatment temperatures of approximately 230 to 260 °C, hexagonal-phase $BaCl_2$ nanocrystals will form. At higher heat treatment temperatures, approximately 290 °C, the hexagonal-phase $BaCl_2$ crystals, which always form first, will transform into orthorhombic-phase $BaCl_2$ crystals. The hexagonal phase is generally preferable for scintillator applications, while the orthorhombic phase has better storage phosphor performance [18, 21].

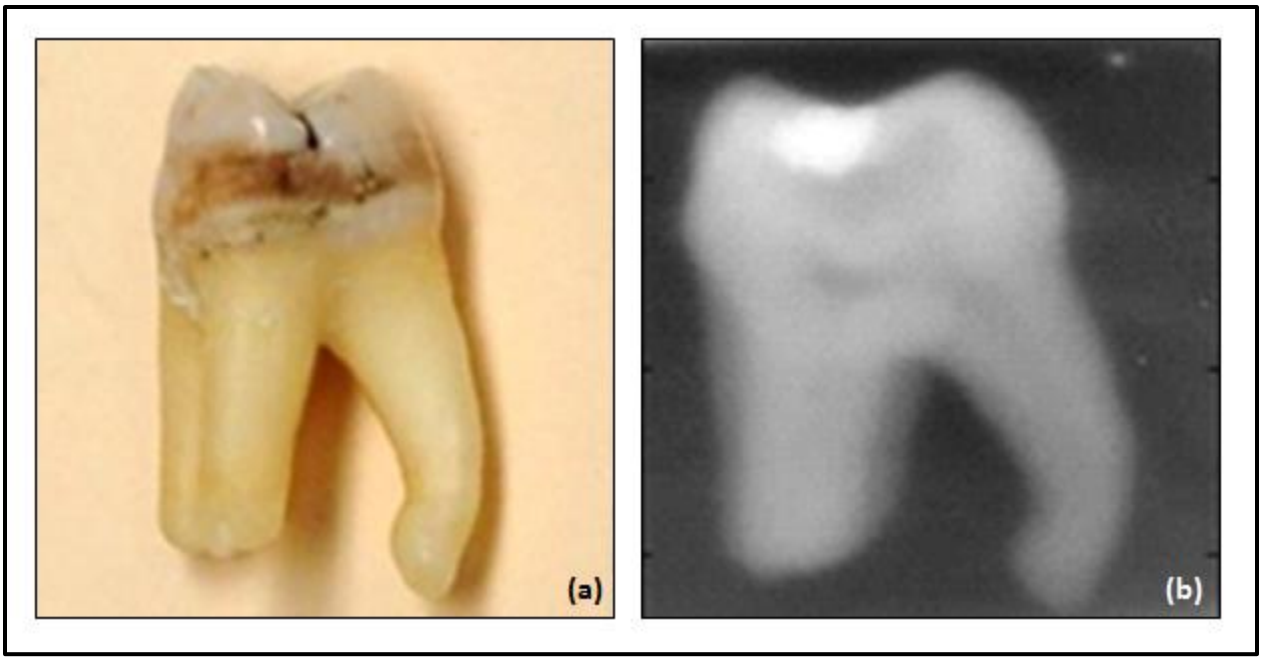

Figure 2. (a) a photograph of a tooth with a metal filling and (b) a dental radiograph of the same tooth produced with an FCZ glass-ceramic storage phosphor plate for computed radiography.

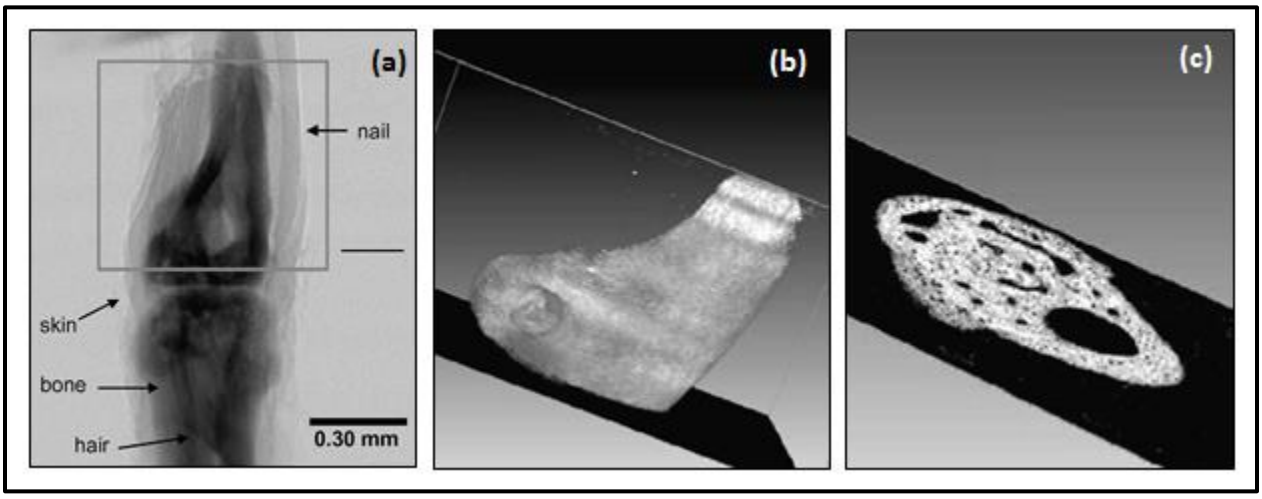

Figure 3. X-ray micro-CT images of a mouse joint recorded on a 2% Eu-doped FCZ glass-ceramic scintillator plate: (a) a transmission X-ray image, (b) a reconstructed 3-D image of the selected image in (a), and (c) a cross section from the 3-D image in (b). The figure was adapted from [21].

Photovoltaic Cells

Photovoltaic (PV) cells, commonly referred to as solar cells, are solid-state devices that convert photonic energy into electrical current. The PV effect was discovered in 1839 by French physicist Alexandre-Edmond Becquerel. Early photovoltaic cells had very low efficiencies. It was not until the 1950s that Bell labs developed the first practical PV cell by using a diffused silicon p-n junction. Initial applications were limited to space, where the cells' power-to-weight ratio made them superior to other options available at the time. Over time, the efficiencies of these devices have steadily increased along with their applications [26, 27].

Photovoltaic cells have many advantages over other power sources such as coal or natural gas. After construction, they operate essentially pollution free. They generate energy from the sun, which is a renewable resource. They can operate on a small scale and can be placed in remote areas because they do not need to have fuel to produce electricity.

Unfortunately, the total cost of a photovoltaic cell over its lifetime, generally measured in kilowatts-per-dollar, is high when compared to nonrenewable sources such as coal or natural gas. However, photovoltaic cells do have niche applications, such as supplying ancillary peak power for large cities, which is generally required mid-day when demand is highest, but also when solar cells are most efficient due to the position of the sun. However, for photovoltaics to be competitive in supplying electricity on a large scale, their efficiency will have to improve and their price will need to drop.

Polycrystalline silicon photovoltaic cells are the most purchased type of solar cell [27]. They consist of two layers of polycrystalline silicon, p-type–containing an abundance of electron holes, and n-type–containing an abundance of electrons. The two layers form a p-n junction. They are generally less expensive than other types of cells but also less efficient. Some factors that influence their efficiency are the Shockley–Queisser limit, attenuation of the solar spectrum by assembly components, absorption of light away from the depletion zone, and reflection of the incident light.

The Shockley–Queisser limit predicts the maximum efficiency that a single bandgap photovoltaic cell can achieve at the earth's surface, under the solar spectrum (see Figure 4) [26]. For polycrystalline silicon PVs, which have bandgap energy of 1.1 eV, this value is around 30%. There are two reasons for this value (see Figure 5). The first is that photons with energies below that of the bandgap of the PV are not absorbed and pass through without generating the electron-hole pairs necessary for electrical current. The second reason is that photons with energies greater than that of the bandgap do not completely transfer their energy into electrical current; all energy in excess of the bandgap is converted to heat, which cannot be harnessed.

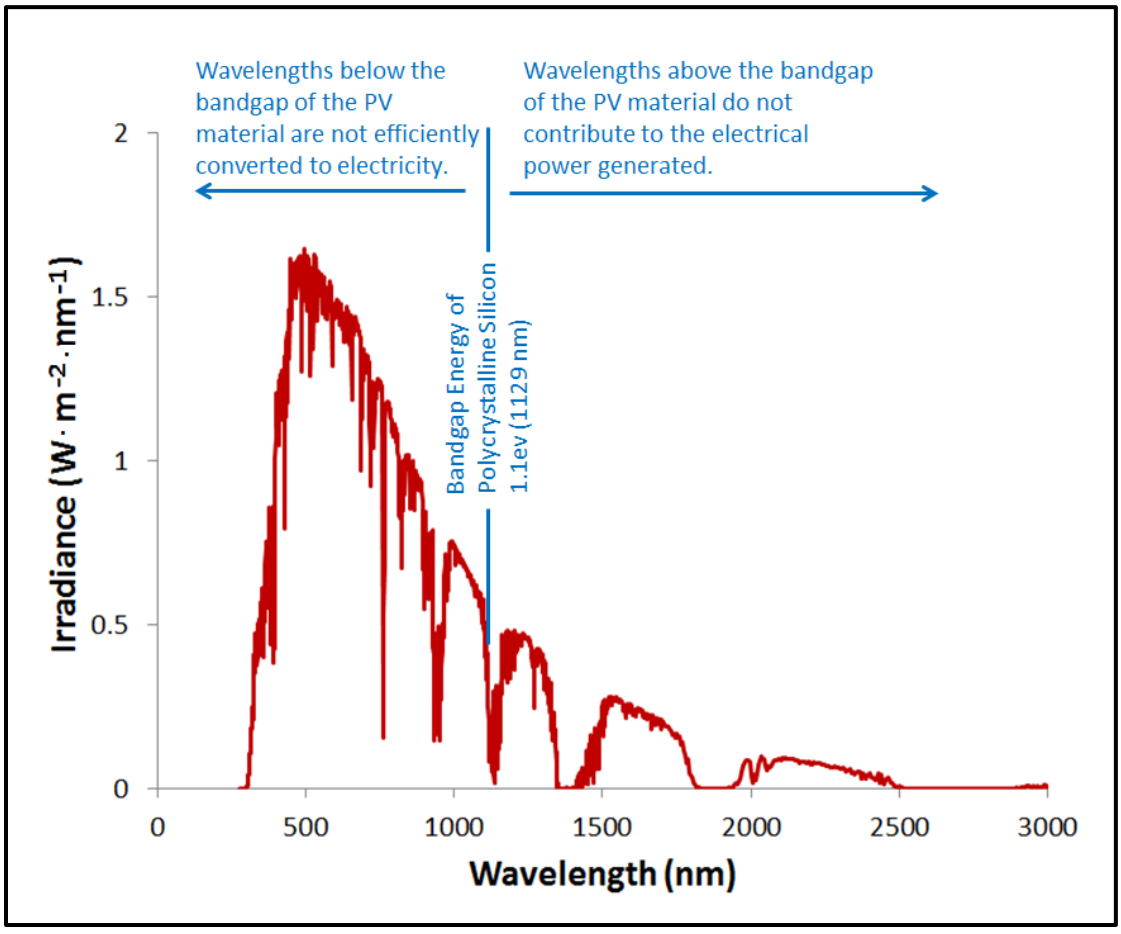

Figure 4. The solar spectrum at the earth's surface shown with the bandgap energy of polycrystalline silicon. Adapted from [28].

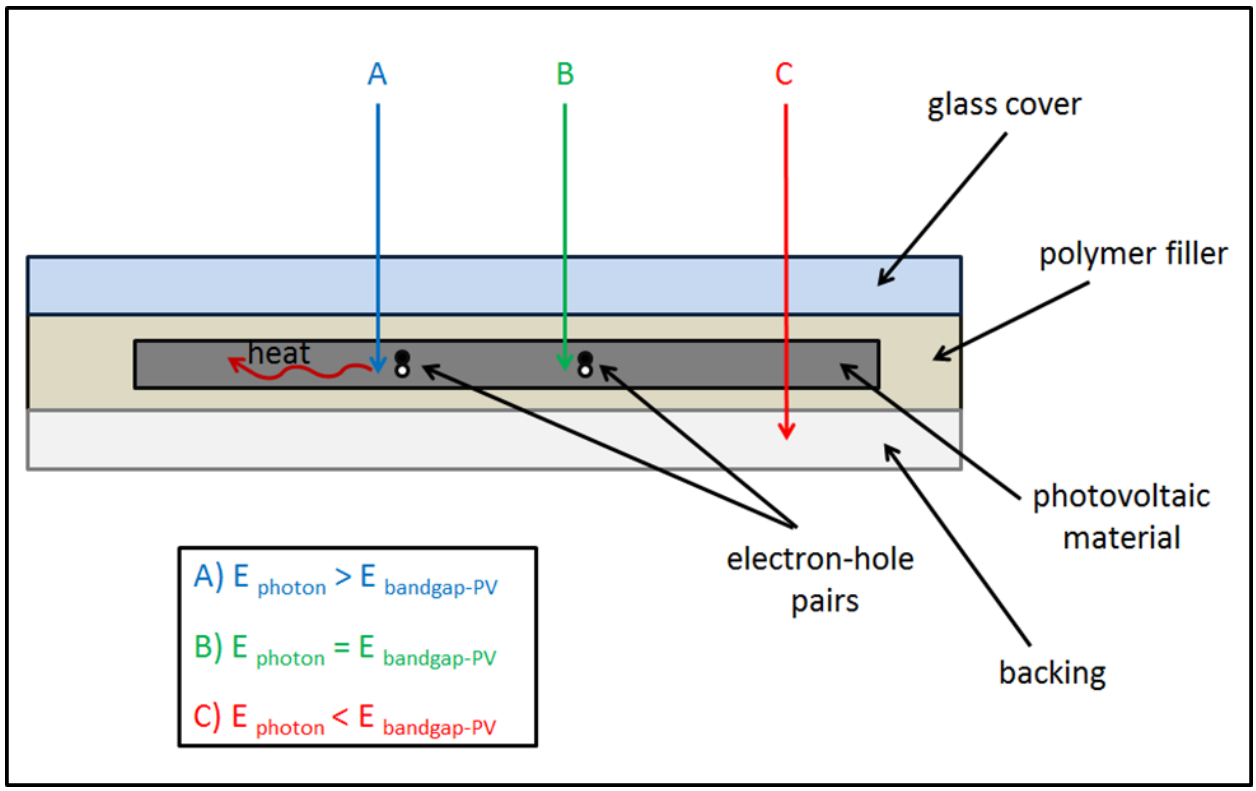

Figure 5. Schematic showing conversion inefficiencies due to differences between the energy of the incident photons and the bandgap of the in PV material: a) excess photonic energy is lost as heat, b) no photonic energy is lost, c) all photonic energy is lost.

The components of the solar cell assembly that hold and protect the photovoltaic material also contribute to the inefficiency of solar cells. Typically the photovoltaic is held within a polymer filler behind a glass cover, usually made from soda-lime glass, for protection. These materials are not transparent to ultraviolet (UV) light and prevent a significant portion of the solar spectrum from reaching the photovoltaic cell.

Light absorption away from the depletion zone is another factor that decreases the efficiency of solar cells. The depletion zone is a region which surrounds the p-n junction in polycrystalline silicon photovoltaics. If light is absorbed away from the depletion zone in the n-region, the electron hole pairs will spontaneously recombine without the

generation of electrical current. For this reason, the n-regions of the cells are generally made as thin as possible. Absorption of the ultraviolet radiation in this region is a significant problem.

If light scatters off the glass cover that protects a solar cell instead of passing through, this energy is wasted. This problem has been mostly solved by the addition of anti-reflective (AR) coating to the top surface of the protective glass cover.

Downshifting is one strategy to alleviate the inefficiencies caused by the Shockley–Queisser limit: i.e., the UV absorption in the solar cells by the glass cover and polymer filler, and absorption in the n-region of PVs [29-31]. Downshifting is the absorption of light by a photoluminescent material with subsequent emission of light at lower energy (longer wavelength) as shown in Figure 6. In the case of solar cells, downshifting material is added to the cover glass, so that higher energy ultraviolet light is converted to lower energy visible light that can be used more readily by the photovoltaic cell. The lower energy light is able to pass through the glass cover and polymer filler of the assembly and also the n-region of the photovoltaic to reach the depletion zone, where it can be harnessed to create electrical energy. There is still some loss of energy to heat in this process, but overall, more useable light energy reaches the PV material. Furthermore, it is more advantageous for the heat generated to be localized on the glass cover surface, as it can be transferred away by convection; PV efficiency deteriorates with higher temperatures. An additional benefit of this approach is that there is reduced exposure of the photovoltaic units to ultraviolet radiation, which can be damaging to cells over time.

The excellent photoluminescent properties of FCZ glass ceramics make them potential candidates for downshifting glass covers for photovoltaic applications. The combination of a transparent, low phonon energy matrix and luminescence-enhancing nanocrystals may allow for a significant increase in photovoltaic efficiency through better utilization of the UV portion of the solar spectrum.

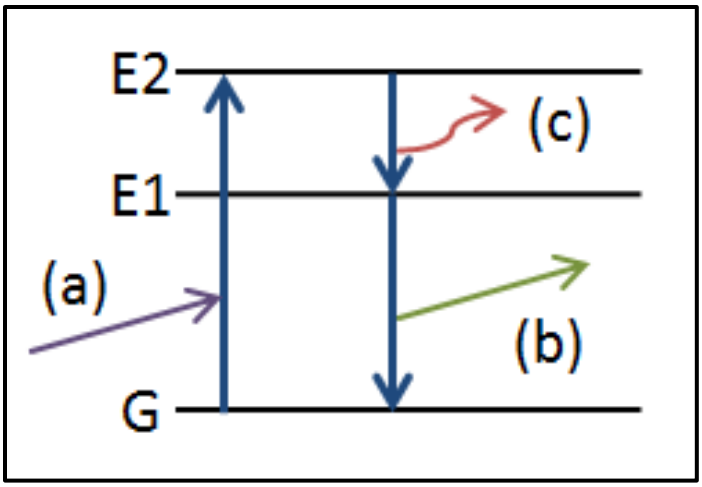

Figure 6. Downshifting: absorption of (a) higher energy, lower wavelength light and the subsequent emission at a (b) lower energy, higher wavelength. Some energy is lost as (c) heat.

Computed Radiography

Computed radiography (CR) is a popular imaging technique with applications in both medical imaging and nondestructive testing [32-36]. CR systems use a reusable storage phosphor imaging plate. In CR, an x-ray source produces a beam that is attenuated by the subject (patient). Denser materials–especially those with high atomic number–absorb more radiation, thereby creating contrast. The radiation incident at the imaging plate will therefore vary spatially. The image is stored as metastable electron-hole pairs; their density is proportional to the incident energy. Photostimulation, typically by a laser, causes recombination of electron-holes pair with resulting emission of light that is of a different wavelength than the stimulation source. The photostimulated light can be collected pixel-by-pixel across the imaging plate and assembled via computer to create a radiographic image. Any residual image stored within the plate can be erased by prolonged exposure to a light source of sufficient intensity. The process is repeatable and the imaging plates can be re-used multiple times; the lifetime of the plates is generally limited by wear or physical damage to the plates.

Commercial CR systems were introduced in the1980s as an attractive alternative to film/screen systems. CR has many advantages over film/screen systems, including: greater dynamic range, reusable media, and automatic digital image creation with readout. In the commercial market for new two-dimensional radiographic systems, digital radiography (DR) systems–which use a solid-state, flat panel detector–are CR's primary competition, with both systems owning a sizeable market share.

Glass-Ceramic Storage Phosphor Materials

Glass-ceramic storage phosphors have received much attention for their potential as storage media for computed radiography applications [18, 19]. The most studied system is based upon fluoride glass with precipitated halide crystals within the matrix. Other glass matrices, such as the borate glass system, have been studied as well [37].

Commercial CR imaging plates consist of polycrystalline storage phosphor crystals held within a polymeric binder. A thin polymer film protects the optically-active layer from damage, while a thicker layer on the opposite side provides stability and support. A significant disadvantage with this type of plate is that the stimulating light used during readout scatters across the grain boundaries of the polycrystalline material, thus causing photostimulated emission away from the target pixel. This emission is undesirable because it decreases the spatial resolution of the system (see Figure 7a). To mitigate the effects of scattering, the thickness of the plate must be limited; this reduces x-ray absorption and requires a trade-off between spatial resolution and detective quantum efficiency (DQE).

A glass-ceramic CR imaging plate consists of a transparent glass matrix with embedded nanoscale storage phosphor crystals. The size of the crystallites is significantly smaller than the wavelength of the stimulating light source, so scattering is greatly reduced. The reduction of scattering increases the spatial resolution of the system, bestowing glass-ceramic storage phosphors an inherent advantage over commercial polycrystalline plates (see Figure 7b). The reduced scattering also allows for thicker plates to be utilized, increasing x-ray absorption and DQE.

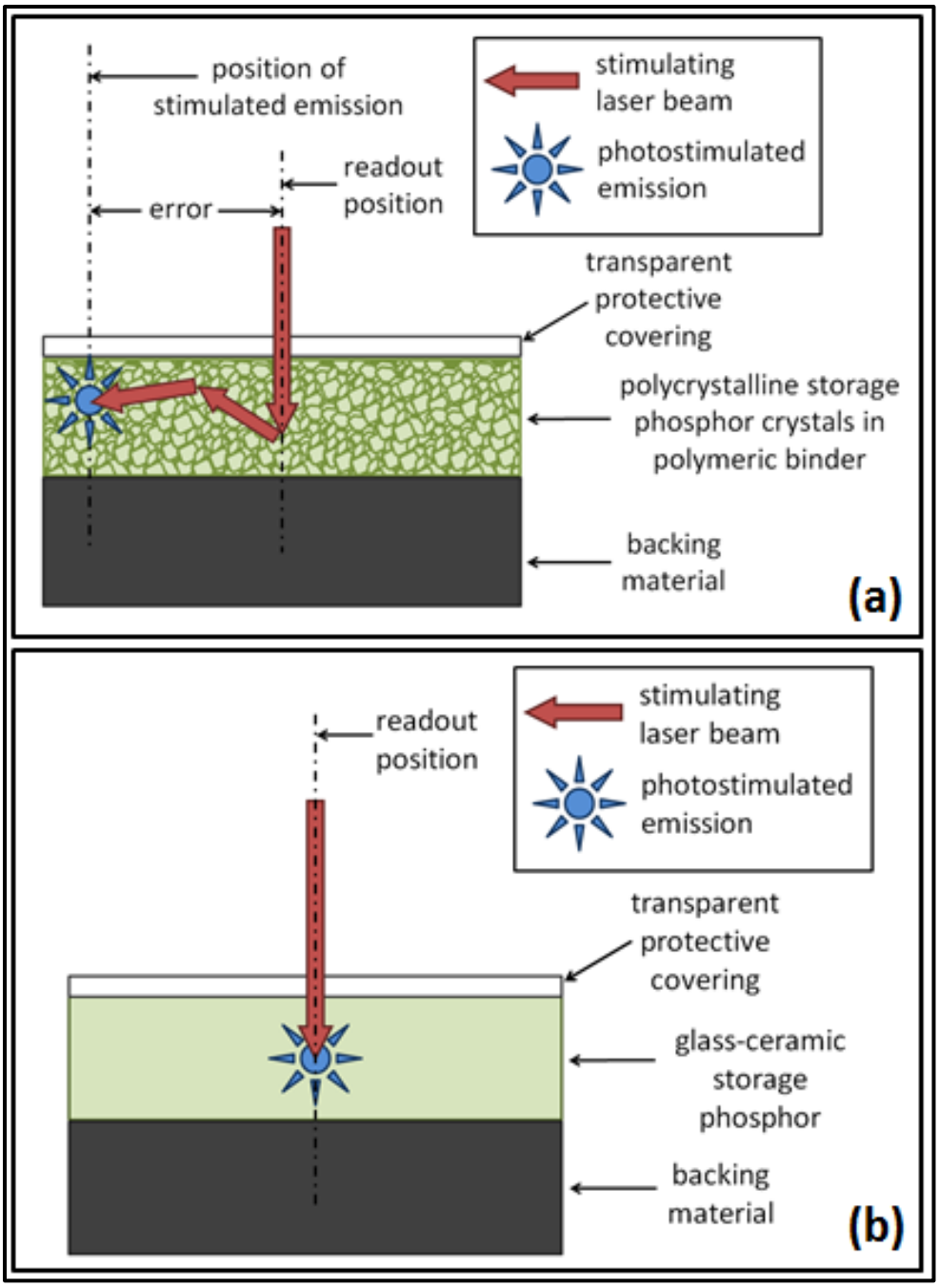

Figure 7. (a) Scattering of the stimulating laser beam at the grain boundaries of a polycrystalline storage phosphor causing a decrease in spatial resolution and (b) reduced scattering in a glass ceramic storage phosphor for improved spatial resolution.

Biomedical Applications of Glass-Ceramic Storage Phosphor Materials

Due to the potential for high resolution computed radiography, there has been much interest in developing glass-ceramic storage phosphors for biomedical applications such as mammography, where the ability to resolve 50-200 um microcalcifications is imperative [38]. The relatively large format plates required for mammography (18 cm × 24 cm and 24 cm × 30 cm), however, make optimization for this application problematic on a laboratory scale. For this reason, optimized glass ceramic imaging plates for dental applications, in particular intraoral dental radiography, are a more logical starting point for commercial development due to the significantly smaller imaging plate size (24 mm × 40 mm for a size 1 plate).

Intraoral Dental Radiography

Intraoral dental radiography is an invaluable tool for the diagnosis and detection of oral diseases such as dental caries (cavities), root fractures, and periodontal (gum) diseases [39, 40]. Intraoral dental radiography systems were film-based until the 1980s when direct digital and indirect digital systems were introduced commercially. Film-based systems are still in-use today, but the general trend is a migration to digital systems [41].

In general, exposures are carried out in similar fashion for each of the three radiographic methods (film, direct digital, and indirect digital). An x-ray source operating between 60-70 kVp produces a beam. The beam is conditioned using a filter made from a material such as aluminum to remove lower energy x-rays. The beam is positioned so that the region of interest lies in the focal spot. The x-ray beam is attenuated by the patient's tissue and is recorded by a sensor for the creation of an image. Paralleling techniques may be used to ensure dimensional accuracy of the image recorded by the sensor.

How the three types of intraoral radiographic systems differ is in their method of recording an image and subsequent readout. Film systems use an x-ray sensitive silver halide emulsion to create a latent image that must be subsequently chemically

developed; the resulting analog image is displayed in a light box. Direct digital systems (analogous to DR systems in medical imaging) use a solid state sensor, either a charge coupled device (CCD) or a complementary metal oxide semiconductor (CMOS) to create a digital image; the sensors are either x-ray sensitive or light sensitive and paired with an x-ray scintillator. Indirect digital systems use a photostimulable phosphor (PSP) to record the image, which much be subsequently read-out using a high speed laser scanner system; this type of system is analogous to CR in medical imaging. Each of these systems has distinct advantages and disadvantages [39, 40, 42-46].

Dental practitioners are moving away from film-based systems for many reasons. The dose required to generate a diagnostic quality image is higher with film than with digital methods. Developing the film is labor intensive and requires a dark room and consumable chemicals. The analog images produced are not easily shared or archived. The dynamic range for film is more limited than with digital systems, making retakes due to over- or under-exposure more likely.

Dental radiography is unique in that imaging is not usually performed by a specialist (radiologist), but rather by the dental practitioner or a staff member. This lack of specialization and presumably expertise establishes the need for dental radiography systems to produce acceptable images with less than ideal exposure parameters. Therefore a system that produces high quality images over a wide exposure range is highly desirable; it will reduce overall dose to patients due to the reduction in retakes.

Standard parameters are required to objectively compare radiographic systems. The following is a list, from literature [39, 43], of parameters commonly used:

- spatial resolution – usually expressed in the number of line pairs per millimeter that can be resolved
- contrast resolution – typically expressed as the number of holes of varying depth in an aluminum phantom that can be detected simultaneously
- practical exposure range – the difference between the lowest and the highest acceptable exposure for making a diagnostic-quality image

In general, there is considerable variation in performance between commercial systems for each type of system: direct or indirect, with neither system having a clear advantage in the commercial market. In practice, the type of system purchased depends upon the preference of the dental practitioner and includes such factors as cost (both initial and ongoing), patient comfort, and ease of operation.

Costs vary primarily based upon performance; however, there are some differences between the direct and indirect systems. Direct systems require the purchase of a costly solid state sensor for each image size (pediatric periapical, adult periapical, panoramic, etc.). Replacement costs for direct imaging sensors are much higher than for indirect, although indirect sensors are more prone to wear.

Due to the thin, flexible nature of PSP plates, indirect radiography is generally considered more comfortable than direct. Direct radiography typically requires a cord for power and data transmission. This feature combined with the relatively large overall thickness of the sensor can make this type of system uncomfortable for children and adults with disabilities. Wireless sensors are available, but do little to increase comfort due to the increase in size required for accommodating a battery. Patients with a tendency to gag may find DR sensors intolerable. Positioning errors are more likely with the larger solid state detectors, so retakes are more frequent.

Results from a direct radiography system are immediately available; whereas indirect systems require additional time due to the additional readout step required. One common readout system for indirect systems may accommodate multiple examination rooms, though. For direct systems, either an individual sensor must be purchased for each examination room or the sensor must travel from room-to-room.

There is a desire for improved intraoral radiography systems, in terms of dose and resolution–both spatial and contrast. For example, one study showed that in a comparison of four different modalities: film, CCD, PSP, and cone beam CT, none of the studied systems exhibited both high sensitivity and specificity in the detection of

proximal caries [45]. Commercial PSP plates have been shown to be no more effective than film in the detection of dental root fractures [46]. It is generally acknowledged that there is no lower limit to a safe amount of x-ray exposure and it should be limited where possible, following the ALARA principle–as low as reasonably achievable. Children, with rapidly dividing cells, may be at special risk. In developed nations, dental patients will have radiographs taken of their mouths at periodic intervals, typically once per year. Lowering the dose required for each dental radiograph will significantly lower the total radiation dose received by dental patients over a lifetime.

Dental radiography systems based upon current PSP technology require a tradeoff between dose and resolution. Scattering of the stimulating light at the crystalline boundaries during readout is a significant factor that limits image resolution. Resolution improves as the thickness of the phosphor decreases, because of reduced scattering length. Conversely, quantum efficiency, the ratio of detected to incident x-ray quanta, is decreased due to lower x-ray absorption. Meaningful improvements in PSP-based imaging thus require a new type of phosphor material.

Glass-ceramic storage phosphors represent a new class of computed radiography imagining plates. As previously discussed in this chapter, reduced scattering of the stimulating light in these materials provides an advantage in spatial resolution. In addition, the light output per volume crystal is enhanced by the glass matrix [12].

The development of glass-ceramic storage phosphors has not yet reached maturity. Factors that influence performance include matrix composition and the size, distribution, phase, and chemical composition of the embedded storage phosphor crystals. For example, the incorporation of lead into the glass matrix may increase x-ray absorption and increase detective quantum efficiency. Optimization of these parameters may lead to a glass-ceramic intraoral imaging plate superior to existing commercial plates in terms of spatial resolution, contrast resolution, dynamic range, and optimized exposure (dose).

Portal Imaging

Portal imaging is the use of an oncological therapeutic beam to create an image. The primary purpose of this technique is to accurately position the patient [47, 48]. Ideally, the image could also be used to verify that the proper dose was administered to the patient. Furthermore, it should be possible for the image to be of near-diagnostic quality, so the condition of the irradiated tumor could perhaps be evaluated without additional, subsequent imaging; this would reduce dose to the surrounding tissues [48, 49].

The energies used in oncology are considerable (greater than 1 MeV) and much greater than those used in traditional radiographic applications (less than 100 keV) as shown in Table 1. At such energies, interaction occurs primarily by Compton scattering, which makes imaging difficult due to low object contrast. Other factors such as the size of the focal spot, scattered radiation, and patient motion compound the difficulties of making a high quality image at the energies required. For example, in dental radiography spatial resolution greater than 10 lp/mm is not uncommon, while modern electronic portal imaging devices (EPID), have values in the range of 0.3-0.4 lp/mm [50].

Originally standard x-ray film was used for the acquisition of portal images. Eventually, specialized portal films were developed. Over time other methods were applied including CR, EPID, and active matrix flat panel detectors (AMFPI). Each modality has its advantages and disadvantages [47, 48, 51, 52]. Portal film is the traditional medium utilized for portal imaging; but it is not reusable, requires chemical development, and produces analog images that must be digitized in a subsequent step for digital manipulation and storage. CR systems have a large dynamic range and produce high-quality digital images, but require image readout with a laser scanner; thereby the images produced are not immediately available. EPDI and AMFPI systems can produce an immediate image, but are a subject to radiation damage if the detector is placed directly in line with the therapy beam, thus leading to costly replacement. Other configurations of EPDI and AMFPI, in which the sensors are outside the beam, such as those where a mirror is employed, are inefficient.

Table 1. Typical energies for radiotherapy for certain cancer locations. Adapted from [48].

Cancer Location	Beam Energy (MeV)
larynx	4
breast	8
lung	8
prostate	8-18

Glass ceramic-based CR plates for portal imaging may hold an advantage over commercially available polycrystalline ones. As noted previously, reduced scattering of the stimulating light source in the glass-ceramic plate should lead to increased spatial resolution. In addition, the transparent nature of these materials allows for thicker, more radiation-absorbing plates to be used for imaging. Conversely, commercial CR plates are turbid, so thicker plates would not allow complete transmission of either the stimulating source or the photostimulated emission. The increased absorption of the therapy radiation by the glass-ceramic imaging plates may lead to an increase in detective quantum efficiency and improved imaging characteristics. Improvements in spatial resolution and contrast could potentially reduce positioning errors and thus decrease the treatment margins around the clinical target volume.

Summary of Work

This work explores the effects of changes in composition and processing on the properties of FCZ glasses and glass ceramics. Special interest is given to the crystallization characteristics of these materials and their luminescent properties. Chapter II focuses on the effects of the dopants Eu^{2+} and Ho^{3+} on material properties and the suitability of these materials as downshifters for photovoltaic applications. Chapter III investigates how the amount of the network modifier NaF affects the precipitation of $BaCl_2$ crystals in the glass matrix and its effect on the storage phosphor

performance for intraoral dental radiography applications. Chapter IV explores the use of an FCZ glass ceramic for computed radiography at MeV energies to determine the material's suitability for portal imaging and nondestructive testing applications.

CHAPTER II:

RARE EARTH DOPED DOWNSHIFTING GLASS CERAMICS FOR PHOTOVOLTAIC APPLICATIONS

A version of this chapter was originally published by Russell L. Leonard, Sharon K. Gray, Shauna D. Albritton, Lydia N. Brothers, Raven M. Cross, Andrea N. Eastes, Hien-Yoong Hah, Hodari S. James, Julie E. King, Sanjay R. Mishra, and Jacqueline A. Johnson:

> Leonard, R.L., et al., *Rare earth doped downshifting glass ceramics for photovoltaic applications.* Journal of Non-Crystalline Solids, 2013. **366**: p. 1-5. doi:10.1016/j.jnoncrysol.2013.01.029

Russell L. Leonard was responsible for all writing and research activities in the original article except as noted: Gray assisted with the synthesis of the as-made glass samples, heat treatments, and XRD data collection. Gray, Albritton, Brothers, Cross, Eastes, Hah, James, King, and Mishra participated in the DSC and/or preliminary XRD data collection. Johnson provided guidance for the overall project. Some ancillary figures, not present in the original publication, are included in the Appendix.

Abstract

The ability of fluorochlorozirconate (FCZ) glass ceramics containing hexagonal barium chloride nanocrystals doped with the rare earth elements, holmium and europium, to downshift ultraviolet light to wavelengths more usable by polycrystalline silicon photovoltaic cells was investigated. Six rare-earth-doped and one undoped FCZ glass samples were synthesized and subsequently heat treated to produce glass ceramics containing barium chloride nanocrystals in the hexagonal phase. The glasses were characterized by differential scanning calorimetry to determine crystallization temperatures for the heat treatment process. The resulting glass ceramics were characterized by x-ray diffraction, phosphorimetry, and spectrophotometry. All samples produce light centered at 470 nm when excited by ultraviolet radiation. The excitation spectra of FCZ glass ceramics containing hexagonal barium chloride nanocrystals doped or co-doped with divalent europium more closely match the solar spectrum at the earth's surface than the excitation spectrum of an undoped sample. This feature of the

europium doped glass ceramics makes them suitable for the process of downshifting to improve the efficiency of polycrystalline silicon photovoltaic cells. The addition of holmium to the glass ceramics gives rise to additional emissions at higher wavelengths and nearer to the band gap energy of polycrystalline silicon photovoltaic cells, reducing heating of the cells and thereby increasing cell efficiency. Additionally, the strong absorption by europium in the ultraviolet region of the spectrum may allow these glass ceramics to serve as a protective layer for ultraviolet sensitive materials.

Introduction

Polycrystalline silicon photovoltaic (PV) cells are the most purchased type of solar cell [27]. They are generally less expensive than other types of cells, but also less efficient. Some factors that influence their efficiency are the Shockley–Queisser limit [26], attenuation of the solar spectrum by assembly components, and absorption of light away from the depletion zone.

Downshifting is one strategy to alleviate these inefficiency problems [29] . Downshifting is the absorption of light by a photoluminescent material and the subsequent emission of light of lower energy. In the case of solar cells, downshifting material is added to the cover glass, so that higher energy ultraviolet light is converted to lower energy visible light, which can be more readily used by the photovoltaic cell. The lower energy light is able to pass through the glass cover and polymer filler of the assembly and also the n-region of the photovoltaic cell, to reach the depletion zone, where it can be harnessed to create electrical energy (see Figure 8). There is still some loss of energy to heat in this process, but more useable light energy reaches the PV material. Furthermore, it is advantageous for the heat to be generated on the cover surface where it can be transferred away by convection, as PV efficiency deteriorates with higher temperatures. An additional benefit of this approach is that there is reduced exposure of the photovoltaics to ultraviolet radiation, which is damaging to the cell over time.

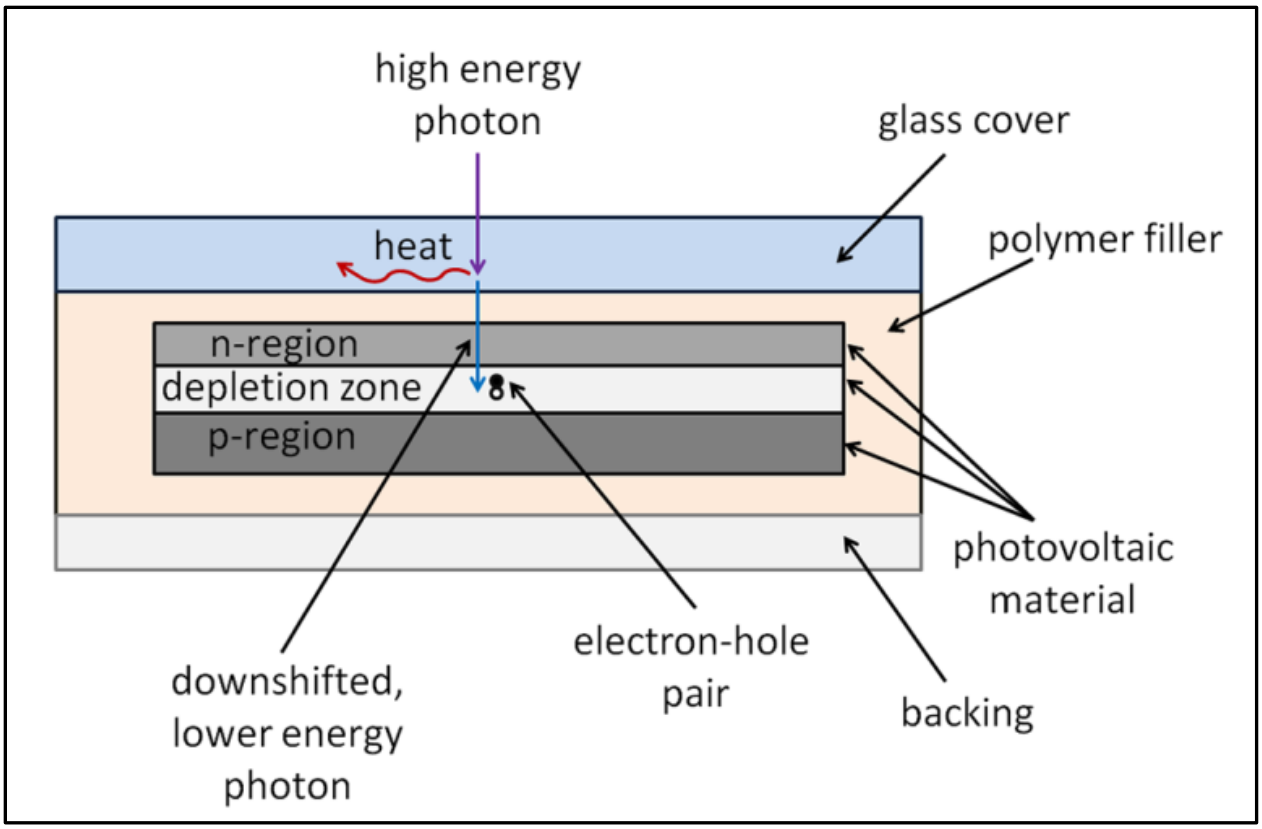

Figure 8. Illustration of Downshifting to Improve PV Efficiency

The purpose of this work is to investigate the ability of fluorochlorozirconate (FCZ) glass ceramics [16, 17, 53] containing hexagonal barium chloride nanocrystals doped with the rare earth elements, holmium and europium, to downshift ultraviolet light to wavelengths more usable by polycrystalline silicon photovoltaic cells. Europium and holmium are both well-known luminescent materials, producing emission in the visible range [54, 55]. A series of FCZ glass samples were produced with the desired amount of rare earth dopant, and then subsequently heat treated to precipitate $BaCl_2$ nanocrystals to create a glass ceramic. Crystallization temperatures for the base glasses were found using differential scanning calorimetry (DSC) [25, 56, 57]. X-ray diffractometry (XRD) was used to identify the phases present in the glass ceramics [58]. Emission and excitation spectra were determined with phosphorimeter measurements [20, 59]. The locations of absorption peaks in the glass ceramics were found using a spectrophotometer.

Materials and Methods

Six FCZ glass samples were prepared for this research with a composition in mole percentage of this form: 51.0ZrF_4-20.0$BaCl_2$-20.0NaF-3.0AlF_3-3.5LaF_3-0.5InF_3-x$EuCl_2$-(2.0-x)HoF_3, where x represents the amount of the doping material to be added. One additional sample with no dopant material was also made for comparison, 53.0ZrF_4-20.0$BaCl_2$-20.0NaF-3.0AlF_3-3.5LaF_3-0.5InF_3.

During synthesis, the raw materials were weighed in a glovebox (MBRAUN Labmaster SP) with an argon atmosphere to prevent contamination from oxygen or water vapor. Next, the sample materials were heated within a platinum crucible inside a programmable tube furnace (MTI Corporation OTF-1200X) to a temperature of 825 °C (see Figure A1 in the Appendix). The furnace was connected to the glovebox though a doorway and also contained an argon atmosphere. At the completion of the heating cycle, the molten glass was poured into a brass mold at a temperature of 200 °C (see Figure A2 in the Appendix). The brass mold was equipped with a cartridge heater connected to a PID controller, allowing for the gradual cooling of the glass to room temperature over a period of four hours.

Differential Scanning Calorimetry (Netzsch DSC 200 F3) scans were made from 100 °C to 400 °C at a rate of 10 K per minute. Sample mass was 20 ± 10 mg for each scan. The results of these scans determined the heat treatment temperatures used to precipitate barium chloride nanocrystals within the glass samples, converting them into glass ceramics [58].

A portion of each glass sample of approximate size 1 cm x 1 cm was heat treated in air using a tube furnace at around 250 °C for five minutes to precipitate hexagonal $BaCl_2$ nanocrystals in the glass matrix of the samples to create a glass ceramic. Prior to heat treatment, the samples were preheated using a hot plate to approximately 200 °C to prevent thermal shock. During the heat treatment process, the samples were held in an aluminum compartment that had an embedded thermocouple to monitor temperature.

Upon removal from the aluminum compartment the samples were placed on a 200 °C surface to prevent thermal shock and then allowed to cool slowly in the ambient air.

X-ray diffraction measurements of the heat treated samples were performed on a Philips X'Pert MRD X-ray Diffractometer in the 2θ range from 20° to 80°. Scanning rate step size was 0.01° with a time step of 4 seconds. Prior to measurement, the samples were polished to expose the sample bulk. MDI Jade 9 analytical software was used to identify phases.

Excitation and emission spectra were determined using a QM-3-PH phosphorescence / fluorescence spectrofluorometer (Photon Technology International, Inc.) with Czerny-Turner monochromators at the source and detector. The system was equipped with a Type L4633 Xenon Flash Lamp (Hamamatsu Photonics K.K.) and an R1527P Photomultiplier tube (Hamamatsu Photonics K.K.). The computer interface was a PC equipped with FeliX32 software for data analysis. The measurements in this study were made using the following parameters: step size = 1 nm, integration time = 50 µs, averages (number of repeated scans for which results are averaged) = 3, shots (lamp pulses per each individual scan with results averaged) = 50, lamp frequency = 100 Hz.

Transmission spectra for the samples were found using GenTech Scientific TU-1901 double beam ultraviolet/visible light spectrophotometer with UVWin 5.0.4 software. The samples were scanned from 190 to 900 nm in one nanometer increments. Interchange from the tungsten lamp to the deuterium lamp occurred at 360 nm.

Results and Discussion

Differential Scanning Calorimetry

Differential Scanning Calorimetry scans yielded similar results for all samples (see Figure 9). The addition of the rare earth halides had no measurable effect on the DSC scans. The glass transition temperature for all samples was about 214 °C. The large exothermal peaks centered near 240 °C represent the formation of hexagonal $BaCl_2$

crystals [58]. At higher temperature, these crystals undergo a solid state transformation to form the orthorhombic phase [60], which is associated with the exotherms at approximately 300 °C [56]. Large exothermic peaks due to bulk crystallization of the glass matrix can be seen centered between 314 °C and 331 °C [56].

X-ray Diffraction

X-ray diffraction results confirmed that nanocrystals precipitated during the heat treatment process for the glasses (see Figure 10). The diffractograms for the heat treated samples were all quite similar, meaning the same phases are present in all samples after heat treatment. The diffractogram for an unannealed glass is shown for comparison. The crystal peaks match the pattern for $BaCl_2$ in the hexagonal phase (Powder Diffraction File PDF 45-1313). These results, along with the results from DSC, indicate that the amount and type of doping had little or no effect on the hexagonal $BaCl_2$ crystallization process.

Phosphorimetry

Barium chloride nanoparticles doped with divalent europium embedded in an FCZ glass matrix give photoluminescent emission when excited with UV radiation [61]. Results from this study show that the presence of europium is not required for emission from barium chloride nanocrystals in the hexagonal phase (see Figure 11a). The excitation spectrum for the undoped glass ceramic is complex and cannot be satisfactorily deconvoluted. Hexagonal $BaCl_2$ is metastable and cannot be grown as bulk crystals, so its luminescent properties outside of a glass matrix are not known [62, 63]. Therefore the effect of the glass matrix on absorption cannot be determined. The addition of divalent europium in the form of $EuCl_2$ does not significantly alter the emission spectrum (see Figure 11b), but eliminates some of the luminescent pathways at the lower end of the UV spectrum, while simultaneously creating new transitions at higher UV wavelengths (see Figures 12a and 12b).

The excitation spectra of the FCZ glass ceramic doped with divalent europium more closely matches the solar spectrum at the earth's surface than the excitation spectrum

of the undoped sample (see Figure 12). This feature of the europium doped glass ceramic makes it suitable for the process of downshifting higher energy ultraviolet light to lower energy visible light, which can be more readily used by photovoltaic cells.

The addition of trivalent holmium doping in the form of HoF_3 has little effect on the excitation spectra of the glasses in the ultraviolet region when measuring the emission at 470 nm (see Figure 13); the shape of the spectrum in this region is almost entirely determined by whether or not europium is present. A small peak centered at 360 nm is the most noticeable change. This peak is only present in the co-doped samples and can be attributed to energy exchange from the Ho^{3+} ions, which absorb strongly at this wavelength, to the $BaCl_2:Eu^{2+}$ luminescent center, which is responsible for the emission centered at 470 nm. Co-doping the samples very noticeably changes the excitation spectra in the visible region, with increasing emission at excitation wavelengths of 425 nm or greater. This feature of the co-doped excitation spectra can also be explained by energy exchange between the Ho^{3+} ions and the $BaCl_2:Eu^{2+}$ luminescent center due to the strong absorption of Ho^{3+} centered at around 450 nm, which can be seen in the spectrophotometry results presented later in this chapter.

The emission spectra for the glass-ceramic samples see several changes with the addition of trivalent holmium (see Figure 14). An emission peak centered at 545 nm appears and grows in intensity with increased holmium content. This emission is likely due to two causes: direct excitation of the holmium ion at the 360 nm wavelength and partial absorption of europium doped $BaCl_2$ nanocrystal emission at the peak centered at 470 nm.

The small peak centered at 410 nm on the europium doped samples is not present in the samples that are undoped or singularly doped with holmium. Because this emission increases with increasing holmium content, energy exchange between the two luminescent centers is likely. One possible route is energy transfer from the Ho^{3+} ion to the Eu^{2+} ion where it emits due to the 4f-5d electronic transition.

The emission spectrum for the sample that is singularly doped with holmium does not exhibit the large broad peak centered at 470 nm seen in the other spectra. This result indicates that the 470 nm emission is dependent upon energy exchange between the $BaCl_2$ nanocrystals and the divalent europium when excited with ultraviolet light (360nm).

The holmium doped samples all have an emission peak centered at 545 nm due to the presence of Ho^{3+} ions in the glass matrix that increases in relative intensity with increased holmium doping percentage. This phenomenon is advantageous because lower energy light, nearer the bandgap energy of the PV cell (1.1 eV or 1127 nm [26]), is converted to electricity by photovoltaic cells with reduced heating of the cell, thereby increasing cell efficiency.

The presence of holmium creates a disruption in the emission curve centered at approximately 450 nm in the emission spectrum of the co-doped samples [64]. Holmium has a strong absorption band in this region of the spectrum; the absorption at 450 nm likely contributes to the emission seen at 545 nm.

It should be noted that in past studies of samples that were made in a similar fashion to those discussed here, amounts of trivalent europium were detected even though only divalent europium compounds were used in sample preparation; this was attributed to oxidation [65]. Nonetheless, trivalent europium is not present in sufficient quantity in the samples discussed here to produce measureable emission in the yellow to red region of visible light, where trivalent europium emits with the greatest intensity [54].

The undoped glass did not exhibit any significant luminescence before heat treatment. In addition, all emission could be assigned to either $BaCl_2$, $BaCl_2:Eu^{2+}$, or Ho^{3+} in the heat treated glass-ceramic samples. Therefore, no emission is attributed to the glass matrix.

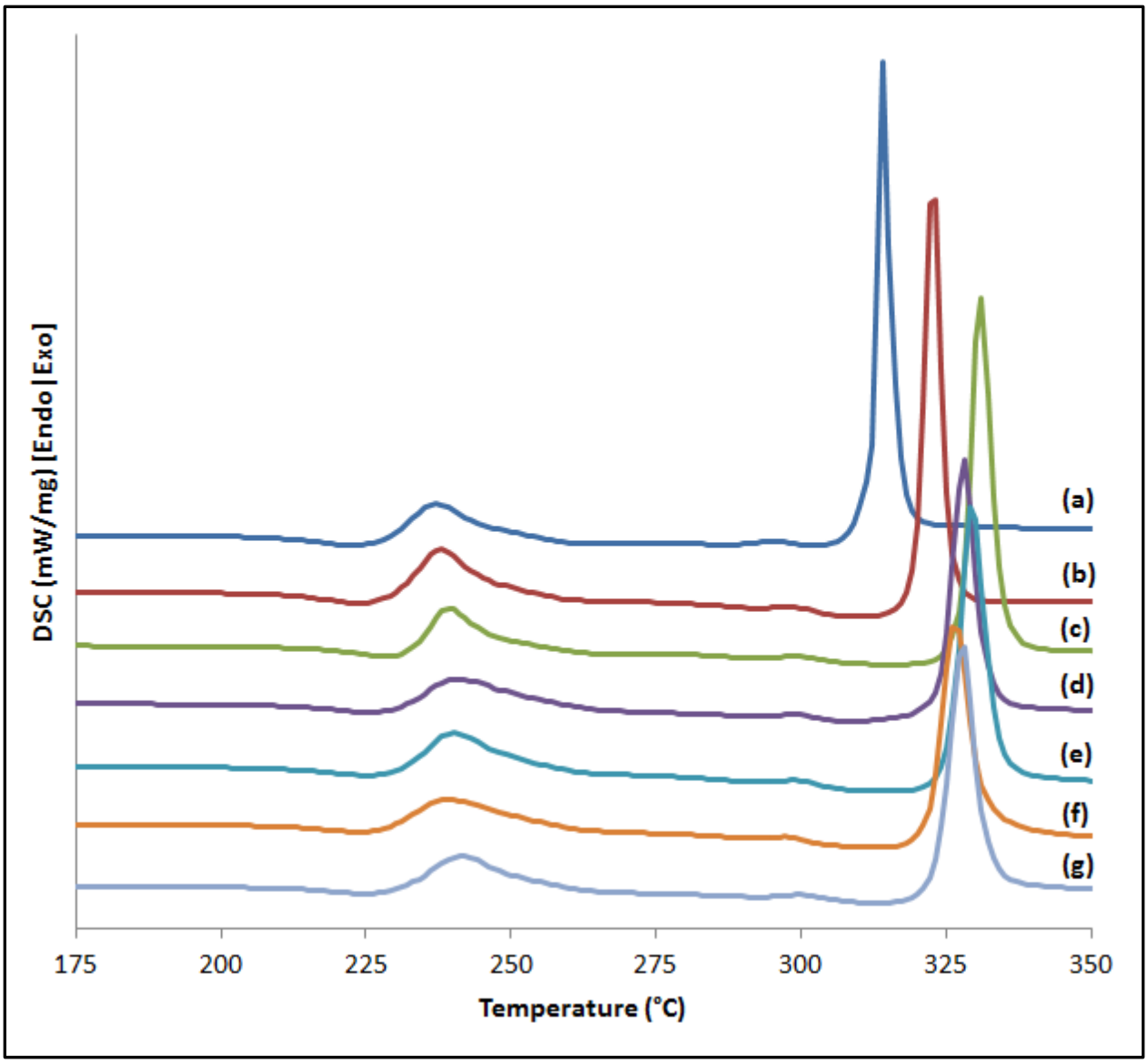

Figure 9. DSC scans for (a) an undoped FCZ glass and (b-g) FCZ glasses doped as follows: (b) 0.0% HoF_3 / 2.0% $EuCl_2$, (c) 0.4% HoF_3 / 1.6% $EuCl_2$, (d) 0.8% HoF_3 / 1.2% $EuCl_2$, (e) 1.2% HoF_3 / 0.8% $EuCl_2$, (f) 1.6% HoF_3 / 0.4% $EuCl_2$, and (g) 2.0% HoF_3 / 0.0% $EuCl_2$. The data are stacked for clarity.

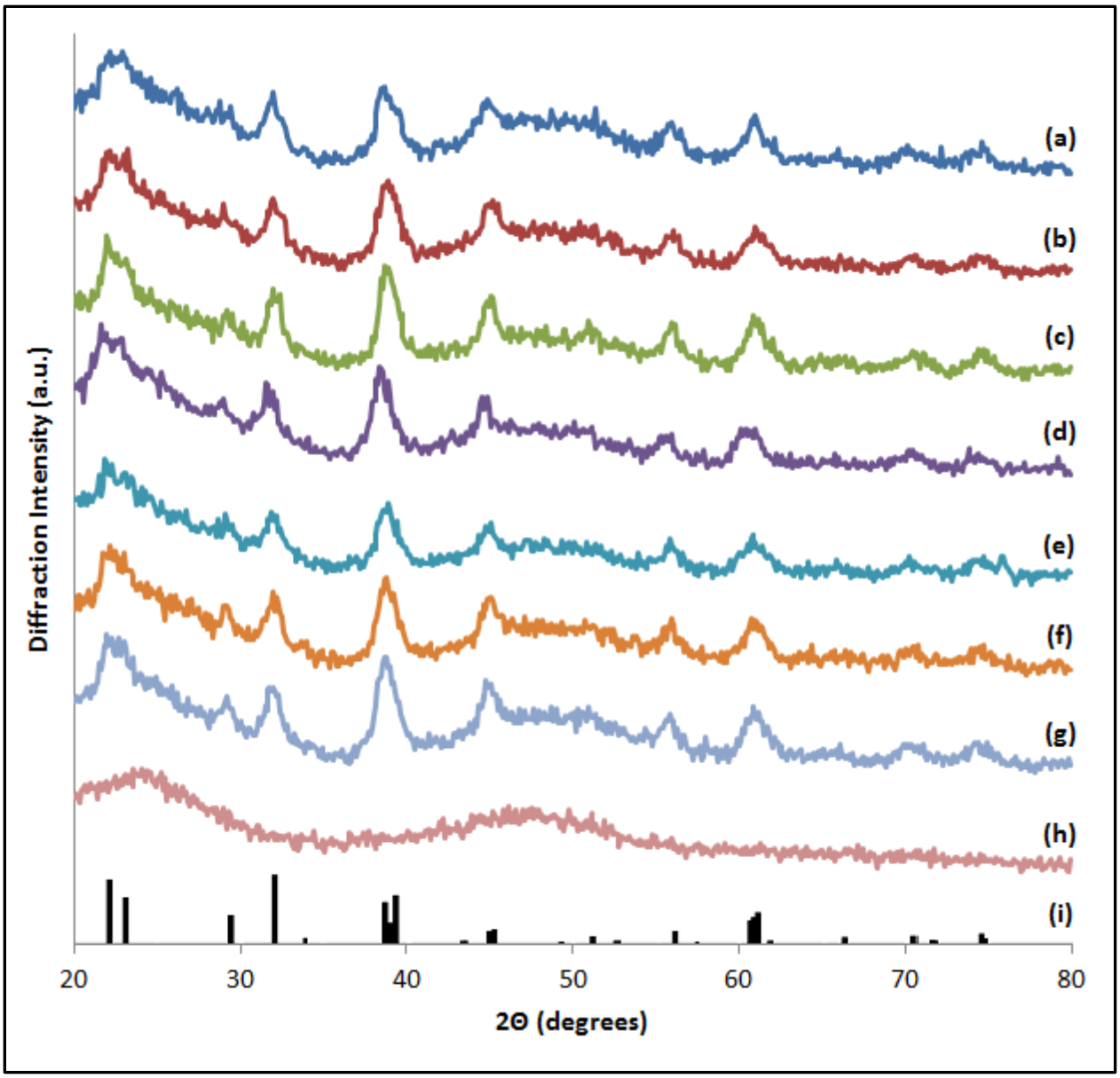

Figure 10. X-ray diffractograms for: (a) an FCZ glass ceramic containing undoped barium chloride nanocrystals, (b-g) an FCZ glass ceramic containing barium chloride nanocrystals doped as follows: (b) 0.0% HoF_3 / 2.0% $EuCl_2$, (c) 0.4% HoF_3 / 1.6% $EuCl_2$, (d) 0.8% HoF_3 / 1.2% $EuCl_2$, (e) 1.2% HoF_3 / 0.8% $EuCl_2$, (f) 1.6% HoF_3 / 0.4% $EuCl_2$, (g) 2.0% HoF_3 / 0.0% $EuCl_2$, (h) an FCZ glass that has not been heat treated, and (i) the pattern for hexagonal phase $BaCl_2$ (PDF 45-1313). The data are stacked for clarity.

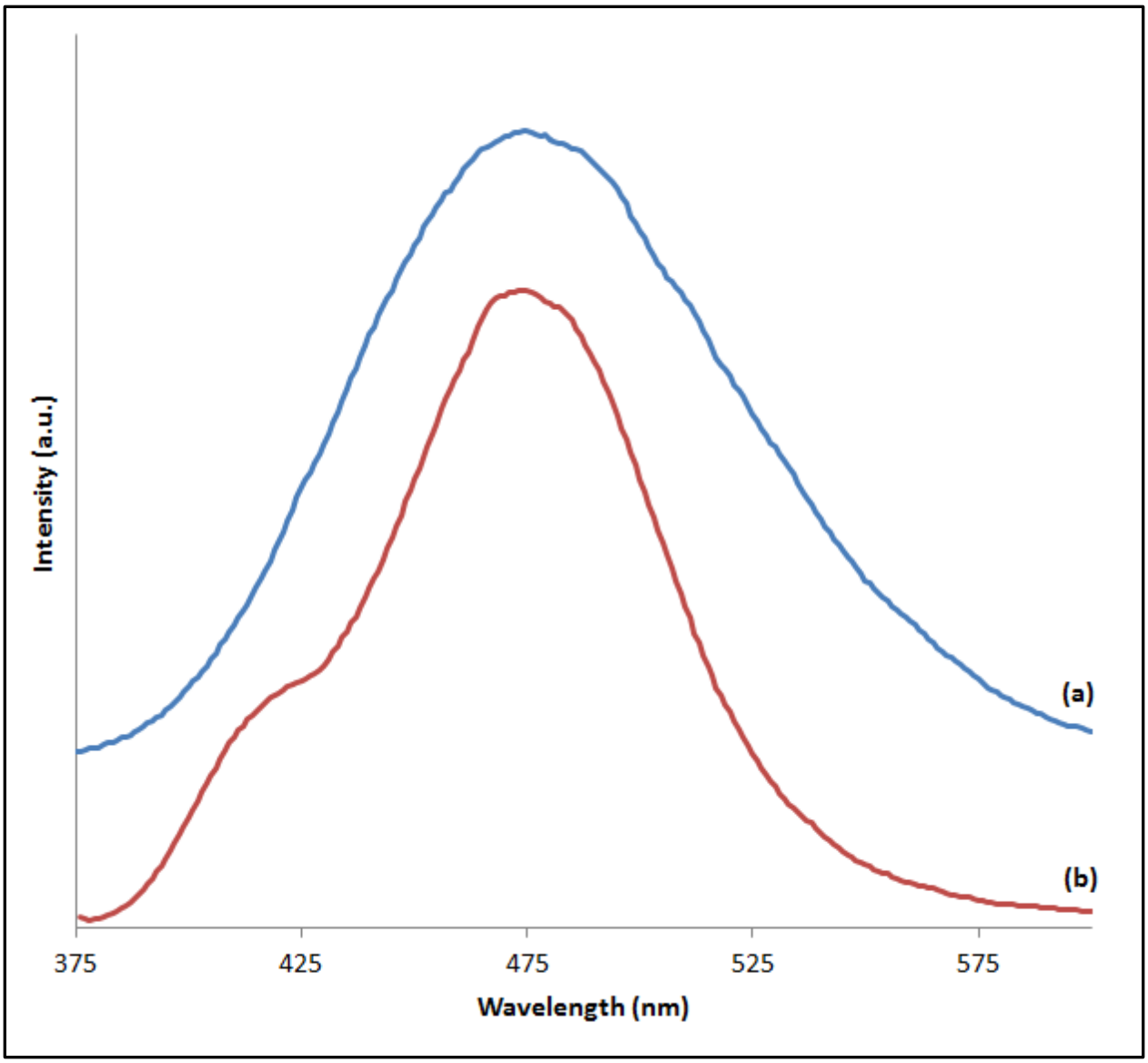

Figure 11. Normalized emission spectra for FCZ glass ceramics containing (a) undoped and (b) 2.0% $EuCl_2$ doped barium chloride nanocrystals. The undoped sample was excited at 270nm; the doped sample was excited at 360 nm. The spectra are stacked for clarity.

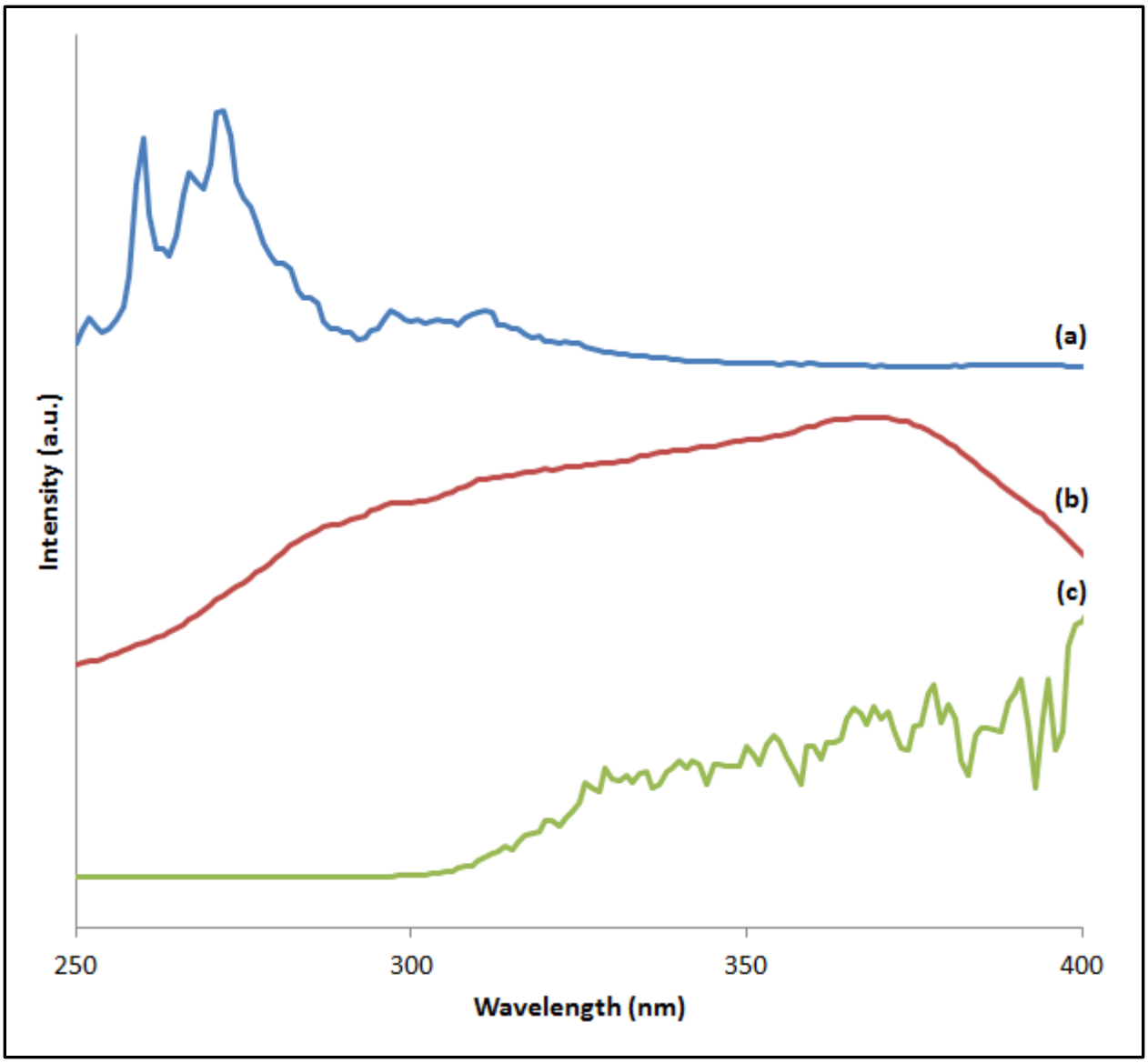

Figure 12. Normalized excitation spectra for 470 nm emission for FCZ glass ceramics containing (a) undoped and (b) 2.0% $EuCl_2$ doped barium chloride nanocrystals. The global solar spectrum with 37° south facing tilt (c) [28]. The spectra are stacked for clarity.

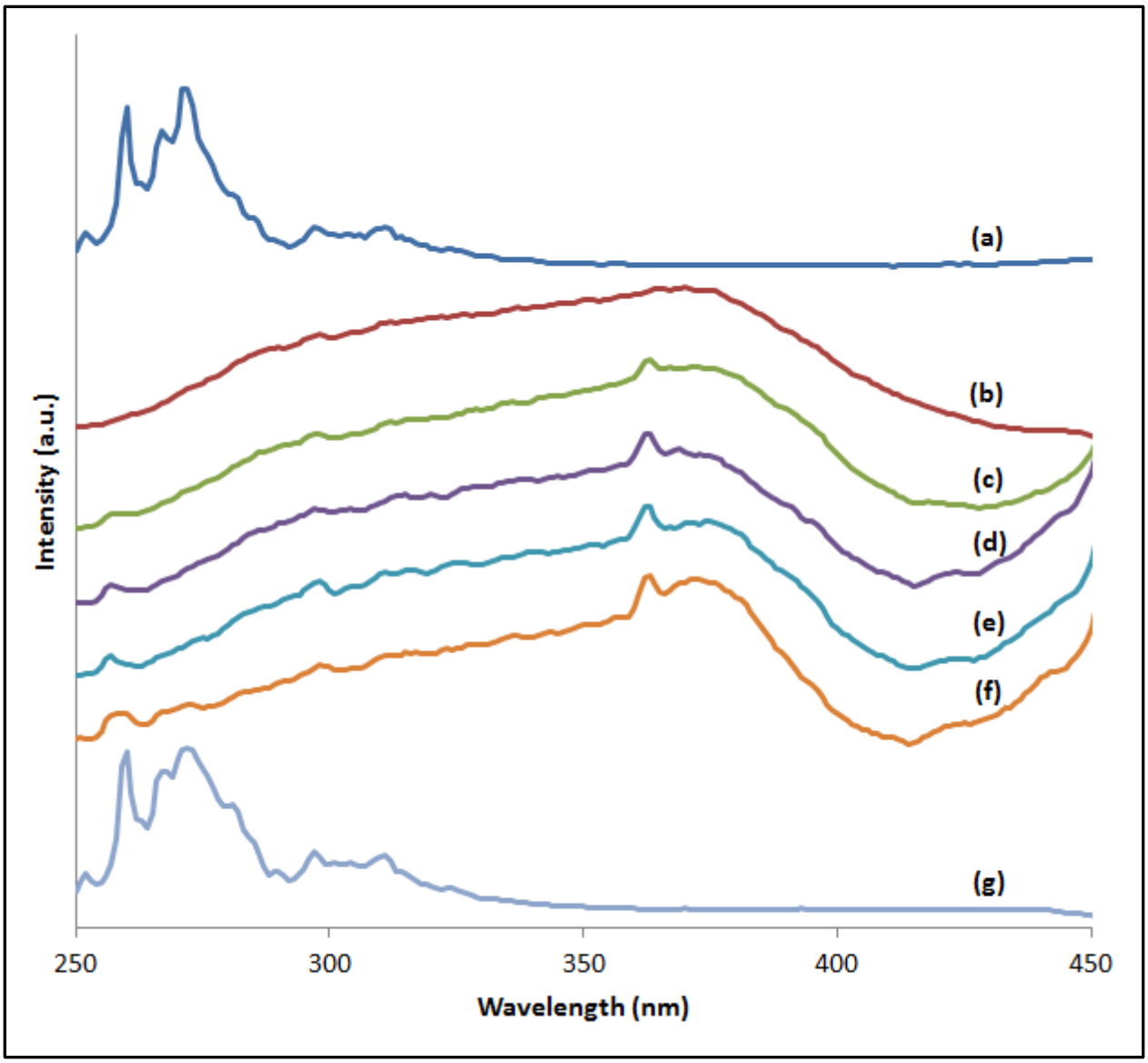

Figure 13. Normalized excitation spectra for: (a) an FCZ glass ceramic containing undoped barium chloride nanocrystals, (b-g) an FCZ glass ceramic containing barium chloride nanocrystals doped as follows: (b) 0.0% HoF_3 / 2.0% $EuCl_2$, (c) 0.4% HoF_3 / 1.6% $EuCl_2$, (d) 0.8% HoF_3 / 1.2% $EuCl_2$, (e) 1.2% HoF_3 / 0.8% $EuCl_2$, (f) 1.6% HoF_3 / 0.4% $EuCl_2$, and (g) 2.0% HoF_3 / 0.0% $EuCl_2$. Emission was measured at 470 nm for all samples. The data are stacked for clarity.

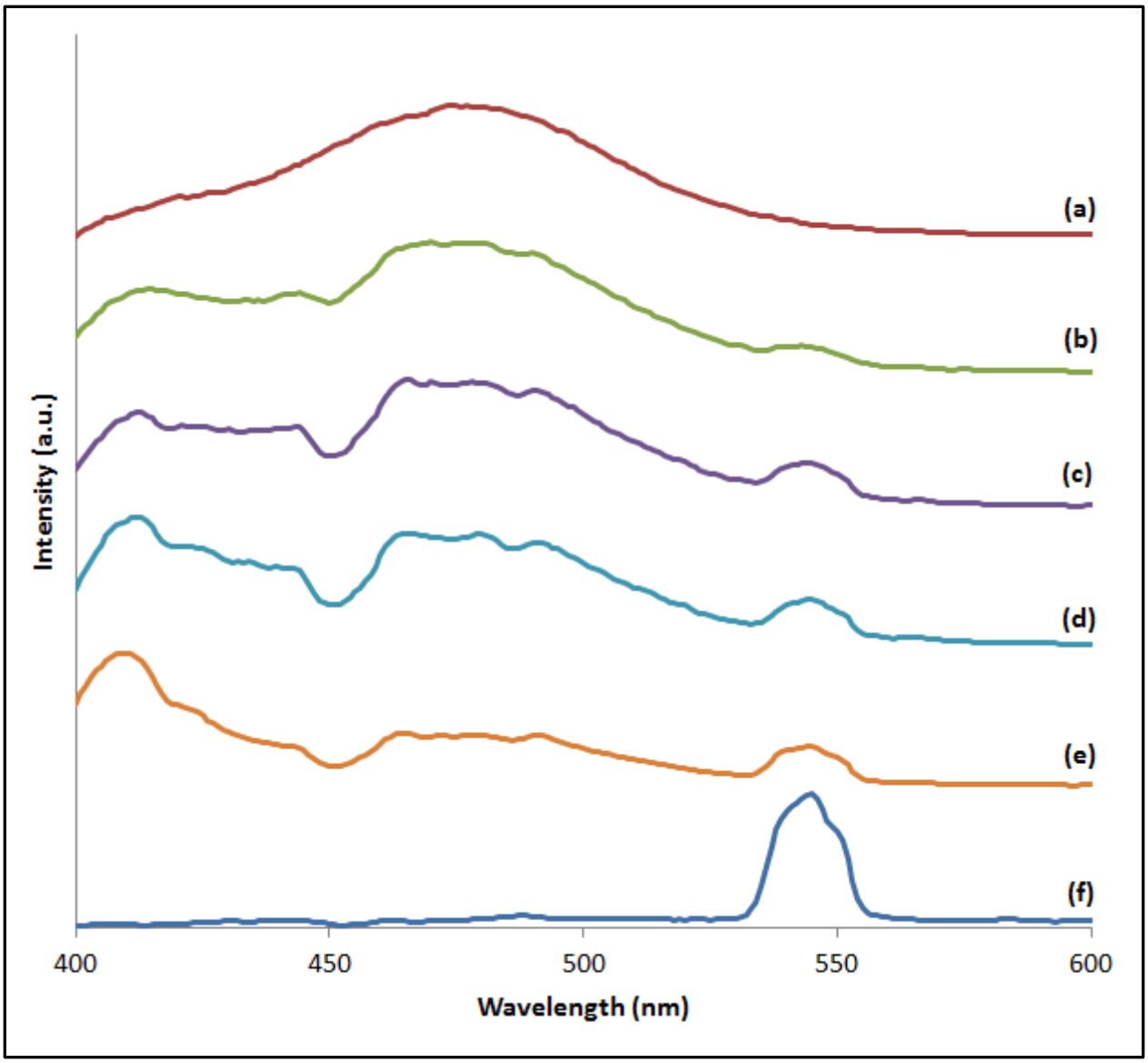

Figure 14. Normalized emission spectra for: FCZ glass ceramic containing barium chloride nanocrystals doped as follows: (a) 0.0% HoF_3 / 2.0% $EuCl_2$, (b) 0.4% HoF_3 / 1.6% $EuCl_2$, (c) 0.8% HoF_3 / 1.2% $EuCl_2$, (d) 1.2% HoF_3 / 0.8% $EuCl_2$, (e) 1.6% HoF_3 / 0.4% $EuCl_2$, and (f) 2.0% HoF_3 / 0.0% $EuCl_2$. The samples were excited at 360 nm. The data are stacked for clarity. Emission from the undoped sample was extremely weak and was therefore not included on this graph.

Spectrophotometry

The transmission spectrum for each of the samples is shown in Figure 15. It is clear that the addition of divalent europium changes the transmission spectra of the glasses. Light at wavelengths below about 370 nm is completely absorbed by the glass ceramics containing europium. This property of the europium doped samples could be exploited if the glass ceramic was used as a cover for UV sensitive materials. The addition of trivalent holmium gives rise to several smaller absorptions in the visible spectrum. These absorptions due to holmium will decrease the output of PV cells by reducing some of the incident light; future studies are required to determine if the gains from downshifting will outweigh the losses caused by the holmium absorptions.

Conclusions

The excitation spectra of FCZ glass ceramics containing hexagonal $BaCl_2$ nanocrystals doped or co-doped with divalent europium more closely matches the solar spectrum at the earth's surface than the excitation spectrum of an undoped sample. This feature of europium doped glass ceramics makes them suitable for the process of downshifting to improve the efficiency of polycrystalline silicon photovoltaic cells. The addition of holmium to the glass ceramics gives rise to additional emission at higher wavelengths and nearer to the band gap energy of polycrystalline silicon photovoltaic cells, reducing heating of the cells and thereby increasing cell efficiency. Additionally, the strong absorption by europium in the ultraviolet region of the spectrum may allow these glass ceramics to serve as a protective layer for ultraviolet sensitive materials.

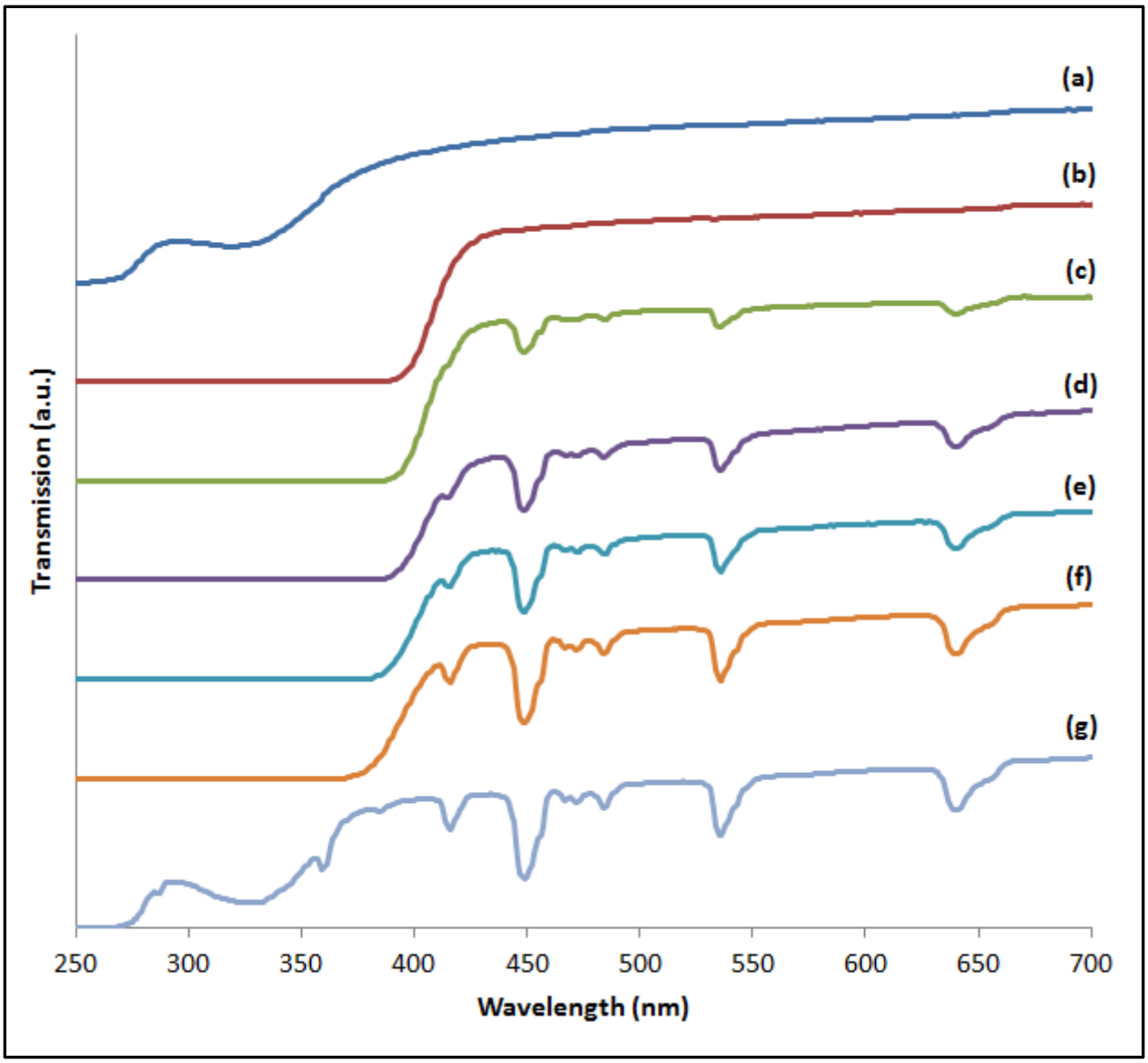

Figure 15. Transmission spectra for: (a) an FCZ glass ceramic containing undoped barium chloride nanocrystals, (b-g) an FCZ glass ceramic containing barium chloride nanocrystals doped as follows: (b) 0.0% HoF_3 / 2.0% $EuCl_2$, (c) 0.4% HoF_3 / 1.6% $EuCl_2$, (d) 0.8% HoF_3 / 1.2% $EuCl_2$, (e) 1.2% HoF_3 / 0.8% $EuCl_2$, (f) 1.6% HoF_3 / 0.4% $EuCl_2$, and (g) 2.0% HoF_3 / 0.0% $EuCl_2$. The data are stacked for clarity.

CHAPTER III:
THE EFFECTS OF SODIUM FLUORIDE CONTENT ON THE PROPERTIES OF FCZ GLASS CERAMICS AND THEIR PERFORMANCE AS STORAGE PHOSPHORS FOR DENTAL RADIOGRAPHY

Russell L. Leonard was responsible for the writing of this chapter and all research activities presented, except as noted: Anthony R. Lubinsky provided the photostimulated luminescence data collected using the 70 kVp source. Jacqueline A. Johnson provided guidance for the overall project.

Abstract

The sodium fluoride content in fluorochlorozirconate (FCZ) glass-ceramic storage phosphor plates was varied to determine the effect on sample properties, including photostimulated light (PSL) output for computed radiography applications, in particular intraoral dental radiography. Differential scanning calorimetry showed that increasing sodium fluoride content, in general, lowered the glass transition, crystallization, and phase transformation temperatures of the as-made glasses. Spectrophotometry results showed an increase in transparency with increased sodium fluoride content. Portions of each glass composition underwent a series of heat treatments in which europium-doped barium chloride crystals in the orthorhombic phase were precipitated to create glass-ceramic storage phosphor imaging plates. The resulting imaging plates were characterized by x-ray diffraction and phosphorimetry to determine the crystalline phases present in each sample for each heat treatment temperature. Visual inspection showed loss of transparency at lower heat treatment temperatures for samples with higher sodium fluoride content. Photostimulated luminescence decay curves were generated for each sample after exposure to x-ray radiation from a copper anode x-ray source operating at 45 kVp. In addition, select samples were evaluated using a 70 kVp x-ray source, which provided energies more similar to those used in intraoral dental radiography. There is a complex relationship between PSL light output and sodium fluoride content in the samples. Samples with intermediate amounts of sodium fluoride (15, 20, and 25 percent) had the greatest light output. It is hypothesized that a phase that forms with partial crystallization of the glass matrix consumes the barium chloride crystals before they can fully transform into the orthorhombic phase in the sample with the lowest amount of sodium fluoride, thus, greatly reducing its PSL light output; this

phenomenon also affects the performance of the other samples, but to a lesser degree. The PSL light output of the samples was insufficient for intraoral dental radiography, but may be suitable for other applications such as nondestructive testing, where dose is not a primary concern.

Introduction

Fluorochlorozirconate (FCZ) based glass ceramics have shown promise in a variety of applications including medical imaging, nondestructive testing, and photovoltaic applications [18, 19, 21, 66, 67]. Compositions are typically modified ZBLAN glasses with an amount of chlorine added to the composition, so that $BaCl_2$ can be precipitated within the glass matrix, creating an optically-active glass ceramic [23, 25, 57, 68]. Typically the crystals are doped with rare earth elements for increased performance [7, 16, 20, 59].

The phase of the $BaCl_2$ crystals present in the glass ceramic has a strong effect upon the luminescent properties of the material. FCZ glass ceramics with $BaCl_2$:Eu^{2+} in the orthorhombic phase have shown much potential in storage phosphor applications [18, 19, 69]. FCZ glass ceramics with hexagonal phase $BaCl_2$:Eu^{2+} have much lower storage phosphor performance and are better suited for scintillation or downshifting applications [6, 12, 66].

ZBLAN, consisting of the fluorides of zirconium, barium, lanthanum, aluminum, and sodium, is the most stable heavy metal fluoride glass [70, 71]. Zirconium is the network former with all other cations serving as network modifiers that increase the stability of the glass during synthesis. Multivalent cations such as indium or tin are sometimes also added to prevent reduction of the zirconium in the melt [22]. Sodium content has been shown to influence the stability of fluorozirconate glasses during synthesis and also to affect the properties of the resulting glass [72, 73]. To the author's knowledge, however,

the influence of sodium on the properties of FCZ glass and glass ceramics has not been studied.

In this study, the effects of sodium content on FCZ glasses and glass ceramics are explored, with particular interest given to storage phosphor performance for computed radiography applications. A series of glass samples was made with varying amounts of NaF used in their synthesis. The as-made glasses were characterized by differential scanning calorimetry (DSC) and spectrophotometry. In order to make an optically-active glass ceramic storage phosphor, portions of each glass composition were heat treated to precipitate orthorhombic $BaCl_2$:Eu^{2+} crystals within the samples. Each sample was heat treated at a series of temperatures so that the optimum temperature for maximum storage phosphor efficiency could be found. X-ray diffraction (XRD) and phosphorimetry were used to determine the phase(s) of $BaCl_2$ present in each heat treated sample. Photostimulated luminescence (PSL) studies were conducted using a copper anode x-ray tube operating at 45 kVp and 40 mA to determine how the PSL light output of the FCZ glass ceramics varied with composition and heat treatment temperature. Select samples were additionally compared against commercial storage phosphors plates at energies (70 kVp) typical for intraoral dental radiography.

Materials and Methods

A series of FCZ glass samples were prepared for this research with a composition in mole percentage as shown in Table 2. Excluding NaF, the chemicals used in the composition had a relative ratio of $51.0ZrF_4$-$20.0BaCl_2$-$3.5LaF_3$-$3.0AlF_3$-$0.5InF_3$-$0.8EuCl_2$-$1.2HoF_3$. The NaF content was varied for each sample: 10, 15, 20, 25, and 30% on a molar basis.

The samples were prepared in an argon atmosphere using a glove box (MBRAUN Labmaster SP) with a connected tube furnace (see Figure A1 in the Appendix). The samples were synthesized in a two-step process. In the first step, all ingredients,

excluding $BaCl_2$, $EuCl_2$, and HoF_3, were melted together at a temperature of 800 °C. In the second step the remaining chemicals were added and the entire composition was heated to a temperature of 750 °C. Following a 5 minute fining step at 700 °C, the molten glass was poured into a temperature-controlled brass mold preheated to 200 °C that was slowly cooled to 25 °C over a period of 4 hours (see Figure A2 in the Appendix). The combined weight of the raw materials for each sample was 10 grams. The crucible material was platinum. The ingredients were weighed before and after each furnace heating step. The weight of each glass sample was recorded upon removal form the mold.

Transmission spectra for the polished raw glass samples were collected using a GenTech Scientific TU-1901 double beam ultraviolet/visible light spectrophotometer with UVWin 5.0.4 software. The samples were scanned from 200 to 900 nm with 1.0 nm increments. Interchange of the tungsten lamp to the deuterium lamp occurred at 330 nm.

DSC (Netzsch DSC 200 F3) scans were made for each raw glass sample from 100 °C to 400 °C at rates of 1 K per minute. Portions of the glass samples of approximate size 5 mm x 5 mm x 1.6 mm were heat treated in air using a programmable heat treatment system (see Figure A3 in the Appendix). The temperature in the sample chamber was PID controlled, using cartridge heaters as the heat source and thermocouples to monitor the temperature. The samples were first heated to a temperature of 200 °C at a rate of 5 °C per minute and held at that temperature for 10 minutes. The samples were then heat treated to the desired maximum temperature at a rate of 1 °C per minute and held at that temperature for 5 minutes. Afterward the samples were cooled to 25 °C at a rate of 5 °C per minute. A sample heat treatment profile is shown in Figure 16. Table 3 shows the heat treatments for all samples. Initially, heat treatment temperatures were chosen based upon the DSC results.

Table 2. Glass sample compositions.

	Sample 1	Sample 2	Sample 3	Sample 4	Sample 5
ZrF_4	57.37	54.19	51	47.82	44.63
$BaCl_2$	22.5	21.25	20	18.75	17.5
NaF	10	15	20	25	30
AlF_3	3.37	3.19	3	2.81	2.63
LaF_3	3.94	3.72	3.5	3.28	3.06
InF_3	0.56	0.53	0.5	0.47	0.44
$EuCl_2$	0.9	0.85	0.8	0.75	0.7
HoF_3	1.35	1.27	1.2	1.13	1.05

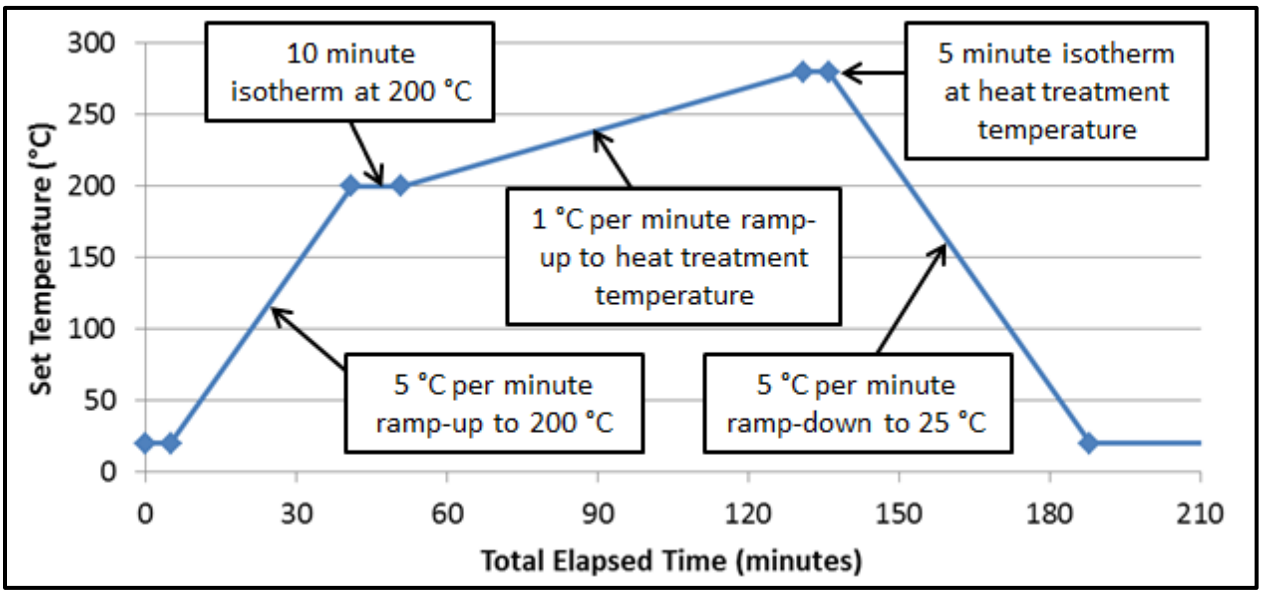

Figure 16. Sample heat treatment temperature profile.

Table 3. Heat treatment temperatures for each sample composition.

Temperature (°C)	10% NaF	15% NaF	20% NaF	25% NaF	30% NaF
270				x	x
275				x	
280			x	x	
285			x	x	
290		x	x	x	x
295		x	x	x	x
300	x	x	x	x	x
305	x	x	x	x	x
310	x	x	x	x	x
315	x		x	x	
320	x	x		x	
325					
330	x	x	x	x	x
335					
340			x	x	x

X-ray diffraction measurement of the raw glass and heat treated samples was performed on a Philips X'Pert MRD X-ray Diffractometer in the 2θ range from 20° to 80°. Scanning rate step size was 0.05° with a time step of 10 seconds. Prior to measurement, the samples were polished to expose the sample bulk. MDI Jade 9 analytical software was used to identify phases.

The excitation and emission spectra for each glass ceramic were determined using a QM-3-PH phosphorescence / fluorescence spectrofluorometer (Photon Technology International, Inc.) with Czerny-Turner monochromators at the source and detector. The system was equipped with a Type L4633 Xenon Flash Lamp (Hamamatsu Photonics K.K.) and an R1527P Photomultiplier tube (Hamamatsu Photonics K.K.). The computer

interface was a PC equipped with FeliX32 software for data analysis. The measurements in this study were made using the following parameters: step size = 1 nm, integration time = 50 µs, averages (number of repeated scans for which results are averaged) = 3, shots (lamp pulses per each individual scan with results averaged) = 50, lamp frequency = 100 Hz.

Photostimulated emission characteristics for each glass ceramic were measured using a custom system consisting of a collector cone, a photosensor (photomultiplier tube) module and power supply (Hamamatsu HC124-06 and C7169), a data acquisition card (National instruments NIUSB-6215), and a 532 nm pumped diode Nd/YAG laser operating at 60 mW (see Figure A4 in the Appendix). To measure the emission, the material was first exposed to x-ray radiation from a Cu anode x-tube operating at 45 kVp and 40 mA. Exposure time for each sample was 60 ± 2 s. The samples were transported from the source to the readout system within light-tight containers. Measurement of the PSL signal occurred at 30 ± 1 minutes after exposure for each sample to reduce variation due to dark decay. Matlab software operating on a personal computer was used to collect the data generated. Integrated PSL signal was determined from 10s of data after the initial signal rise; the estimated background was subtracted from these results.

One heat treated sample from each glass composition was additionally tested after exposure by an x-ray source operating at 70 kVp and 200 mA for 2.5 s. There was a 10 mm aluminum filter between the source and imaging plate for removal of soft x-rays. The estimated exposure is 8R. For comparison, measurements were made using commercial storage phosphors produced by Fuji Photo Film Co. (type ST-VI) and Dentoptix, which are used for chest and dental radiography, respectively. To prevent saturation of the detector while testing the commercial phosphors, the exposure was 2.5% and 5% that of the glass ceramic samples for the Fuji and Dentoptix plates respectively; the data was scaled accordingly for comparison, assuming a linear response to dose. The photostimulated emission was measured using a system consisting of a 4” integrating sphere (Labsphere, Inc.), a photosensor module and

power supply (Hamamatsu HC124-06 and C7169), a data acquisition card (National instruments NIUSB-6215), and a 532 nm pumped diode Nd/YAG laser operating at 17 mW. A 3.2 mm diameter portion of the sample was stimulated diffusely from within the integrating sphere; the laser power at the sample was 48 μW. Matlab software operating on a personal computer was used to collect the data generated. As before, measurement of the PSL signal occurred at 30 ± 1 minutes after exposure for each sample to reduce variation due to dark decay. Integrated PSL signal was determined from 196 s of data after the initial signal rise; the estimated background was subtracted from these results.

Results

Mass Loss

During synthesis, there was significant mass loss due to evaporation during both melting steps. Loss at each step was related to the NaF content for each sample, with increased NaF content leading to reduced mass loss (see Figure 17). In addition, the mass loss was greater during the first melting step than the second for all samples. Tabulated results can be found in the Appendix (see Table A1).

This result indicates NaF has an effect on the stability of the molten glass, which is related to the strength of the chemical bonds within. The increased yield resulting from higher NaF content is advantageous in a large-scale, commercial manufacturing environment, where cost is a primary concern.

Spectrophotometry

The transmission spectra for the sample glasses before heat treatment are shown in Figure 18. Various disruptions can be seen in the spectra due to absorptions from the rare earth dopants present in the matrix. Complete opacity at wavelengths less than approximately 380 nm is due to absorption by Eu^{2+}[66]. The sharp absorption bands in

the spectra such as those found at 450, 540 and 640 nm can be attributed to absorption by Ho^{3+} [64, 66].

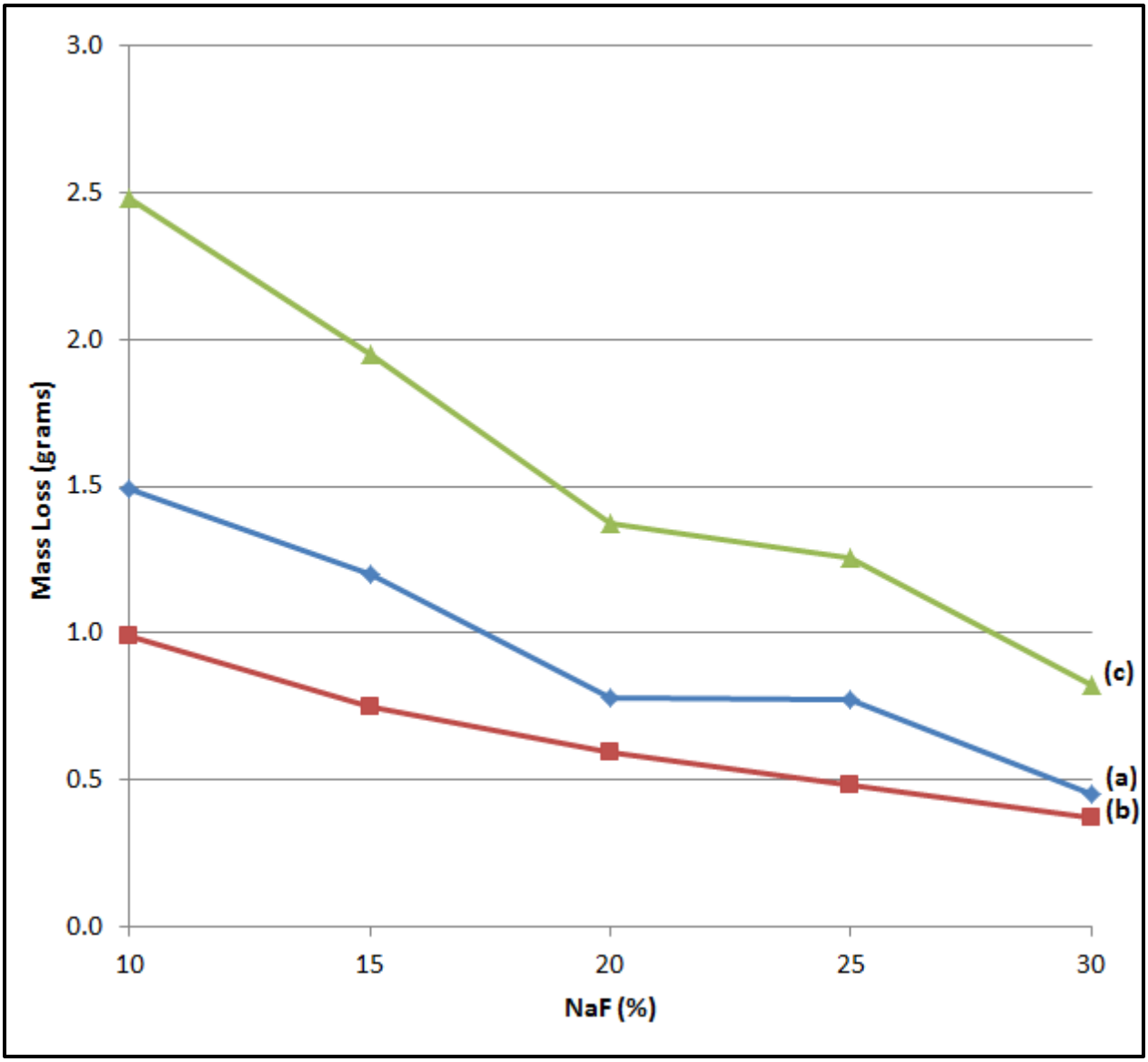

Figure 17. Evaporative mass loss during synthesis in relation to sample sodium fluoride content: (a) during first melt, b) during second melt, and (c) total.

NaF content appears to have a role in the glass transparency. While all samples were similar in appearance, being transparent with a slightly yellow-brown hue, spectrophotometry results showed some variance in light transmission, with the two samples with the lowest sodium content, 10% and 15% NaF, being the least transparent. It is assumed that the NaF content does not affect the glass on the macroscopic scale and any decrease in transparency is due to increased absorption within the material and not due to light scattering losses.

Regions of interest relating to the wavelength of the stimulating laser for PSL and the corresponding PSL emission peak wavelength are shown in Figures 19 and 20, respectively. It is desirable for the materials in storage phosphor applications to be transparent at the wavelengths at which stimulation and subsequent light emission occur. Absorption of the stimulating light away from the luminescent centers (the precipitated $BaCl_2:Eu^{2+}$ nanocrystals in the glass ceramic) is undesirable, as it requires either additional laser fluence or increased stimulation time to collect the same PSL emission as could be accomplished with a non-absorbing matrix. Absorption of PSL emission by the glass matrix decreases signal intensity. For a given imaging system, plates that self-absorb PSL emission will require additional dose (exposure) to generate an equivalent signal, when compared to equivalent plates that do not have this issue. Based upon the spectrophotometry results, it is expected that the sample compositions with higher NaF content, being more transparent, will have an advantage in PSL light output.

Differential Scanning Calorimetry

Plots of the DSC scans at 1K per minute for each glass composition are shown in Figure 21. From the DSC curves, key temperatures relating to crystallization and matrix stability can be extracted (see Figure 22):

- T_g – the glass transition temperature
- $T_{o\text{-}hex}$ – the onset of crystallization for hexagonal $BaCl_2$
- $T_{p\text{-}hex}$ – the peak crystallization temperature for the hexagonal $BaCl_2$
- $T_{o\text{-}ortho}$ – the onset of phase transformation to orthorhombic $BaCl_2$ crystals
- $T_{p\text{-}ortho}$ – the peak temperature for phase transformation to orthorhombic $BaCl_2$ crystals
- $T_{o\text{-}matrix}$ – the onset of partial crystallization of the glass matrix

The compositional changes have a large influence on the thermal characteristics of glasses (see Table 4 and Figure 23). For all compositions, the glass transition temperature decreased with increasing NaF content. For the samples with 15%, 20%, and 25% NaF, hexagonal $BaCl_2$ crystallization, the hexagonal-to-orthorhombic phase transformation, and partial crystallization of the glass matrix occurred at decreasing temperatures with increasing NaF content; the 10% NaF sample, follows the crystallization trends found in the 15%, 20%, and 25% NaF samples, but its hexagonal-to-orthorhombic phase transformation peak is obscured by an overlapping of the matrix crystallization peak. The sample with 30% NaF does not fit the trends for crystallization observed in the other samples and, as with the 10% NaF sample, its hexagonal-to-phase transformation is likewise obscured by a matrix crystallization peak.

The DSC results indicate the increased NaF content increases the mobility of the atoms in the matrix as there is, in general, a decrease in glass transition temperature and crystallization temperature with increased NaF content. The crystallization temperature for the 30% NaF sample does not follow this general trend however. A possible explanation for this deviation from the trend concerns the amount of Ba^{2+} and Cl^- present in each sample composition. As the mole percentage of NaF used in each

composition increases, the amount of the other ingredients decreases. So the sample 30% NaF sample, which has the largest amount of NaF in its composition, also has the least quantity of $BaCl_2$. So while the Ba^{2+} and Cl^- ions may be more mobile in the 30% NaF sample, there are less of them, making the creation of a stable nucleus less likely; with this composition, the lower concentration of the reactants, rather than increased mobility due to the Na^+ content, becomes the more dominant factor in the crystallization kinetics.

As previously mentioned, the 15%, 20% and 25% NaF samples have a detectable exothermic DSC peak associated with the hexagonal-to-orthorhombic phase transformation of the $BaCl_2$ crystals. For the 10% and 30% NaF samples, this event does not occur until partial crystallization of the glass matrix has already begun, which is undesirable.

Visual Inspection of the Samples after the Heat Treatment Process

The heat treated samples are shown in Figure 24 under visible and UV (365 nm) light. For comparison, glass samples that have not been heat treated are also shown. For each composition, the raw glass was transparent with a slight yellow-brown hue. The heat treated samples became less transparent with increased temperature. In addition, the samples became photoluminescent following heat treatment.

Samples with increased amounts of NaF lost transparency at significantly lower heat treatment temperatures that were much closer to the hexagonal-to-orthorhombic phase transformation than those with lesser NaF content. Loss of transparency is attributed to increased $BaCl_2$ crystallite size: larger crystals have increased light scattering, leading to a loss in transmission. Light scattering at the stimulation wavelength is unfavorable in storage phosphors used in computed radiography applications due to its detrimental effect on image spatial resolution. Scattered stimulating light will cause electron-hole pair recombination at locations spatially removed from the pixel being read-out; this result increases the width of the point spread function and decreases spatial resolution for the image being generated.

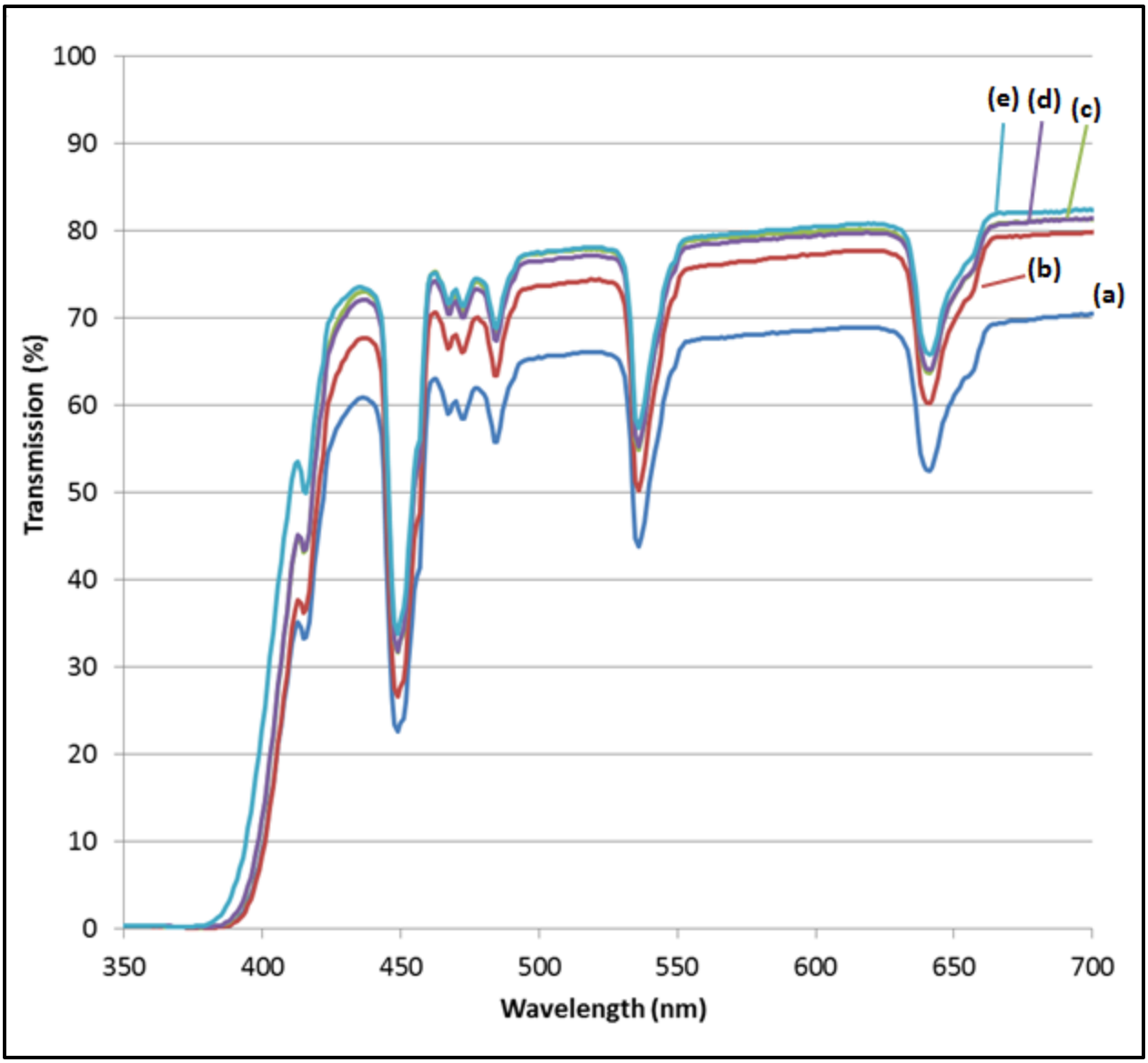

Figure 18. Transmission Spectra for the samples glasses before heat treatment: (a) 10% NaF, (b) 15% NaF, (c) 20% NaF, (d) 25% NaF, and (e) 30% NaF.

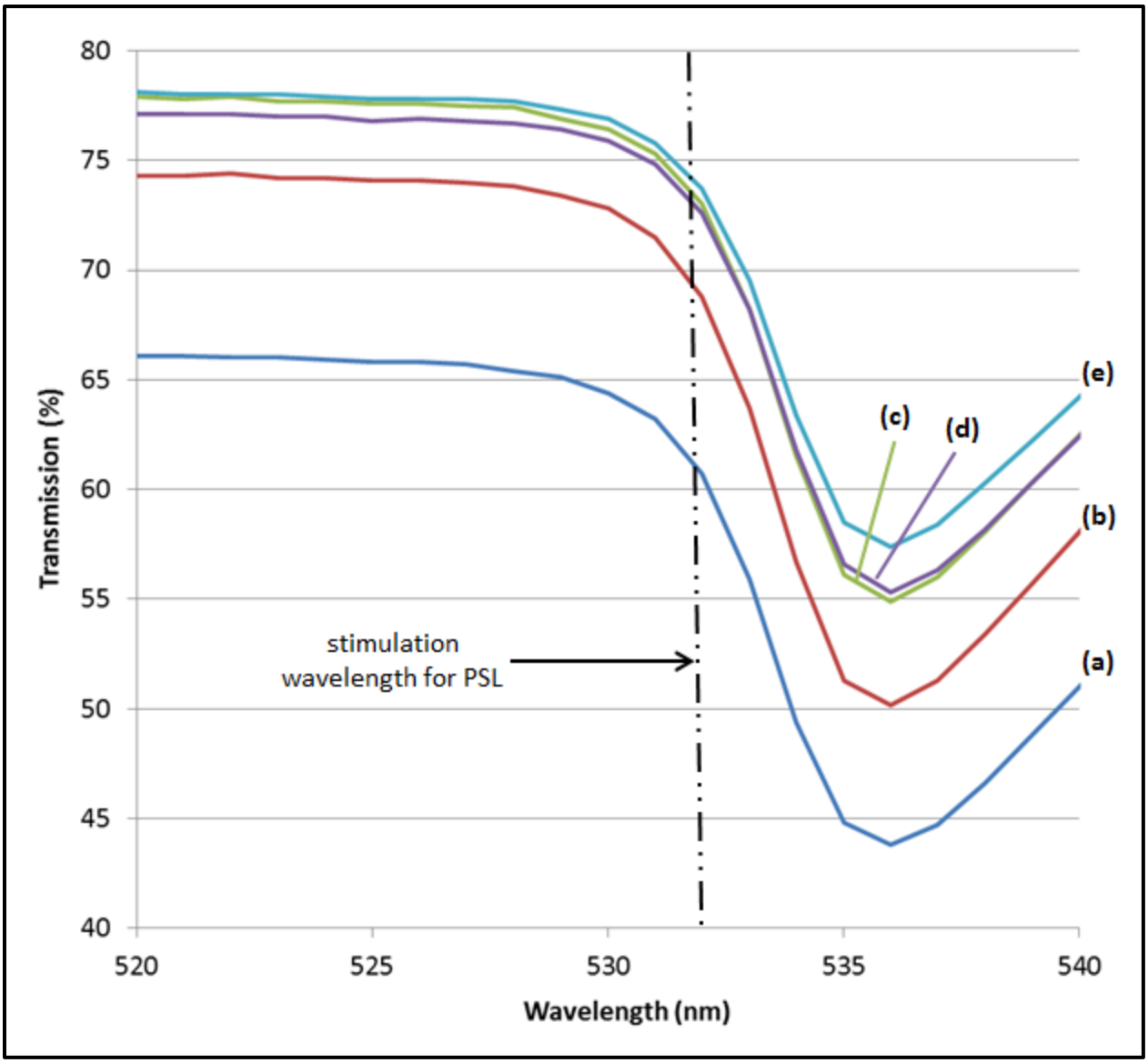

Figure 19. Transmission spectra for the glass samples before heat treatment in the region of interested for photostimulated luminescence with a laser of wavelength 532 nm: (a) 10% NaF, (b) 15% NaF, (c) 20% NaF, (d) 25% NaF, and (e) 30% NaF.

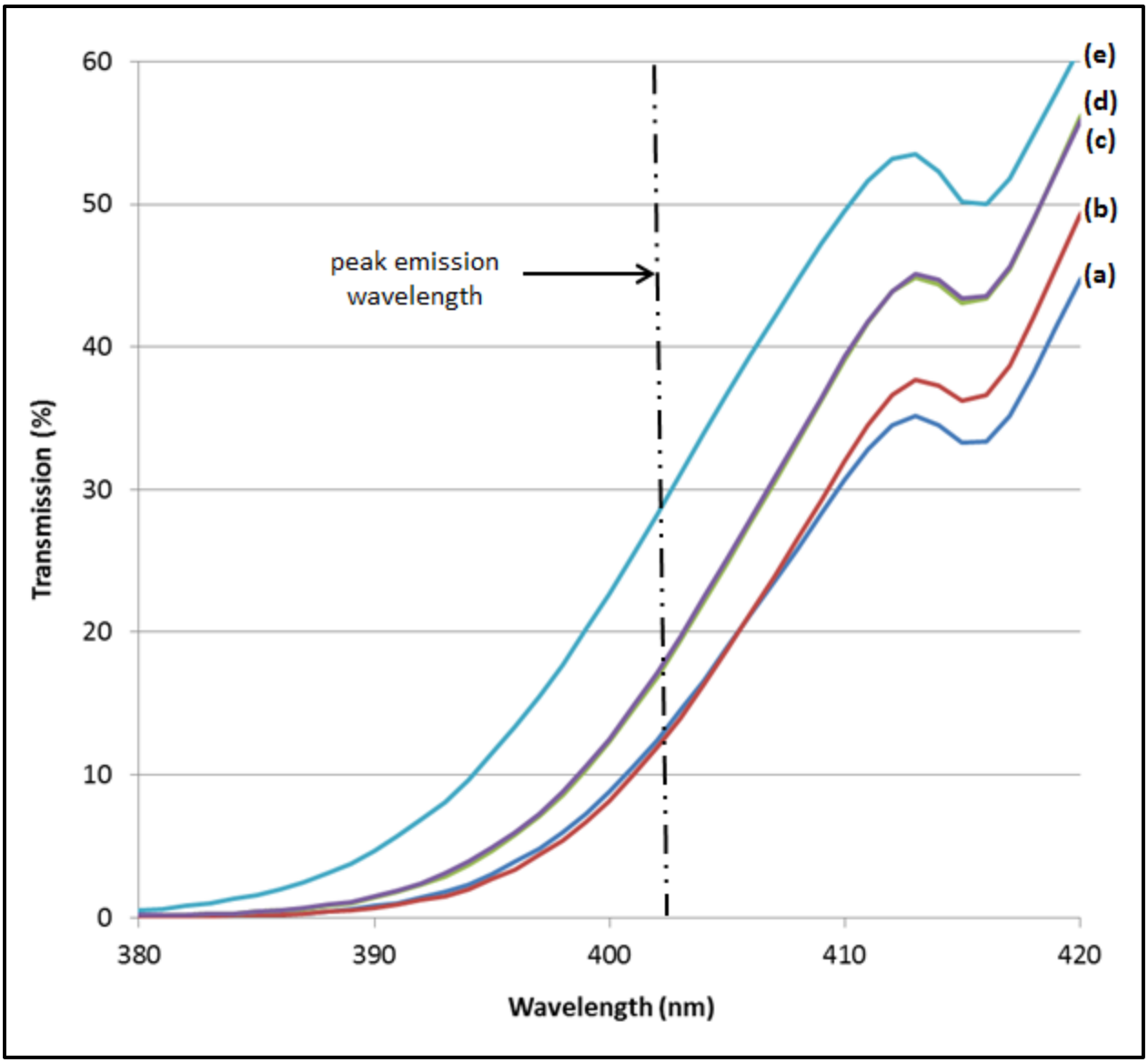

Figure 20. Transmission spectra for the glass samples before heat treatment in the region of interest for photostimulated luminescence with emission centered at ~402 nm: (a) 10% NaF, (b) 15% NaF, (c) 20% NaF, (d) 25% NaF, and (e) 30% NaF.

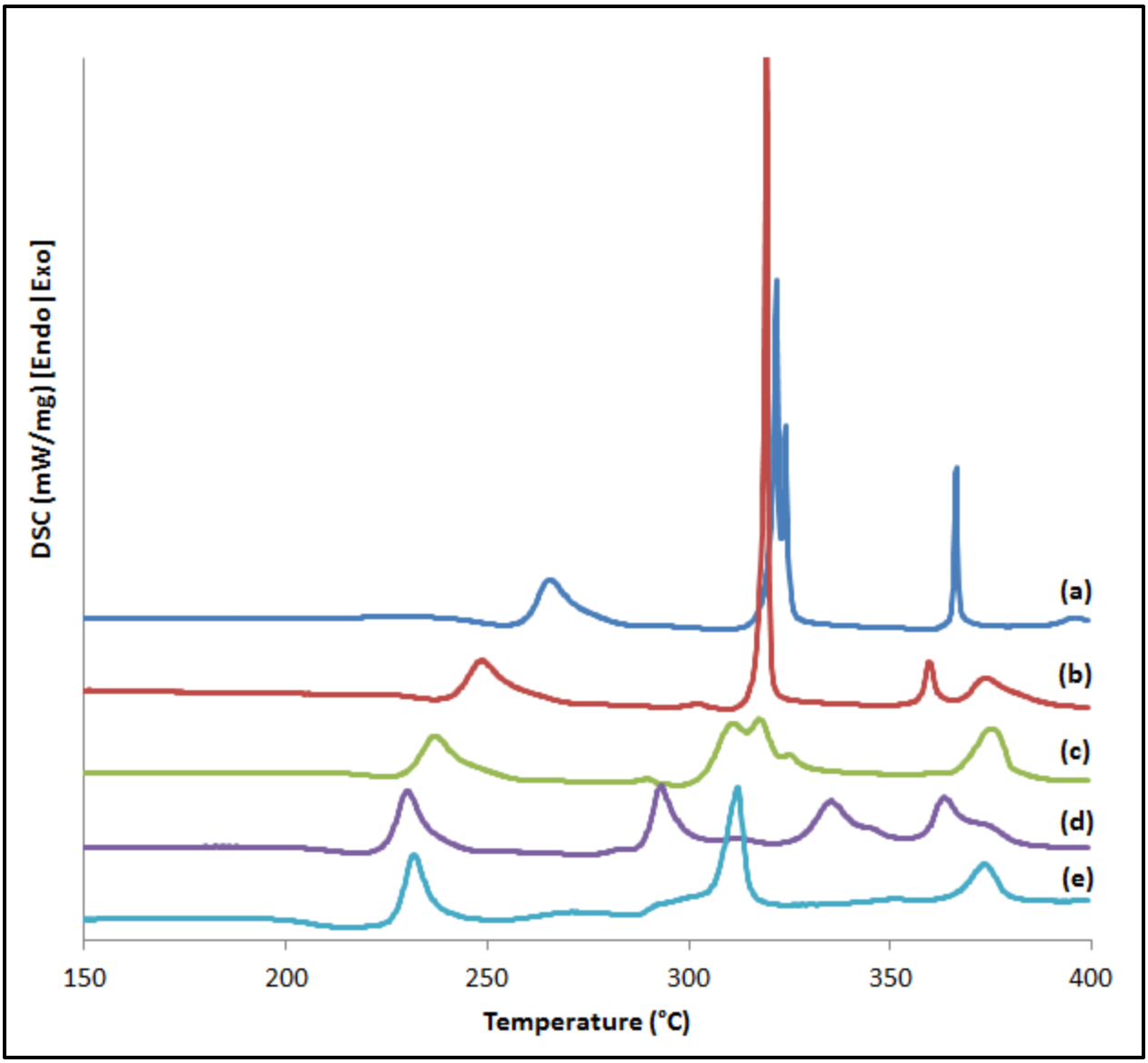

Figure 21. DSC scan at a rate of 1 K per minute for the sample glass: (a) 10% NaF, (b) 15% NaF, (c) 20% NaF, (d) 25% NaF, and (e) 30% NaF.

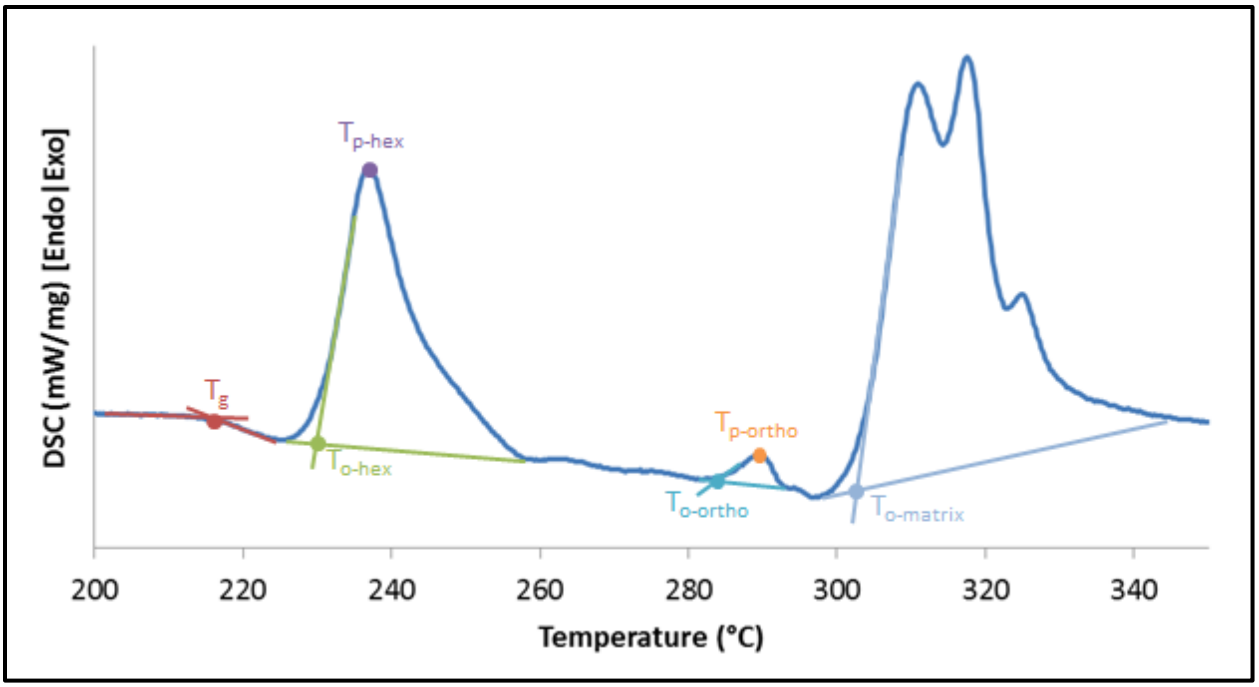

Figure 22. Key temperatures relating to crystallization and glass stability.

Table 4. Key temperatures relating to crystallization and glass stability for each glass composition extracted from the 1K per minute DSC scans.

NaF (%)	10	15	20	25	30
T_g (°C)	239	227	217	203	199
$T_{o\text{-}hex}$ (°C)	259.8	242.4	231	225.1	227.1
T_{p-hex} (°C)	265.4	248.6	236.8	230.2	231.8
$T_{o\text{ - }ortho}$ (°C)	n/a	297.9	285	278.6	n/a
$T_{p\text{-}ortho}$ (°C)	n/a	302.4	289.3	283.1	n/a
$T_{o\text{-}matrix}$ (°C)	320.4	318.5	303.5	289.6	256

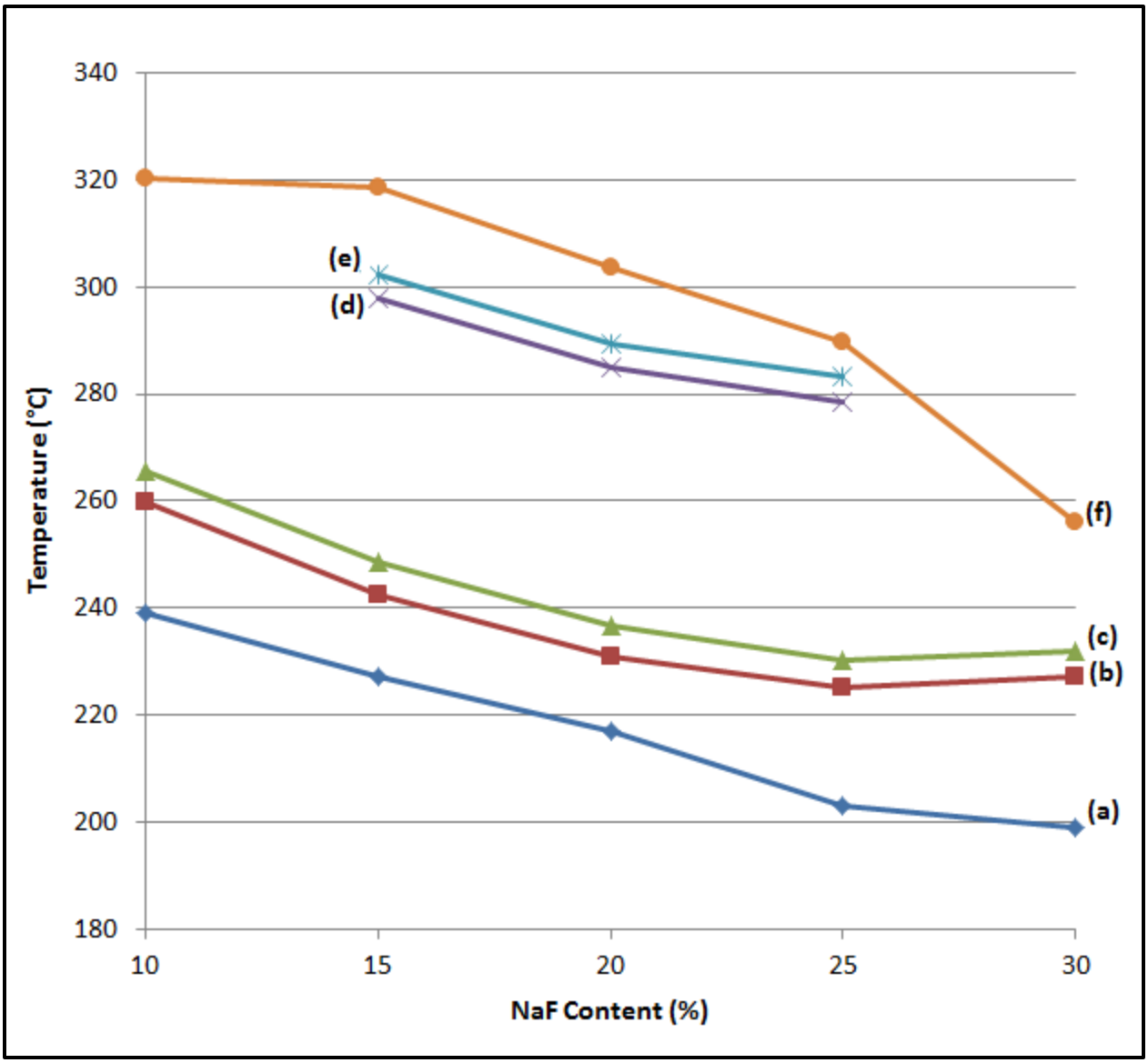

Figure 23. Plots of (a) T_g, (b) $T_{o\text{-}hex}$, (c) $T_{p\text{-}hex}$, (d) $T_{o\text{-}ortho}$, (e) $T_{p\text{-}ortho}$, and (f) $T_{o\text{-}matrix}$ derived from the 1K per minute DSC scan of the raw glass samples as a function of NaF content.

The emission of the samples under UV light progressed from cyan to violet to a dim purple as heat treatment temperature increased. At lower heat treatment temperatures, the cyan emission of the samples is indicative of hexagonal phase $BaCl_2$, while the violet seen at higher temperature heat treatments is indicative of $BaCl_2$:Eu^{2+} in the orthorhombic phase. At the highest heat treatment temperatures, sample emission is greatly reduced; this topic will be addressed in the Discussion section of this chapter.

X-ray Diffraction

For each composition, XRD results for the raw glass and heat treated samples are shown in Figures 25 through 29 along with the peaks, from the literature, for both the hexagonal (Powder Diffraction File PDF 45-1313) and orthorhombic (Powder Diffraction File PDF 24-0094) phase $BaCl_2$ crystals. The diffractograms are somewhat noisy due to the relatively small volume of crystals in each heat treated sample (~20%) and small sample size (~ 5mm × 5mm).

The diffractograms for the raw glass samples are devoid of sharp peaks, due to their amorphous nature. The heat treated samples, however, show many sharp peaks protruding from the amorphous background, indicating that crystallization has occurred. For all compositions at lower heat treatment temperatures, hexagonal phase $BaCl_2$ can be readily identified by prominent peaks at 31.1, 39.3, 45.2, 56.0, and 61.2°. Orthorhombic $BaCl_2$ is more difficult to identify in the diffractograms, and cannot be positively identified in samples with 10% NaF and 30% NaF. For the remaining samples, with 15%, 20%, and 25% NaF, the orthorhombic phase is apparent at intermediate heat treatment temperatures, with the diffraction peaks at 31.0 and 34.2° being most prominent. At the higher heat treatment temperatures, the diffractograms for the samples show additional peaks belonging to crystals other than $BaCl_2$ and a decreased amorphous background, indicating partial crystallization of the glass matrix.

Phosphorimetry

The photoluminescent emission spectra for the heat treated samples are shown in Figures 30 through 34. The spectra follow a similar trend with increasing heat treatment temperature. At lower temperatures, the spectra indicate the presence of a significant volume of hexagonal $BaCl_2$:Eu^{2+} within the samples; the emission from the hexagonal $BaCl_2$:Eu^{2+} can be identified by a large, tall peak centered at approximately 410 nm and a broad peak extending from about 450 to 530 nm [7, 12, 23]. As the heat treatment temperature increases, the position of the large, tall peak shifts to approximately 402 nm and the broad peak diminishes, indicating the $BaCl_2$:Eu^{2+} crystals have transformed into the orthorhombic phase. The phase transformation temperatures from hexagonal to orthorhombic for the $BaCl_2$:Eu^{2+} crystals may therefore be estimated from the data as shown in Table 5, which are in strong agreement with the DSC results (see Table 4). The presence of Ho^{3+} in the sample also affects the emission spectra of the samples, most notably the emission peak centered at approximately 545 nm[66]. Ho^{3+} also causes several disruptions in the spectra that can be clearly seen at 415, 450, and 485 nm. These disruptions are the result of the Ho^{3+} ions absorbing some of the $BaCl_2$:Eu^{2+} emission and match the spectrophotometry results (transmission spectra) for the glass samples prior to heat treatment.

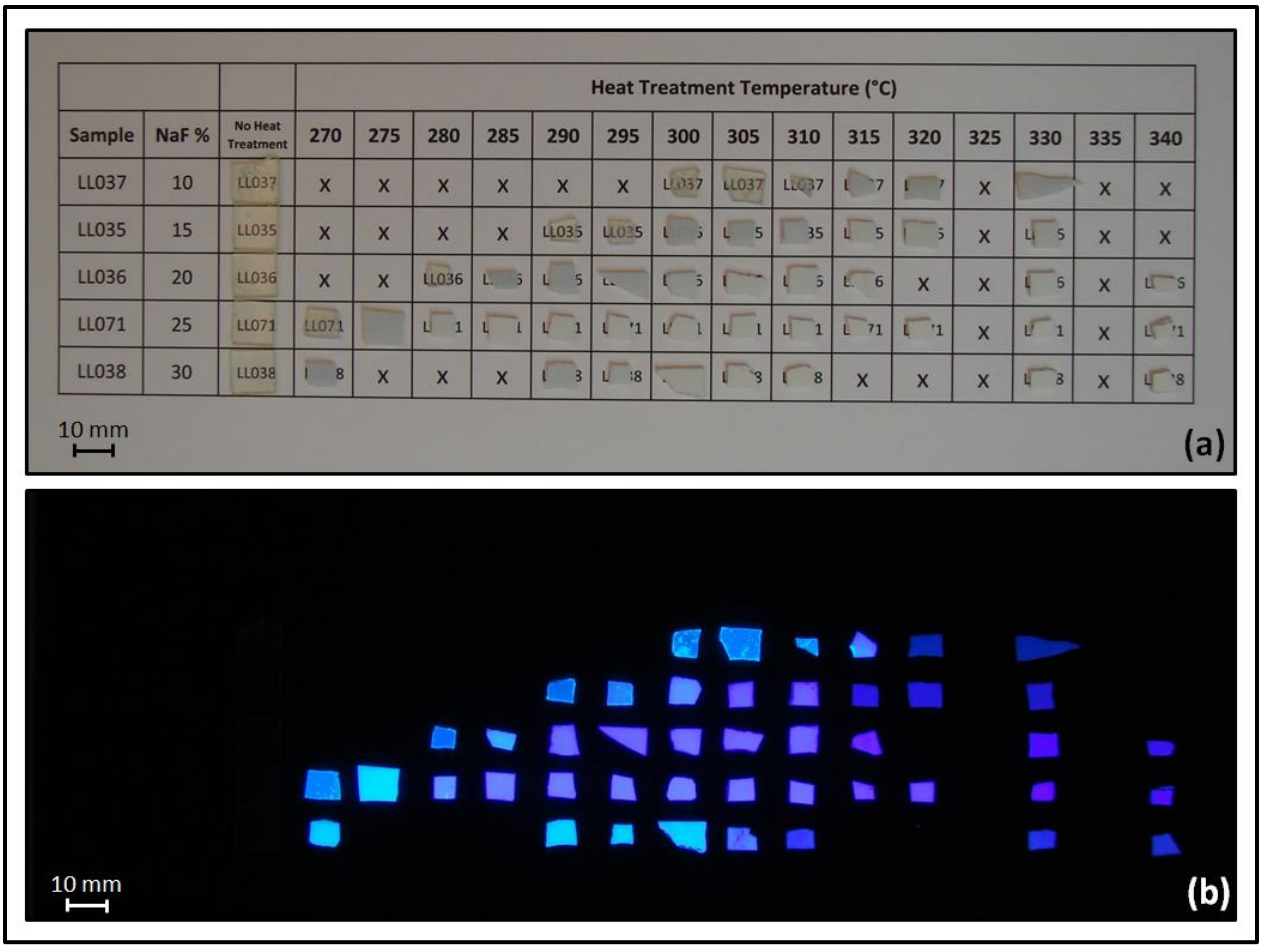

Figure 24. Photographs of the as-made and heat treated samples for each composition under (a) visible and (b) 365 nm UV light. Locations without a sample are marked with an "X".

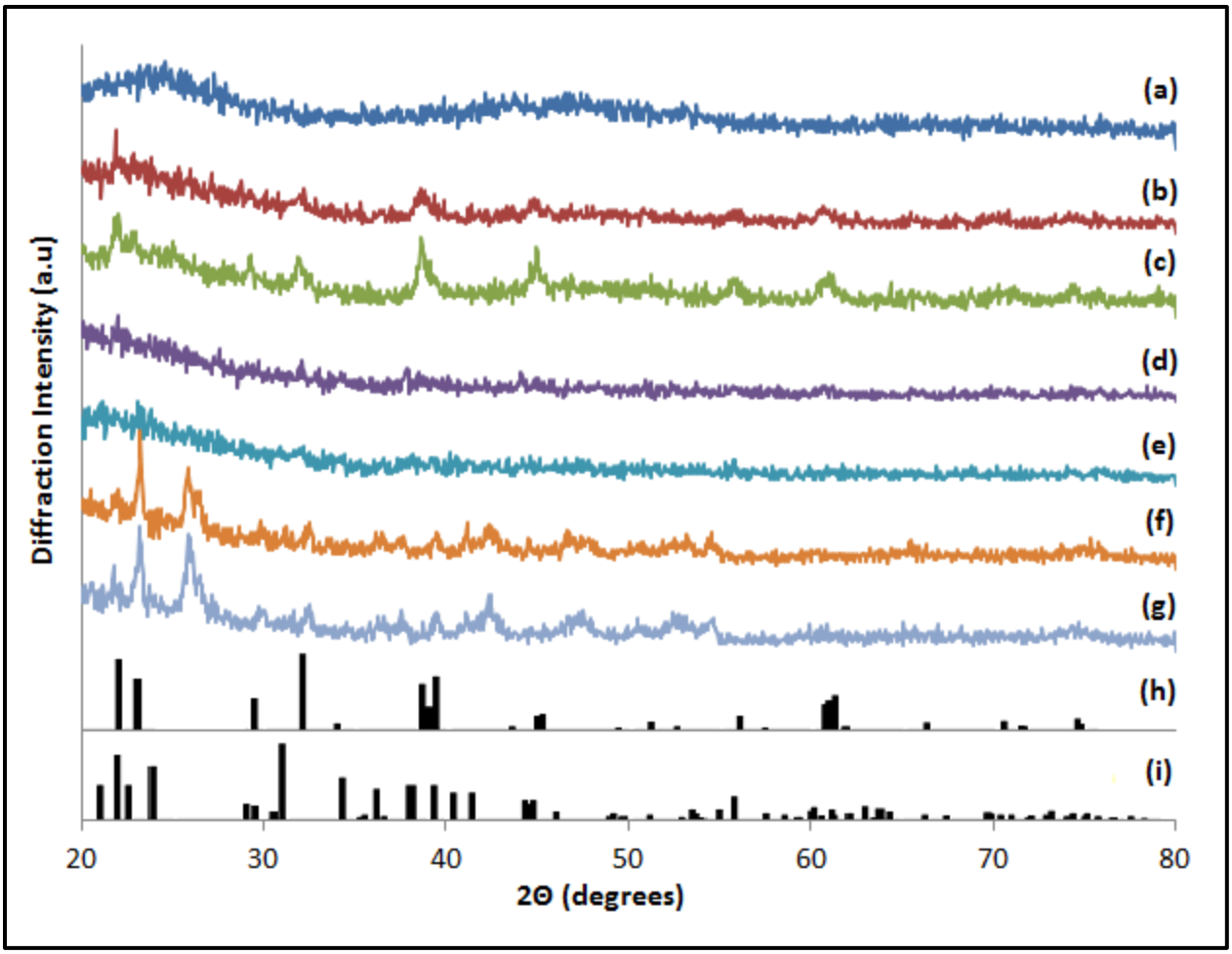

Figure 25. XRD Results for the 10% NaF sample: a) raw glass, samples heat treated to (b) 300, (c) 305, (d) 310, (e) 315, (f) 320, and (g) 330 °C, (h) the pattern for hexagonal phase BaCl2 (PDF 45-1313), and (i) the pattern for orthorhombic phase BaCl2 (PDF 24-0094).

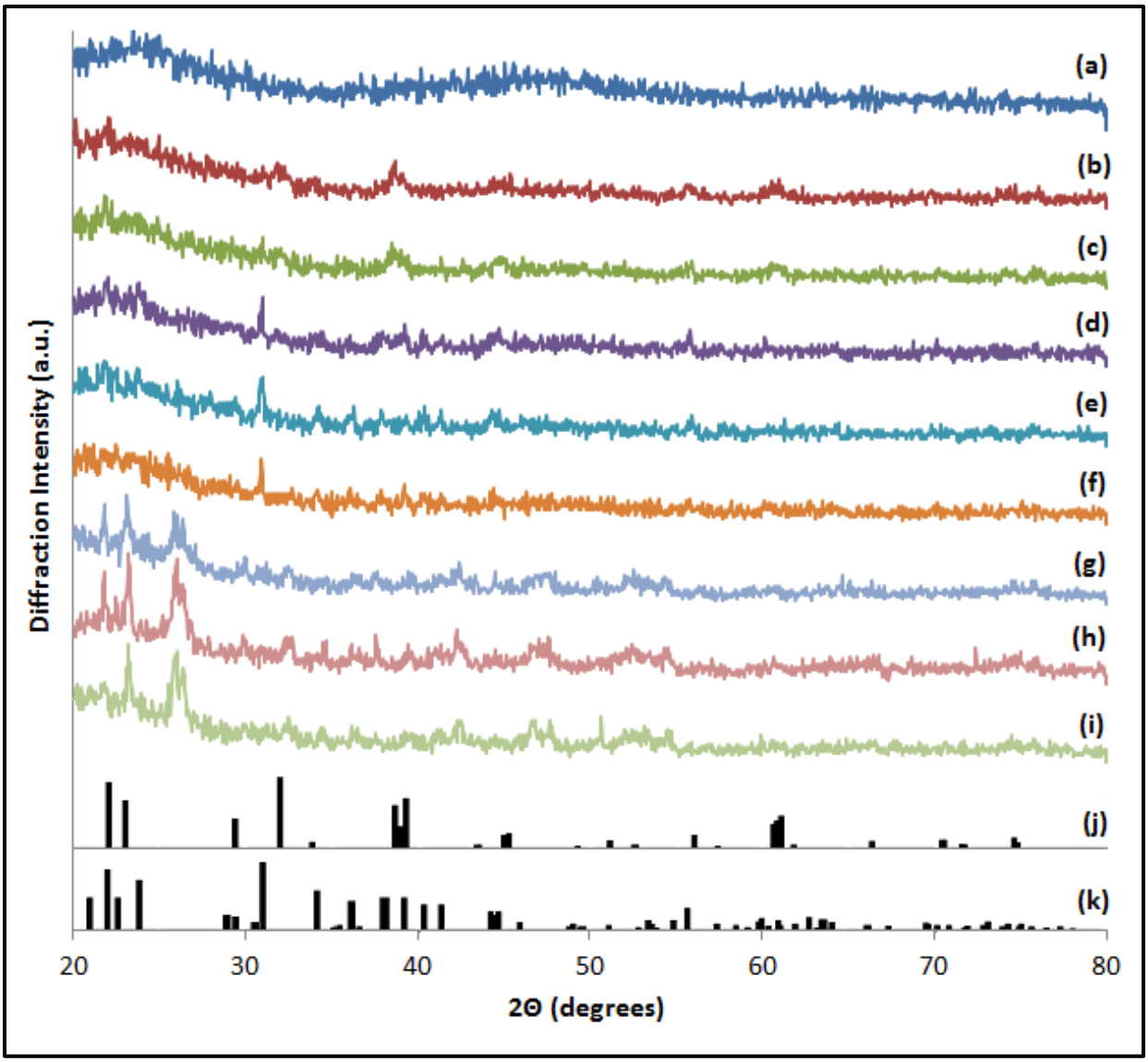

Figure 26. XRD Results for the 15% NaF sample: (a) raw glass, samples heat treated to (b) 290, (c) 295, (d) 300, (e) 305, (f) 310, (g) 315, (h) 320, and (h) 330 °C, (j) the pattern for hexagonal phase $BaCl_2$ (PDF 45-1313), and (k) the pattern for orthorhombic phase $BaCl_2$ (PDF 24-0094).

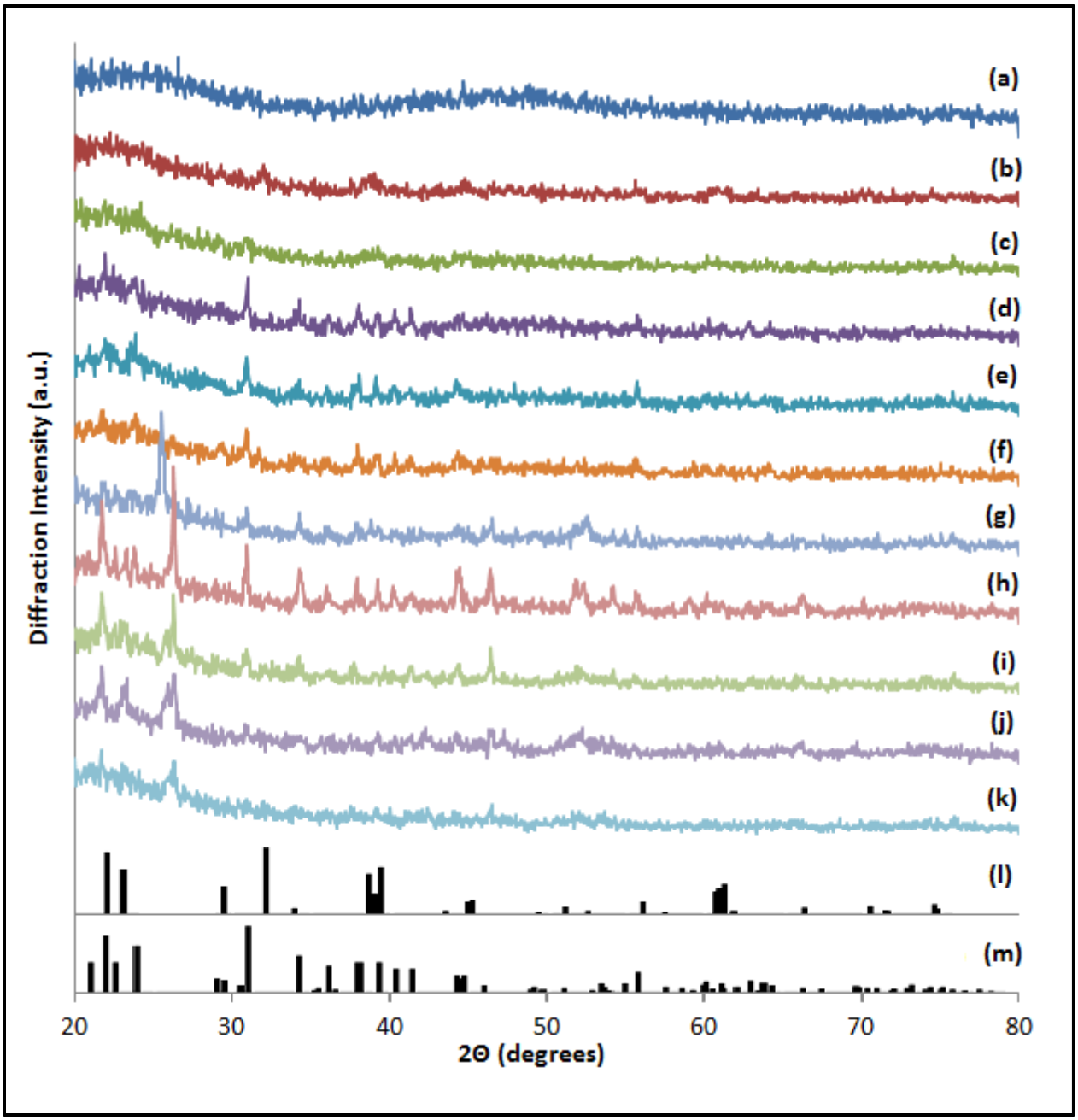

Figure 27. XRD Results for the 20% NaF sample: (a) raw glass, samples heat treated to (b) 280, (c) 285, (d) 290, (e) 295, (f) 300, (g) 305, (h) 310, (i) 315, (j) 330, and (k) 340 °C, (l) the pattern for hexagonal phase $BaCl_2$ (PDF 45-1313), and (m) the pattern for orthorhombic phase $BaCl_2$ (PDF 24-0094).

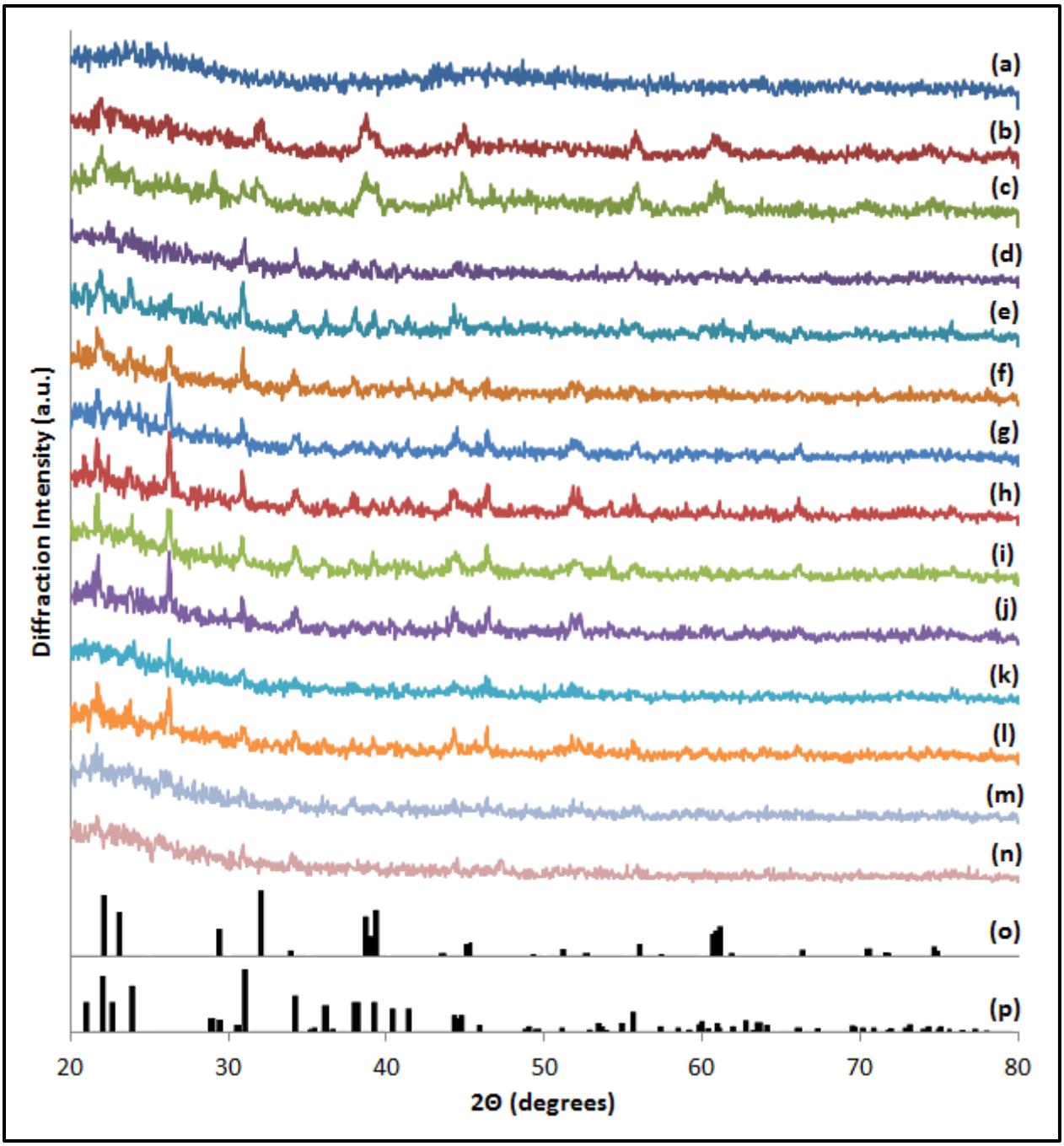

Figure 28. XRD Results for the 25% NaF sample: (a) raw glass, samples heat treated to (b) 270, (c) 275, (d) 280, (e) 285, (f) 290 (g) 295, (h) 300, (i) 305, (j) 310, (k) 315, (l) 320, (m) 330, and (n) 340 °C, (o) the pattern for hexagonal phase $BaCl_2$ (PDF 45-1313), and (p) the pattern for orthorhombic phase $BaCl_2$ (PDF 24-0094).

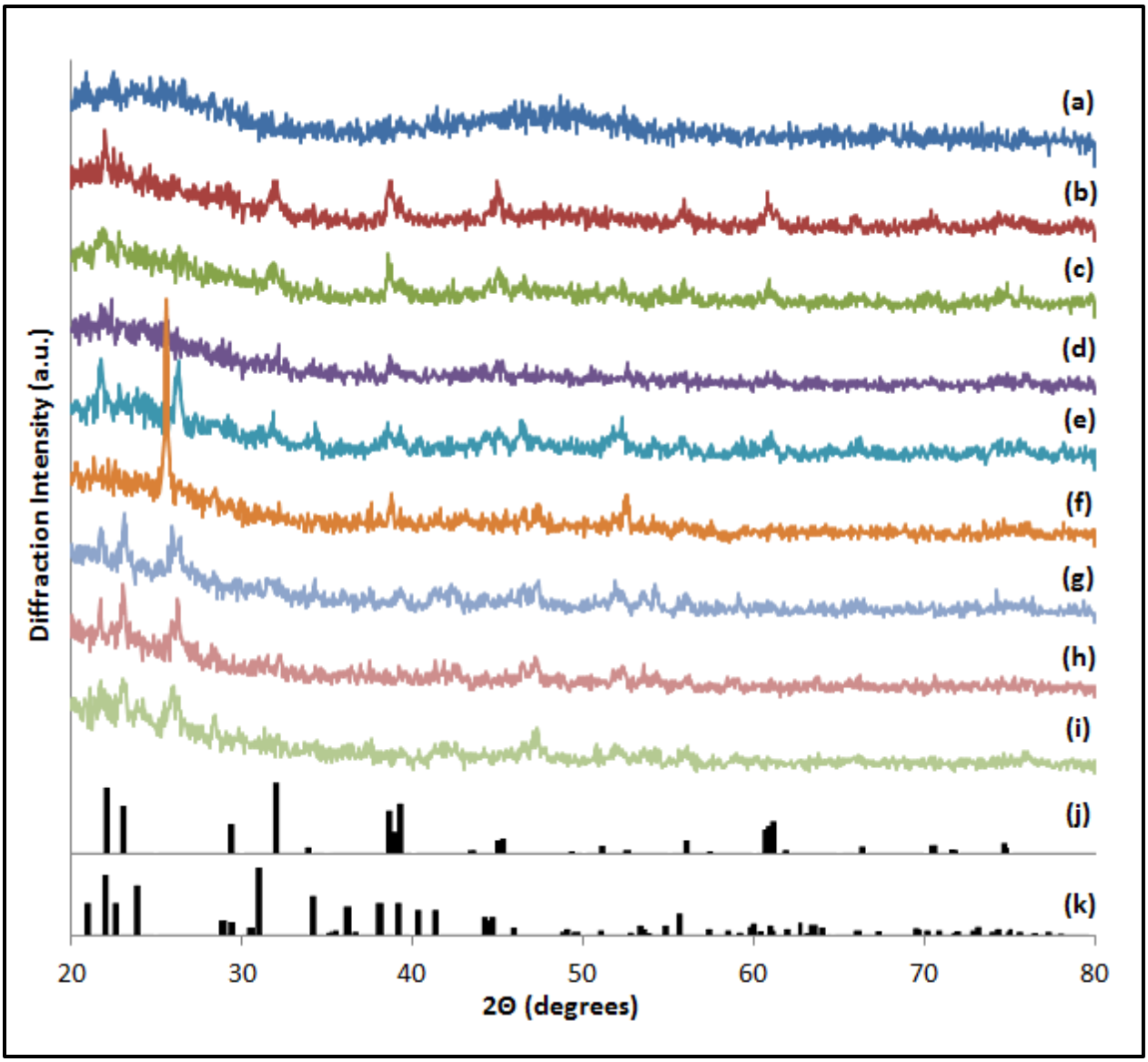

Figure 29. XRD Results for the 30% NaF sample: (a) raw glass, samples heat treated to (b) 270, (c) 290, (d) 295, (e) 300, (f) 305 (g) 310, (h) 330, and (i) 340 °C, (j) the pattern for hexagonal phase $BaCl_2$ (PDF 45-1313), and (k) the pattern for orthorhombic phase $BaCl_2$ (PDF 24-0094).

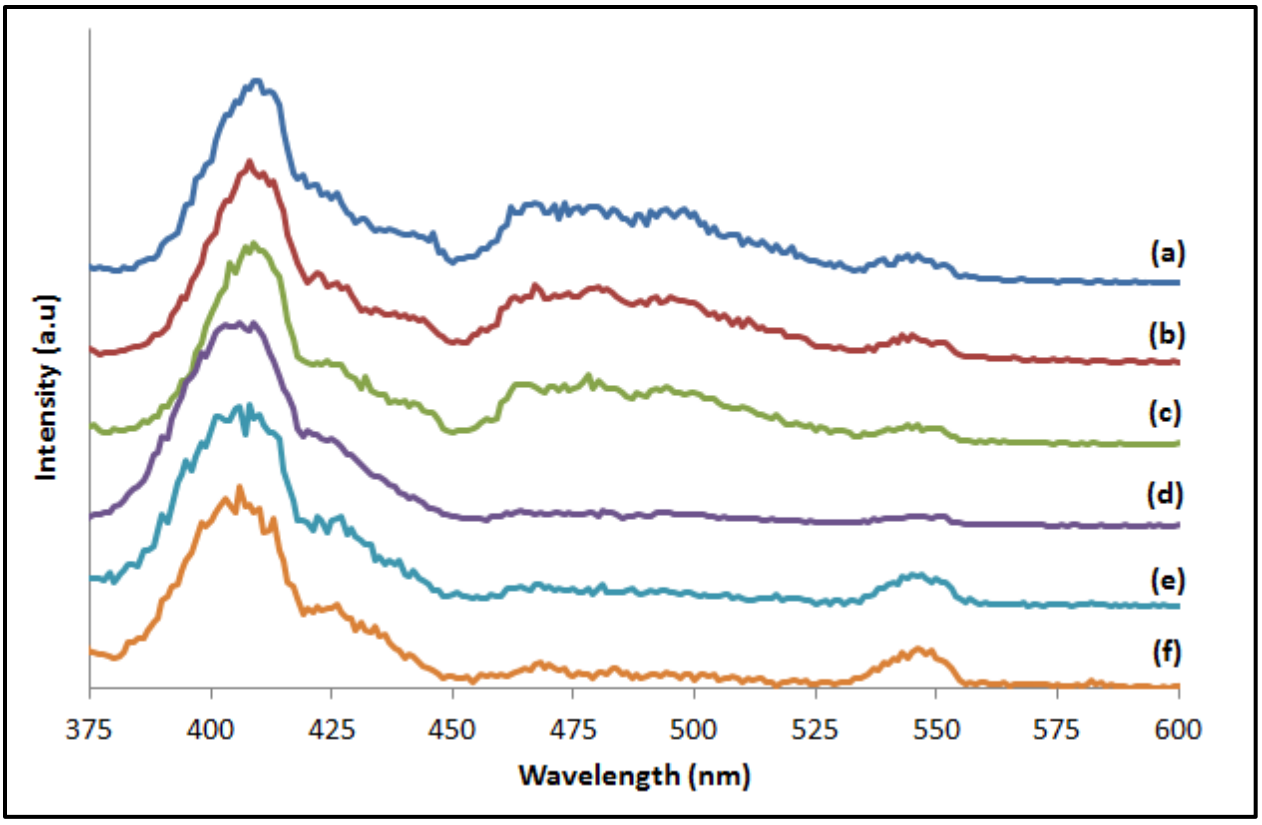

Figure 30. Emission spectra for the 10% NaF sample after heat treatments to the following temperatures: (a) 300, (b) 305, (c) 310, (d) 315, (e) 320, and (f) 330 °C. The excitation wavelength was 360 nm.

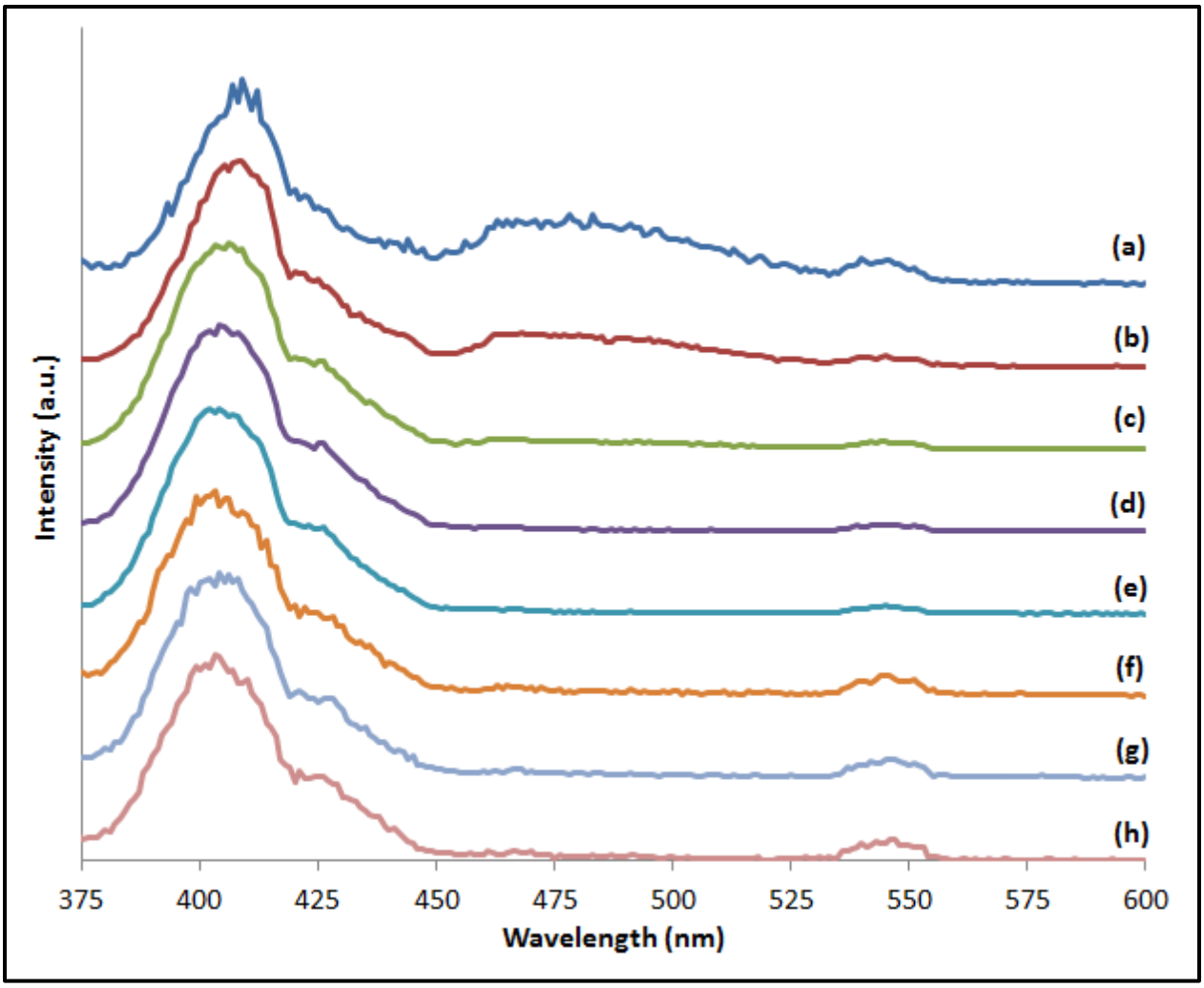

Figure 31. Emission spectra for the 15% NaF sample after heat treatments to the following temperatures: (a) 290, (b) 295, (c) 300, (d) 305, (e) 310, (f) 315, (g) 320, and (h) 330 °C. The excitation wavelength was 360 nm.

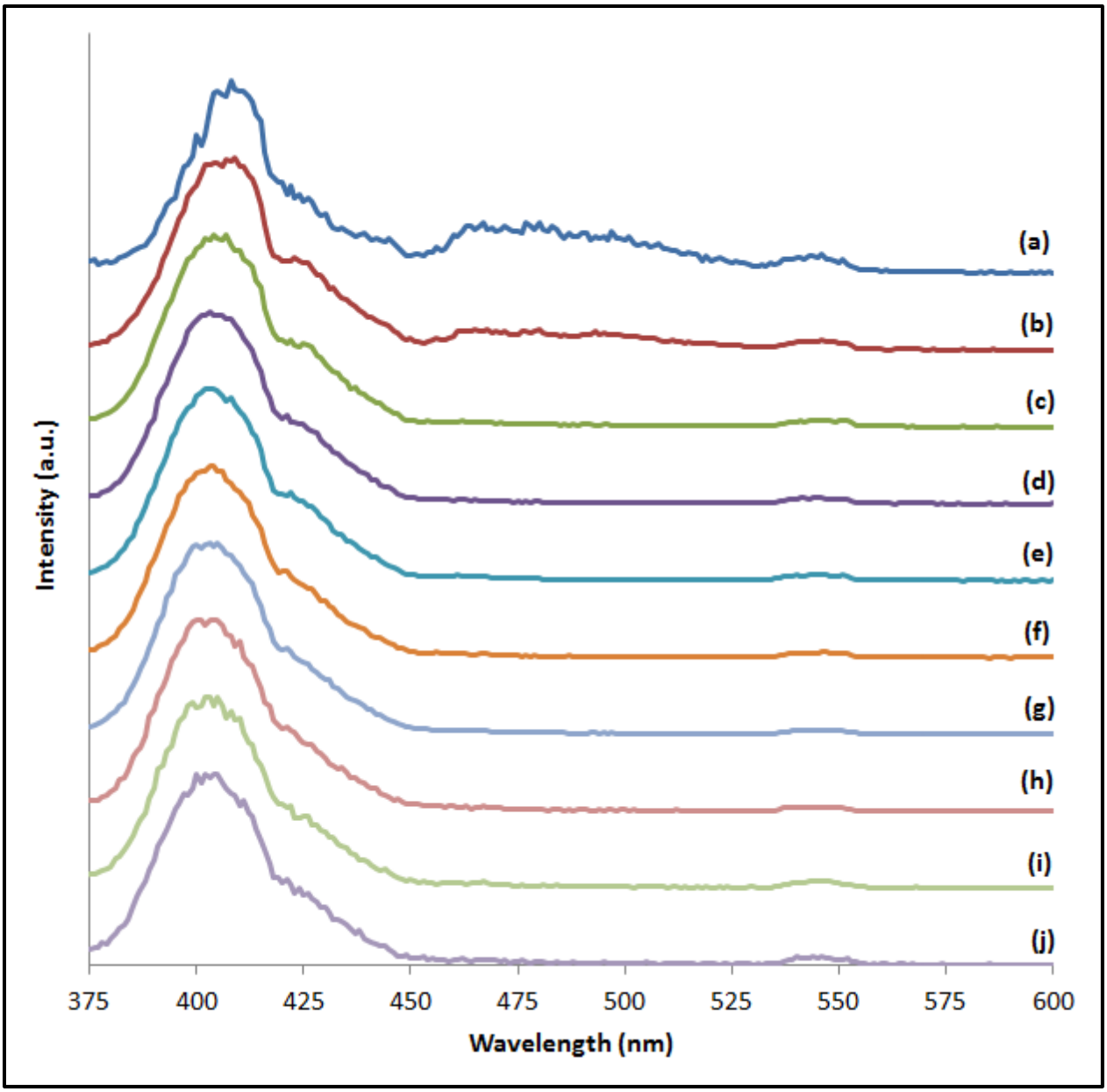

Figure 32. Emission spectra for the 20% NaF sample after heat treatments to the following temperatures: (a) 280, (b) 285, (c) 290, (d) 295, (e) 300, (f) 305, (g) 310, (h) 315, (i) 330, and (j) 340 °C. The excitation wavelength was 360 nm.

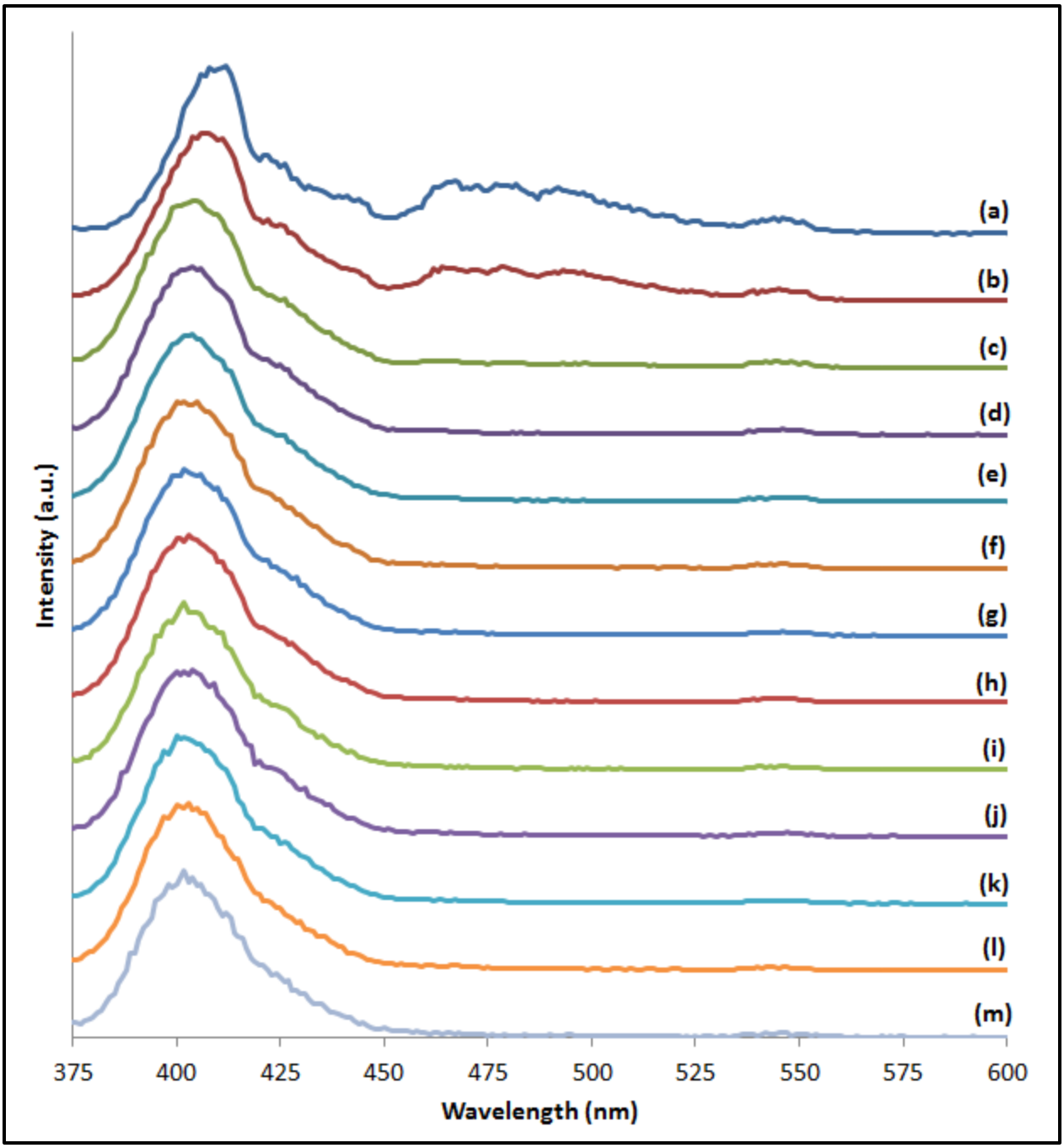

Figure 33. Emission spectra for the 25% NaF sample after heat treatments to the following temperatures: (a) 270, (b) 275, (c) 280, (d) 285, (e) 290 (f) 295, (g) 300, (h) 305, (i) 310, (j) 315, (k) 320, (l) 330, and (m) 340 °C. The excitation wavelength was 360 nm.

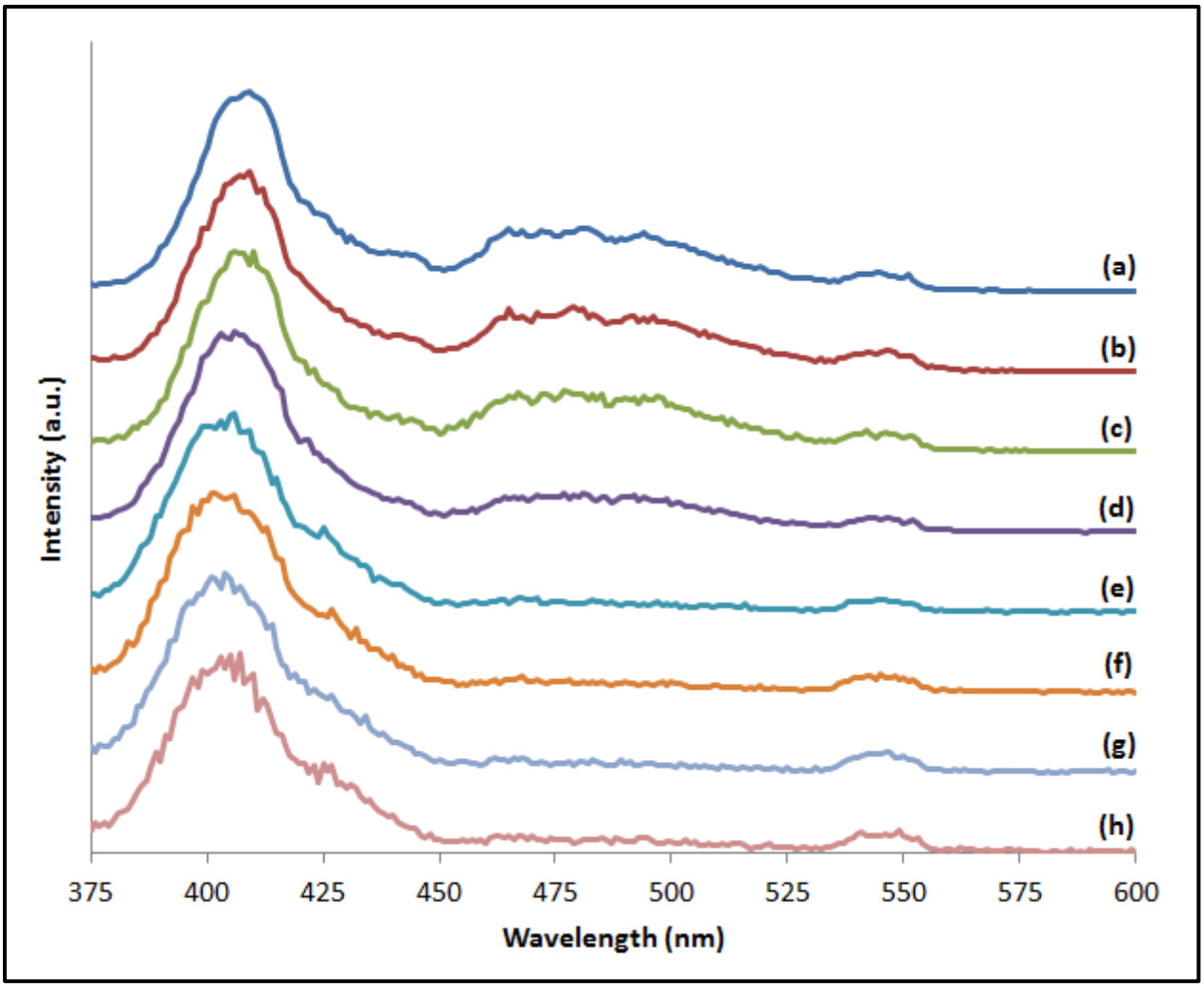

Figure 34. Emission spectra for the 30% NaF sample after heat treatments to the following temperatures: (a) 270, (b) 290, (c) 295, (d) 300, (e) 305 (f) 310, (g) 330, and (h) 340 °C. The excitation wavelength was 360 nm.

Table 5. Phase transformation temperatures from hexagonal to orthorhombic for the $BaCl_2:Eu^{2+}$ crystals estimated from the emission spectra of the heat treated samples.

NaF (%)	10	15	20	25	30
$T_{o\text{ - ortho}}$ (°C)	315	300	290	280	305

Photostimulated Emission Measurements

PSL study of all heat treated samples using an x-ray tube operating at 45 kVp

A representative PSL curve from this study is shown in Figure 35. The emission diminishes with time and can be approximated with an exponential decay curve or the summation of multiple exponential decay curves. Due to their exponential nature, direct comparison of the PSL curves is difficult. In this study, for easier comparison of the PSL output of the samples, the total signal for a finite amount of time was calculated from the data collected for each sample:

$$\text{PSL Area}_{\text{finite}} = \sum_{i=1}^{n} I(t_i)\Delta t_i \quad (1)$$

where

PSL $\text{Area}_{\text{finite}}$ = the area under the PSL decay curve integrated for finite period of time

$I(t_i)$ = the intensity of the PSL signal at a time t_i

Δt_i = sampling interval

n = the number of data points used

The integrated PSL signals based upon this method are shown in Figure 36; the data represent the average area calculated from two separate PSL measurements. For this metric, the 15% NaF sample is the best performing, but has a small process window for heat treatments (300 – 310 °C). The 20% and 25% NaF samples have slightly lower performance, but larger process windows (295 – 310 °C and 285 – 310 °C,

respectively). Larger process windows would be advantageous in a large-scale manufacturing environment.

For all compositions, there is a heat treatment temperature at which there is a steep increase in signal that corresponds to the phase transformation from hexagonal to orthorhombic $BaCl_2$ (see Tables 4 and 5). After this initial gain, some of the compositions have further improvement in performance with increasing temperature, which may be the result of increased crystallite size [12]. The two compositions with the least NaF, 10% and 15%, have a steep reduction in performance at higher heat treatment temperatures, while for the other samples, the drop-off is not so pronounced.

The 25% NaF sample has a data point at 315 °C that appears out-of-place in comparison to the surrounding data points. However, an additional measurement for this heat treated sample yielded PSL results that matched those from the original measurements. Furthermore, an additional portion of the 25% NaF sample was also heat treated to 315 °C using the same parameters as the first heat treated sample; measurement of its PSL light output also yielded similar results, indicating the anomaly in performance is real. The results of all four measurements can be found in the Appendix (see Figure A5).

Comparison against commercial imaging plates at energies typical for intraoral dental radiography

The PSL light output of select samples are compared against commercial storage phosphors, produced by Fuji Photo Film Company and Dentoptix, at 70 kVp energies that are typical for intraoral dental radiography in Figure 37. The samples produced in this study had significantly lower performance than the commercial plates. The 20% NaF sample compared most favorably, having approximately 10% and 30% of the total light output of Fuji and Dentoptix plates respectively.

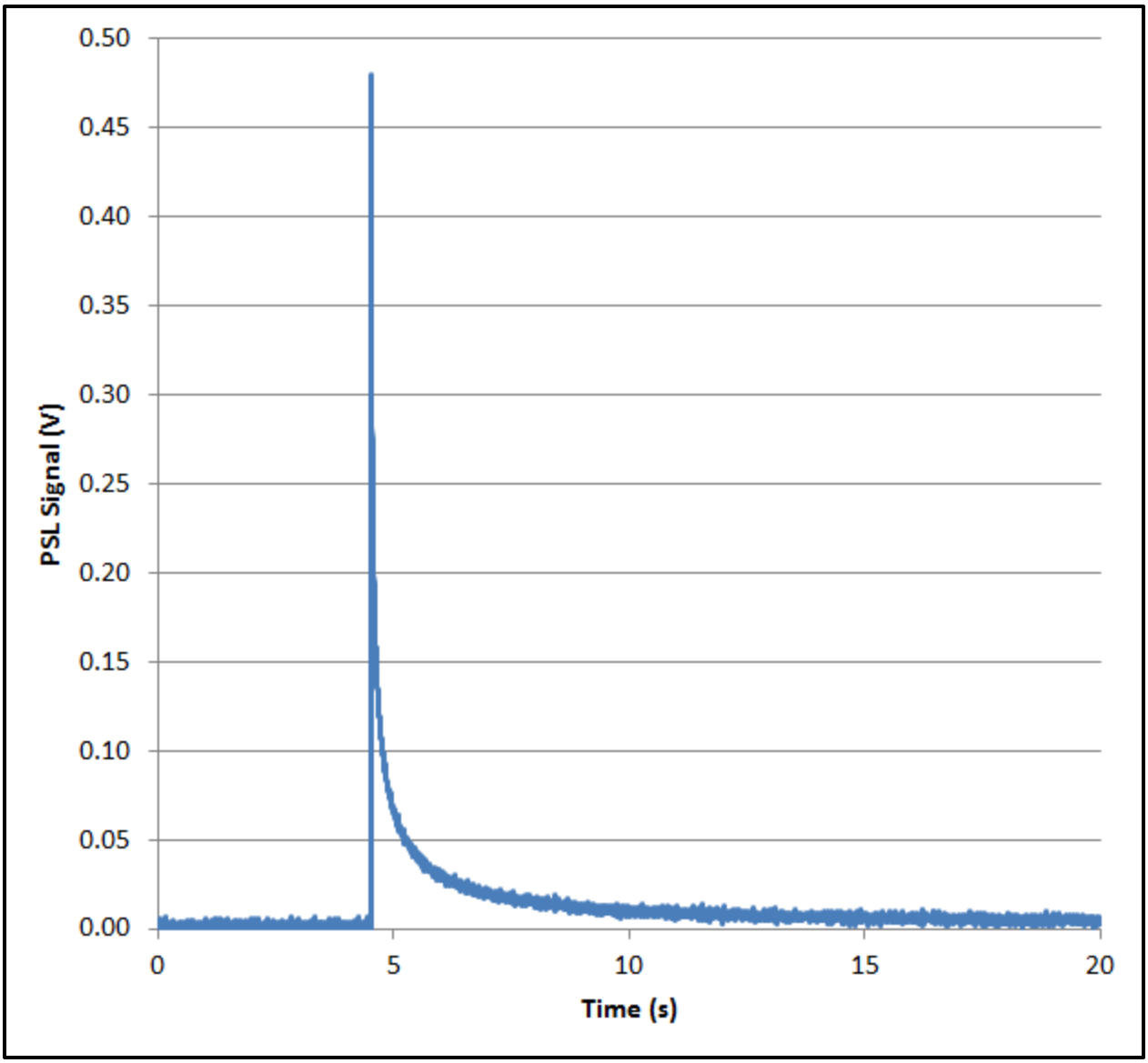

Figure 35. Representative PSL curve from the 15% NaF sample, heat treated to 310 °C.

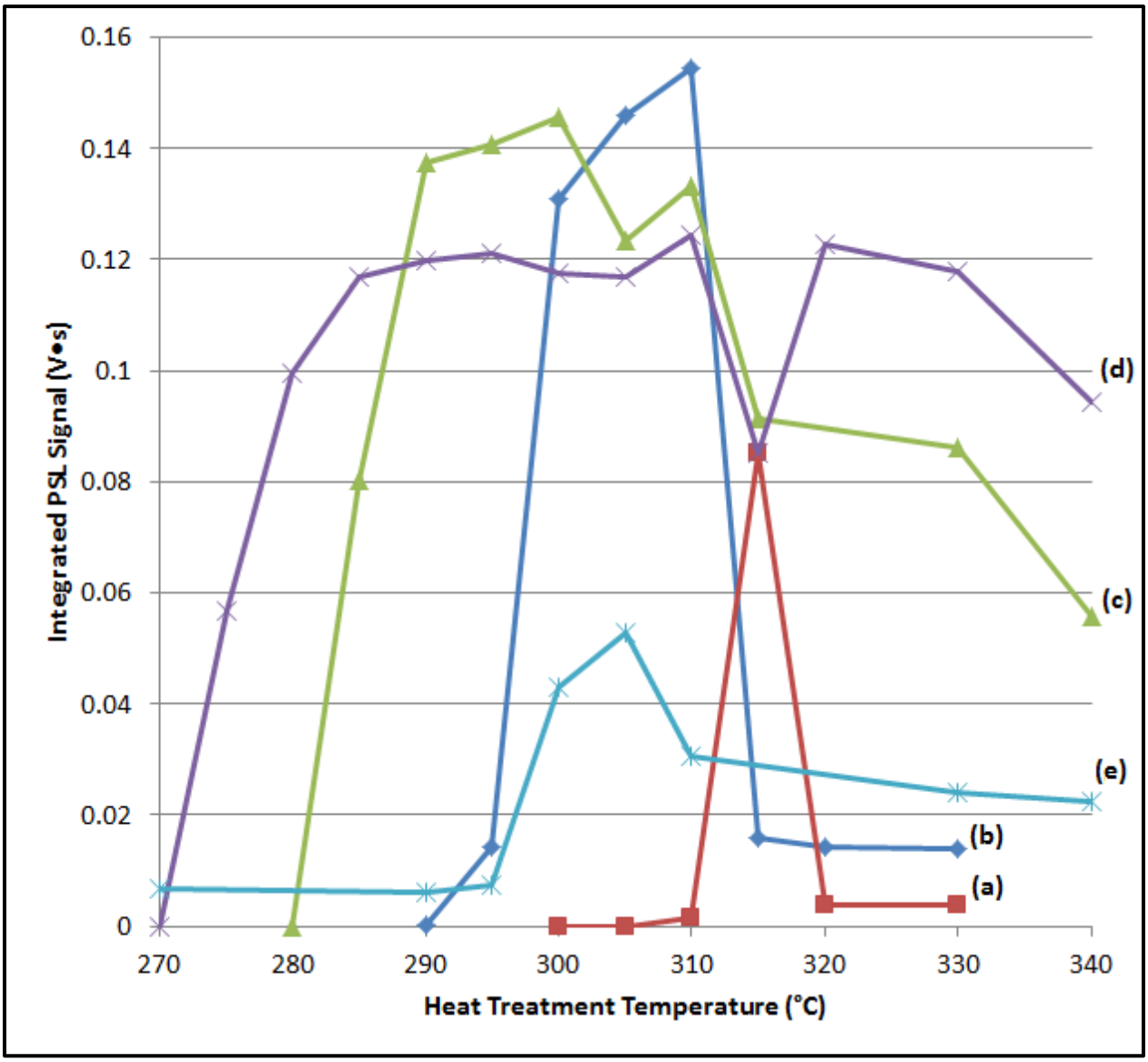

Figure 36. Integrated PSL signal for each heat treated sample based upon 10 seconds of data for the: (a) 10% NaF sample, (b) 15% NaF sample, (c) 20% NaF sample, (d) 25% NaF sample, and (e) 30% NaF sample. Each point represents the average area from two PSL measurements.

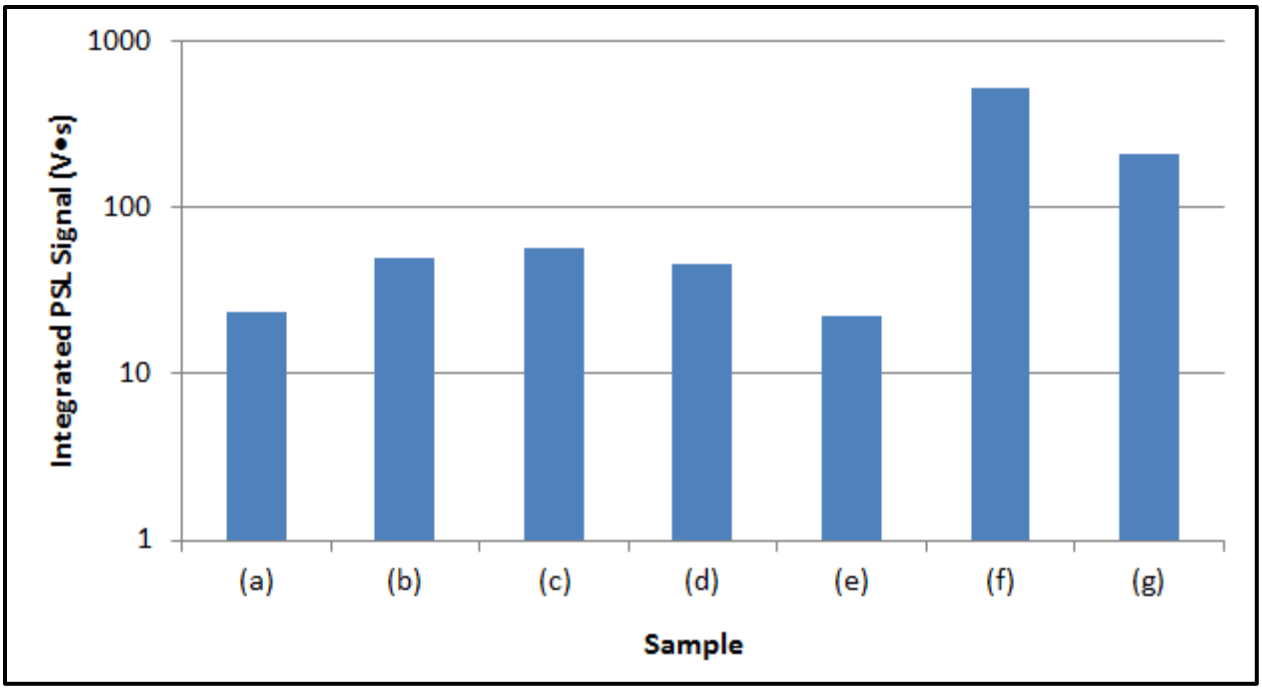

Figure 37. Comparison of PSL light output of select samples against commercial storage phosphors: (a) 10% NaF sample, heat treated to 315 °C, (b) 15% NaF sample, heat treated to 310 °C, (c) 20% NaF sample, heat treated to 300 °C, (d) 25% NaF sample, heat treated to 290 °C, and (e) 30% NaF sample, heat treated to 305 °C, (f) a Fuji Photo commercial plate, and (g) a Dentoptix commercial plate. The data are plotted on a $\log_{10}$ scale.

Discussion

The percentage of NaF content used in glass synthesis had a marked effect on sample properties. Increasing NaF content led to the following changes:

- more stable molten glasses with less evaporative loss during synthesis
- more transparent glasses prior to heat treatments
- lower glass transition temperatures
- lower crystallization and phase transformation temperatures, excluding the 30% NaF sample
- loss of transparency at lower heat treatment temperatures

The effect of NaF on PSL light output, however, is not straightforward. For the results at 45 kVp exposures with the compositions containing 15%, 20% NaF, 25% NaF, and 30% NaF, it would appear that increasing NaF decreases performance. This result could be expected based upon the percentage of Ba^{2+}, Cl^{-}, and Eu^{2+} present in the starting materials, which increases with decreased NaF content and forms the PSL luminescent center $BaCl_2$:Eu^{2+} upon crystallization and subsequent transformation to the orthorhombic phase. Based upon this line of reasoning, the 10% NaF sample, with the most Ba^{2+}, Cl^{-}, and Eu^{2+} present in the starting materials, should have the best performance, but does not.

The 10% NaF sample is the least transparent sample before heat treatment, but this result does not explain its lower performance. The heat treat samples were stimulated for a sufficient amount of time so that reduced transmission at the stimulating wavelength would not affect the overall light output collected. In addition, while the transmission for the 10% NaF sample at the PSL emission wavelength is low, it is roughly equivalent to the 15% NaF sample, which is the highest performing sample.

A possible explanation for the trends in PSL light output for the heat treated samples is revealed when, for each sample composition, the PSL results are overlaid with the DSC curves. These overlays are shown in Figures 38 through 42. In Figure 38, the 10% NaF sample produces considerable PSL signal when heat treated to 315 °C, but almost no signal when heat treated to 320 °C. The rapid decline in PSL output for the 10% NaF sample coincides with a large exothermic peak in the DSC curve for the glass, which is associated with partial crystallization of the glass matrix. A similar drop-off in performance can be seen in the 15% NaF sample and, although the reduction is not as drastic, in the 20% and 30% NaF samples. Alvarez showed that for FCZ glass ceramics, partial crystallization of the glass matrix may result in crystalline phases that contain Ba^{2+} and Cl^{-}, which consume existing $BaCl_2$ during their formation [74]. Consumption of $BaCl_2$ in this manner would decrease the number of luminescent centers in the FCZ glass ceramics and therefore reduce PSL light output. In addition, crystallization of the matrix would lessen transparency, also leading to a decrease in light output. It is hypothesized that the light output of the 10% NaF sample is relatively low because the hexagonal-to-orthorhombic phase transformation of $BaCl_2$ is not allowed to reach completion before the $BaCl_2$ crystals are consumed by the phase that forms with partial crystallization of the glass matrix.

The 25% NaF sample differs from the other samples in that its PSL performance remains relatively stable across higher heat treatment temperatures where additional crystallizations occur, according to the DSC and XRD data. It is possible that these new phases do not consume Ba^{2+} or Cl^{-} in their formation, so PSL performance is not affected. An alternative explanation is that at least one of the subsequent phases has storage phosphor properties of its own; this hypothesis is supported by the drop in performance at a heat treatment temperature of 315 °C, followed by the subsequent increase in performance at 320 °C.

The PSL light output of the heat treated samples was significantly less than that of the two commercial storage phosphors to which they were compared. Clearly for intraoral dental radiography applications, where dose is critical, significant improvements in performance must be obtained before glass-ceramic storage phosphors of the type produced for this study can be competitive with existing commercial technologies. The samples' PSL light output, however, may be sufficient for nondestructive testing applications, where dose is not a primary consideration. The small area of the heat treated sample (~5mm × 5mm) prevents basic imaging tests to determine spatial resolution and contrast detection; larger area glass samples must be made and heat treated for this type of testing to proceed.

Conclusions

This study shows that the percentage of NaF used in preparation of FCZ glass ceramics has a marked effect on the materials' properties. The stability of the molten glass is improved with increasing NaF content, leading to reduced mass loss through evaporation during glass synthesis. The glass transition temperature decreases with increasing NaF content. Up to 25% NaF, crystallization of hexagonal $BaCl_2$ and its subsequent transformation to the orthorhombic phase occurs at lower temperatures with increased NaF content. As-made glasses with increased NaF content were slightly more transparent; however, this trend reversed after the heat treatment process, with higher NaF content glass ceramics becoming more turbid at lower heat treatment temperatures.

There is a complex relationship between PSL light output and NaF content in the samples. Those samples with intermediate amounts of NaF (15, 20, and 25%) had the greatest light output. It is hypothesized that in the 10% NaF sample, a phase that forms with partial crystallization of the glass matrix consumes the $BaCl_2$ crystals before they can fully transform into the orthorhombic phase, thus greatly reducing its PSL light

output. This phenomenon is posited to also affect the performance of the other samples, but to a lesser degree.

The PSL light output of the glass-ceramic samples was considerably less than that of commercial phosphors when tested at energies typical for intraoral dental radiography. For this and other applications where dose is critical, significant improvements in performance must be obtained before glass-ceramic storage phosphors of the type produced for this study can be competitive with existing commercial technologies. The reduced PSL light output of the samples, compared to what is commercially available, may still be suitable for nondestructive testing, where dose is not a primary concern. Larger area samples will have to be produced before additional testing of imaging performance can proceed.

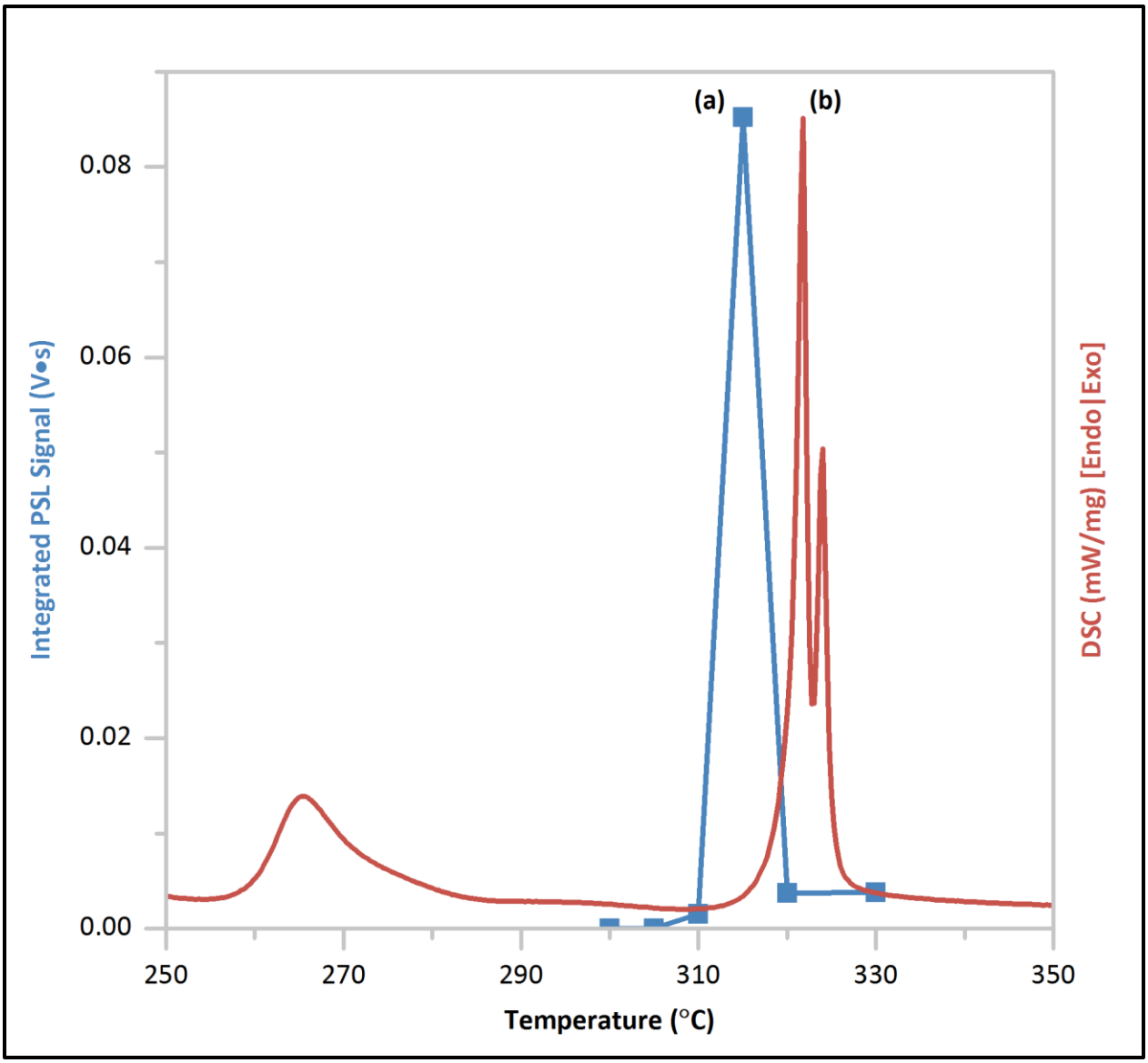

Figure 38. Overlay of (a) the integrated PSL signal as a function of heat treatment temperature and (b) the DSC curve for the 10% NaF sample.

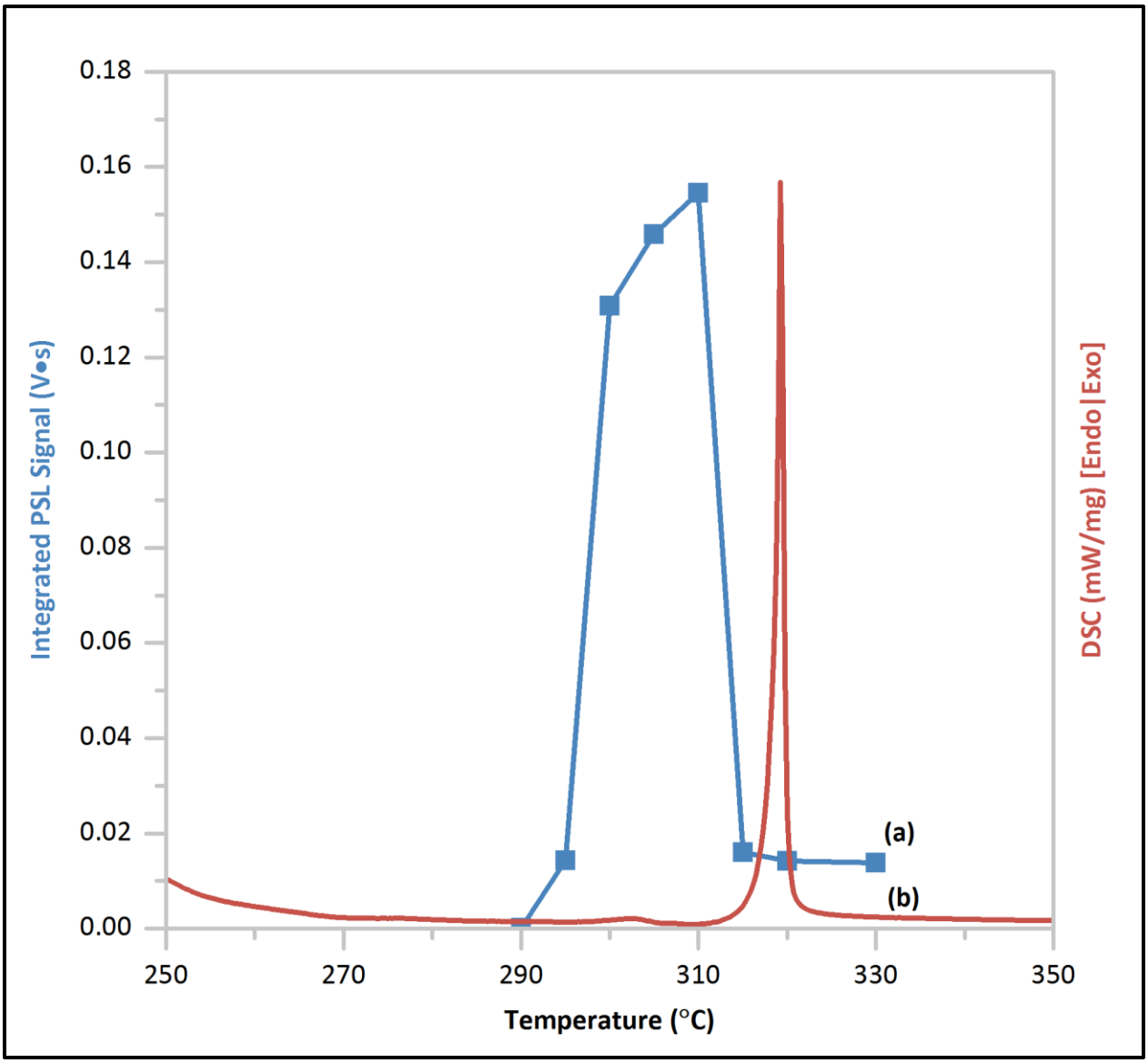

Figure 39. Overlay of (a) the integrated PSL signal as a function of heat treatment temperature and (b) the DSC curve for the 15% NaF sample.

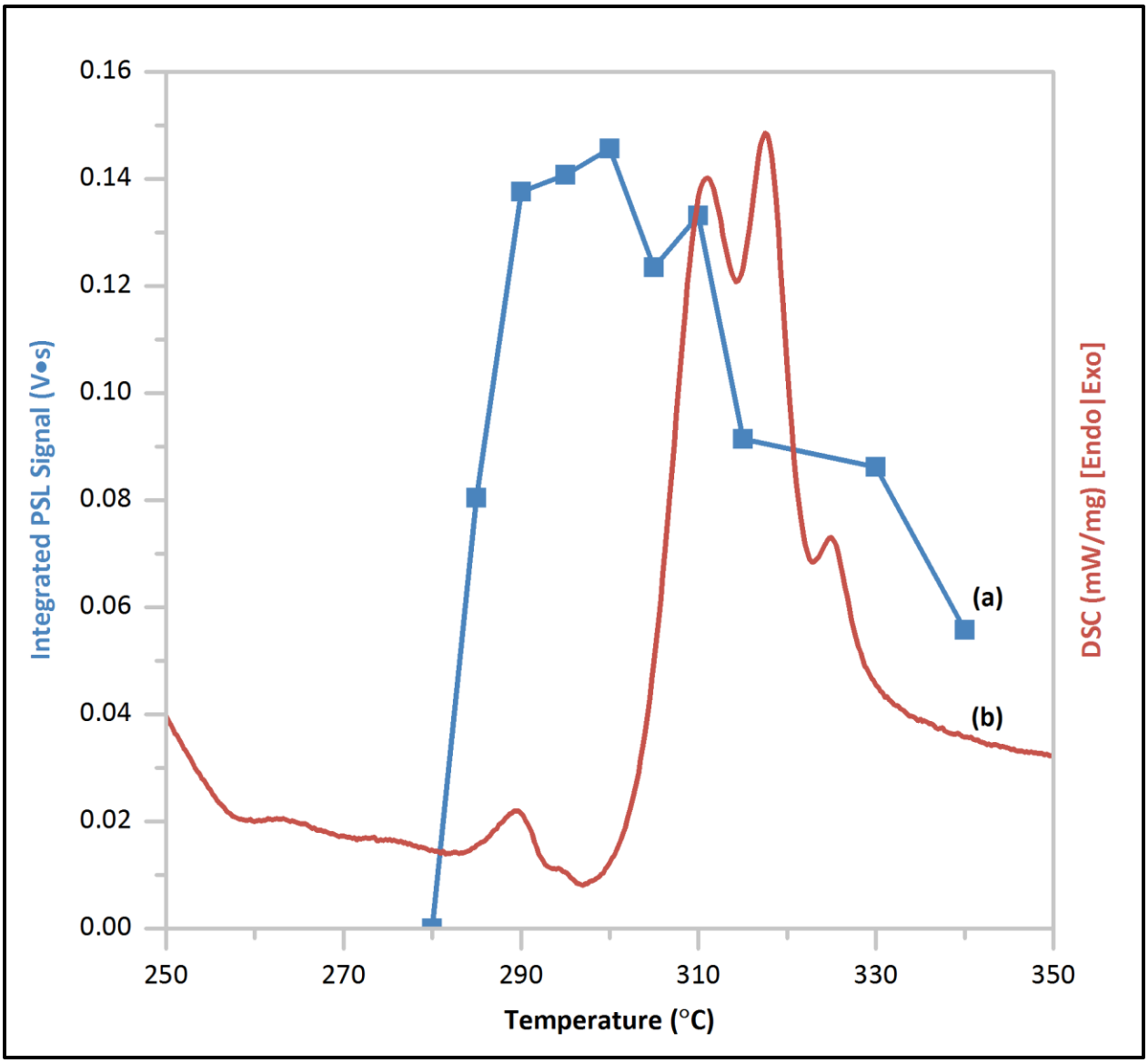

Figure 40. Overlay of (a) the integrated PSL signal as a function of heat treatment temperature and (b) the DSC curve for the 20% NaF sample.

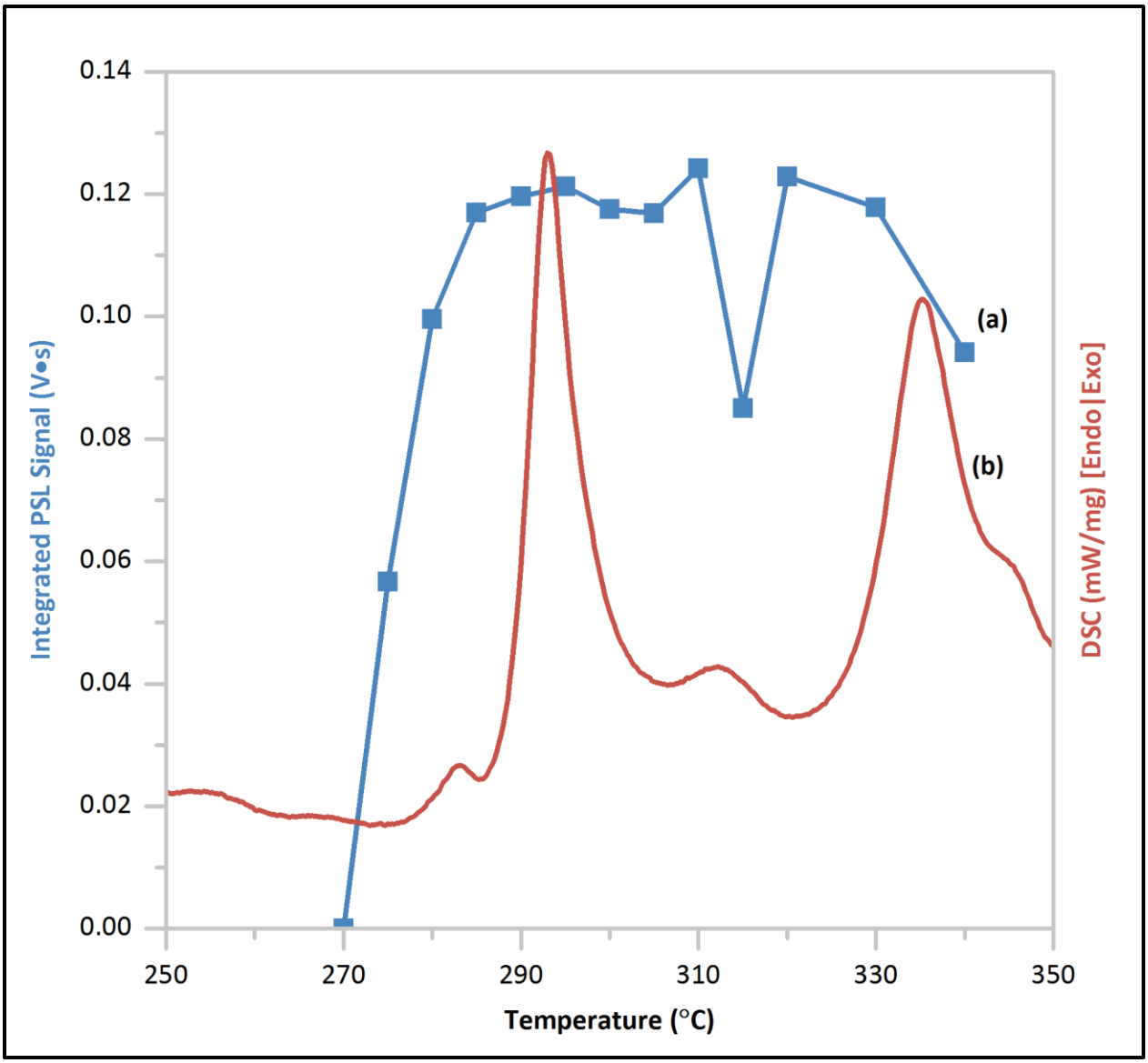

Figure 41. Overlay of (a) the integrated PSL signal as a function of heat treatment temperature and (b) the DSC curve for the 25% NaF sample.

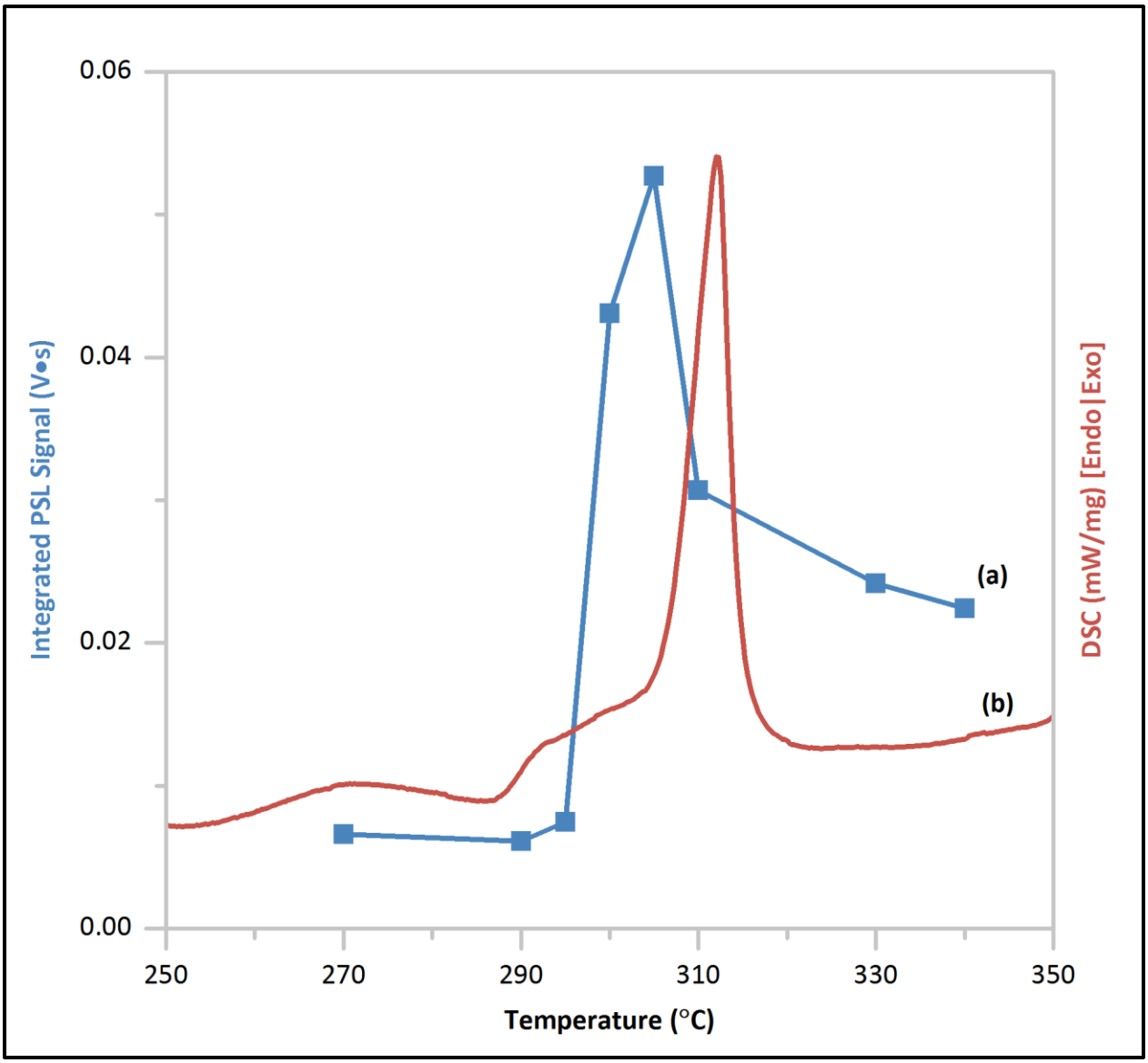

Figure 42. Overlay of (a) the integrated PSL signal as a function of heat treatment temperature and (b) the DSC curve for the 30% NaF sample.

CHAPTER IV:
EVALUATION OF A FLUOROCHLOROZIRCONATE GLASS-CERAMIC STORAGE PHOSPHOR PLATE FOR GAMMA-RAY COMPUTED RADIOGRAPHY

A version of this chapter was originally published by Russell L. Leonard, Sharon K. Gray, Carlos J. Alvarez, Alex K. Moses, Lloyd F. Arrowood, Anthony R. Lubinsky, Amanda K. Petford-Long, and Jacqueline A. Johnson:

Leonard, R.L., et al., *Evaluation of a Fluorochlorozirconate Glass-Ceramic Storage Phosphor Plate for Gamma-Ray Computed Radiography.* Journal of the American Ceramic Society, 2015. DOI: 10.1111/jace.13664

Russell L. Leonard was responsible for all writing and research activities in the original article except as noted: Gray provided the XRD data. Alvarez and Petford-Long provided the results and discussion pertaining to the SEM and TEM measurements. Moses and Arrowood were responsible for the exposure of the samples at MeV energies. Lubinsky assisted with the photostimulated luminescence measurements and imaging and the evaluation of those results. Johnson provided guidance for the overall project. This chapter differs from the original publication in that the potential for portal imaging applications is discussed in more detail and some ancillary figures are included in the Appendix.

Abstract

A fluorochlorozirconate (FCZ) glass ceramic containing orthorhombic barium chloride crystals doped with divalent europium was evaluated for use as a storage phosphor in gamma-ray imaging. X-ray diffraction and phosphorimetry of the glass-ceramic sample showed the presence of a significant amount of orthorhombic barium chloride crystals in the glass matrix. Transmission electron microscopy and scanning electron microscopy were used to identify crystal size, structure, and morphology. The size of the orthorhombic barium chloride crystals in the FCZ glass matrix was very large, ~0.5-0.7 μm, which can limit image resolution. The FCZ glass-ceramic sample was exposed to 1 MeV gamma rays to determine its photostimulated emission characteristics at high energies, which were found to be suitable for imaging applications. Test images were made at 2 MeV energies using gap and step wedge phantoms. Gaps as small as 101.6

μm in a 440 stainless steel phantom were imaged using the sample imaging plate. Analysis of an image created using a depleted uranium step wedge phantom showed that emission is proportional to incident energy at the sample and to the estimated absorbed dose. The results indicate that the sample imaging plate has potential for gamma-ray computed radiography and dosimetry applications. The ability of these materials to generate an image at MeV energies with complementary dosimetry information indicates potential for use in portal imaging applications.

Introduction

Computed radiography (CR) is a valuable imaging technique in which reusable storage phosphor plates capture an image of an object probed with ionizing radiation, typically x-rays [36]. Electron-hole pairs are thereby created within the storage phosphor plate in proportion to the incident radiation; hence the attenuation of the beam by the subject creates an image, stored within the phosphor plate. The image can be subsequently read-out by stimulating the electron-hole pairs within the plate using a light source, such as a laser, causing recombination and light emission that can be collected and measured to create a digital image. Any latent image remaining within the plate can be erased through prolonged exposure to a light source, allowing the plate to be reused. CR is commonly used in medical imaging, where it is an attractive alternative to traditional film/screen and digital (DR) x-ray radiography [32]. CR has advantages over traditional film in that it has greater dynamic range, does not require chemical development, and creates a digital picture as part of the read-out process. CR systems are generally less costly to implement and allow for easier manipulation and placement of the imaging sensor (plate) when compared to DR systems.

CR has found use in portal imaging applications, where a high energy radiotherapy beam is used to acquire an image [47, 48, 75]. The image is primarily used for geometric verification, ensuring that treatment occurs in the correct location. Portal imaging may also be used provide dosimetric verification. Near-diagnostic images should be possible, but the spatial resolution of the image produced by commercial

portal imaging systems is poor [48, 49]. For example, modern electronic portal imaging devices (EPID) have values in the range of 0.3-0.4 lp/mm [50]. Improvements in spatial resolution could potentially reduce positioning errors and decrease treatment margins around the clinical target volume.

CR is also used in nondestructive testing to check the internal structure of an object such as a pipe or a welded component [33-35]. Unlike with medical imaging, dose is generally not a concern, so longer exposures and higher energy photons, including those in the MeV portion of the electromagnetic spectrum, may be used to probe the materials. Higher energies allow for the imaging of thicker, higher density materials. Radioisotopes such as ^{192}Ir, ^{75}Se, and ^{60}Co and linear accelerators (linacs) can serve as radiation sources [33]. The type of photon interaction shifts from the photoelectric effect (energies less than 50 keV) to Compton scattering (100 keV to 10 MeV) as the energy of the radiation source increases. Image creation remains the same, however: exposure, electron-hole pair creation, stimulation, recombination and read-out, followed by erasure. As incident energy increases, the Compton scattering angle decreases, which should reduce spreading and increase resolution, especially in relatively thick imaging plates.

Traditional commercial storage phosphors are finely powdered crystals held within an organic binder [76]. Scattering of the stimulating light at crystal boundaries is an inherent problem leading to reduced resolution. Thinning of the phosphor plate results in improved resolution, but at the same time, a decrease in detective quantum efficiency, thus requiring increased dose.

Glass ceramics represent a new class of storage phosphor materials. Fluorochlorozirconate (FCZ) glass ceramics containing orthorhombic $BaCl_2$:Eu^{2+} nanocrystals have shown the potential for greatly improved resolution when compared to traditional storage phosphor materials [18, 19]. With nanocrystals much smaller in diameter than the wavelength of the stimulating light, scattering is greatly reduced, leading to a large improvement in resolution.

The purpose of this work is to evaluate an FCZ glass ceramic containing orthorhombic $BaCl_2$:Eu^{2+} crystals for use as a storage phosphor in gamma-ray computed radiography. An FCZ glass sample doped with Eu^{2+} was produced, then subsequently heat-treated to precipitate orthorhombic $BaCl_2$ crystals within the matrix to create a glass ceramic capable of performing as a storage phosphor. The approximate temperature of the $BaCl_2$ hexagonal-to-orthorhombic phase transformation was estimated using differential scanning calorimetry (DSC) [66, 77]. X-ray diffractometry (XRD) and phosphorimetry measurements were used to identify the crystalline phases present in the glass ceramic [78]. Transmission electron microscopy (TEM) and scanning electron microscopy (SEM) were used to identify crystal size, structure, and morphology [23, 68]. The sample was exposed to 1 MeV gamma rays to determine its photostimulated emission characteristics at high energies. Test images were made using two types of phantoms at 2 MeV energies. To the author's knowledge, this is the first time testing of this type of plate with high-energy sources has been reported.

Experimental Procedure

An FCZ glass sample was prepared with a composition in mole percentage as follows: $47.80ZrF_4$-$19.90BaCl_2$-$3.28LaF_3$-$2.81AlF_3$-$25.0NaF$-$0.47InF_3$-$0.75EuCl_2$. During synthesis, the raw materials were weighed in a glovebox (MBRAUN Labmaster SP) with an argon atmosphere to prevent contamination from oxygen or water vapor (see Figure A1 in the Appendix). The total weight for the sample mixture was 45 grams. Next, the sample mixture was heated within a platinum crucible inside a programmable tube furnace (MTI Corporation OTF-1200X) to a temperature of 800 °C. The furnace was connected to the glovebox though a doorway and also contained an argon atmosphere. At the completion of the heating cycle, the molten glass was poured into a brass mold at a temperature of 200 °C (see Figure A2 in the Appendix). The brass mold was equipped with cartridge heaters and a thermocouple connected to a PID controller that gradually cooled the glass to room temperature over a period of four hours.

A differential scanning calorimetry (Netzsch DSC 200 F3) scan was conducted from 100 °C to 400 °C at a rate of 1 K per minute. A 27.0 mg portion of the sample was used for the scan. The result of this scan was used to estimate the heat treatment conditions used to precipitate orthorhombic phase $BaCl_2$ crystals in the glass matrix, forming a glass ceramic.

A portion of the glass sample of approximate size 6 cm × 6 cm × 0.15 cm was heat treated in air using a custom-built, programmable device (see Figure A3 in the Appendix). The temperature in the sample chamber was PID controlled, using cartridge heaters as the heat source and thermocouples to monitor the temperature. The sample was heated to 300 °C at a rate of 5 K per minute and held at that temperature for 30 minutes, after which it was cooled to room temperature at a rate of 5 K per minute.

X-ray diffraction measurement of the heat-treated sample was performed on a Philips X'Pert MRD X-ray Diffractometer with a Cu anode x-ray source, in the 2θ range from 20° to 80°. The scanning rate step size was 0.02° with a time step of 10 seconds. Prior to measurement, the sample was polished to expose the sample bulk. MDI Jade 9 analytical software was used to identify the crystalline phases.

The emission spectrum was determined using a QM-3-PH phosphorescence / fluorescence spectrofluorometer (Photon Technology International, Inc.) with Czerny-Turner monochromators at the source and detector. The system was equipped with a Type L4633 Xenon Flash Lamp (Hamamatsu Photonics K.K.) and an R1527P Photomultiplier tube (Hamamatsu Photonics K.K.). The computer interface was a PC equipped with FeliX32 software for data analysis. The measurements in this study were made using the following parameters: step size = 1 nm, integration time = 50 µs, averages (number of repeated scans for which results are averaged) = 6, shots (lamp pulses per each individual scan with results averaged) = 50, lamp frequency = 100 Hz.

TEM and SEM were used to identify crystal size, structure, and morphology within the sample. The specimen was sectioned, polished, and mounted onto an SEM stub using

conductive epoxy. The preparation was completed with the use of oil-based lubricants to prevent the dissolution or reaction of the highly hygroscopic $BaCl_2$ crystals with water. The specimen was first analyzed with SEM (Zeiss 1540XB FIB-SEM) at 5 kV in a focused ion beam (FIB). A backscattered electron detector was used to distinguish the crystalline phase from the glass matrix. After imaging with SEM, the sample specimen was coated with gold and capped with a carbon protection layer; the FIB was then used to make a TEM lift-out specimen. After thinning the lamella down to electron transparency, the specimen was characterized using a JEOL 2100F TEM at 200 kV with a double-tilt holder. Dark-field TEM was used to highlight the locations of the crystals within the glass matrix. Selected area electron diffraction (SAED) patterns were taken from the crystal regions within the lamella. The software package, Single Crystal, was used to simulate the corresponding SAED patterns.

Photostimulated emission characteristics were measured using a custom system consisting of a 4” integrating sphere (Labsphere, Inc.), a photosensor module and power supply (Hamamatsu HC124-06 and C7169), a data acquisition card (National instruments NIUSB-6215), and a 532 nm pumped diode Nd/YAG laser operating at 60 mW. To measure the emission, the material was exposed to 1 MeV gamma rays at a distance of 72 inches for 2.5 minutes using a Varian Medical Systems Linatron-M3 linear accelerator. The estimated dose at the sample was 25 R. A 3.2 mm diameter portion of the sample was stimulated diffusely from within the integrating sphere; the laser power at the sample was 60 µW. Matlab software operating on a personal computer was used to collect the data generated. For comparison, measurements were also made using a commercial storage phosphor made by Fuji Photo Film Co. (type ST-VI).

For gamma-ray imaging, the sample was exposed using a 2 MeV source (Varian Medical Systems Linatron-M3) at a distance of 1.8 m. A 1.3 mm thick tantalum plate was used to condition the beam. Incident exposure at the tantalum plate was approximately 120 R. Lead backing prevented backscattering. Two types of phantoms were used during the imaging process. The first was an assembly of two, 25.4 mm

thick, 440 stainless steel plates, with one plate machined to create a series of small gaps with widths of 5.1, 10.2, 25.4, 50.8, 101.6, 203.2, and 508.0 µm between the two plates (see Figure A6 in the Appendix). The second was a depleted uranium step wedge phantom with 12.7 mm wide steps, which increased in thickness from 1.6 mm to 25.4 mm, in 1.6 mm increments. Readout was obtained using a custom benchtop storage phosphor scanner (see Figure A4 in the Appendix), similar to the one detailed in Lubinsky *et al* [69]. The laser beam had a power of 60 mW and was focused to a $1/e^2$ diameter of approximately 200 µm on the sample. Pixel size, determined by the scan velocity (20 mm per second), sampling rate (80 samples per second), and transverse step size, was 250 µm in both directions.

Because storage phosphor plates are light-sensitive after exposure, several precautions were taken during the experiment to prevent unwanted recombination of the electron-hole pairs. First, the plates were exposed within light-tight containers. Secondly, after exposure, the plates were transported from the source to the readout within the light-tight containers, where they remained until readout. Thirdly, positioning of the plates in the readout device was achieved using a low-power, red LED light. Lastly, ambient lighting in the room where readout occurred was reduced to the minimum necessary to carry-out the experiments.

Results and Discussion

Differential Scanning Calorimetry

The DSC scan yielded a complex curve with multiple crystallization events (see Figure 43). The onset of the glass transition occurred at a temperature of about 212 °C. The large exothermal peak at 253 °C represents the formation of hexagonal $BaCl_2$ crystals [57, 66]. At higher temperature, these crystals undergo a solid state transformation to the orthorhombic phase [68]. The exothermic peak, associated with the hexagonal-to-orthorhombic phase change, is obscured in this scan by a larger peak at 286 °C; the phase associated with this peak is unknown at this time. Because the precise phase transition temperature was not evident from the DSC scan, several trial-and-error heat

treatments were required to determine a suitable protocol for producing $BaCl_2$ in the orthorhombic phase, the presence of which could be verified by XRD, phosphorimetry, SEM, and TEM.

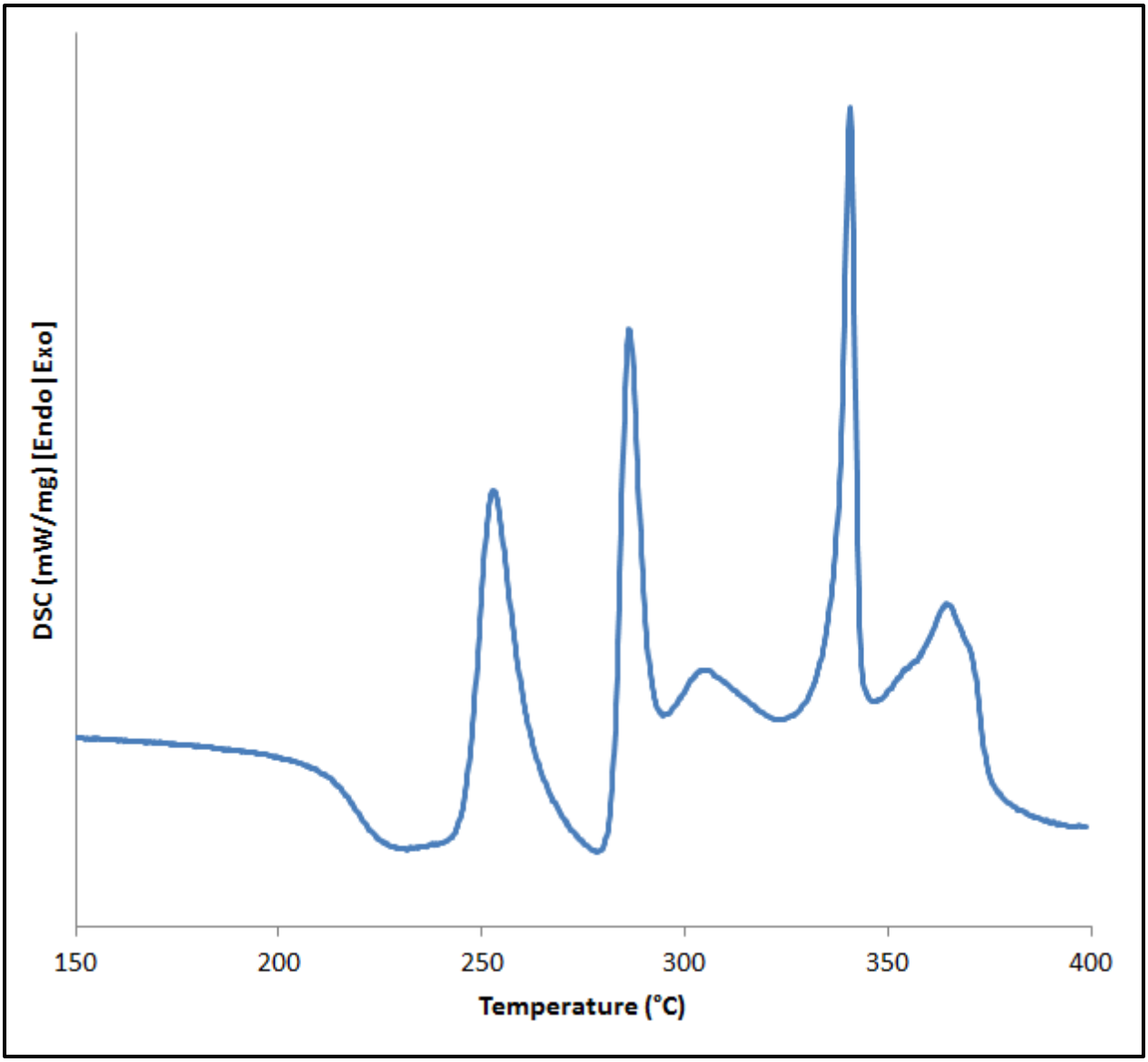

Figure 43. DSC scan at a rate of 1 K per minute for the sample glass.

X-ray Diffraction

X-ray diffraction results confirmed that crystals precipitated during the heat-treatment process for the glass (see Figure 44). In the diffractogram, peaks from both the orthorhombic (Powder Diffraction File PDF 24-0094) and hexagonal (Powder Diffraction File PDF 45-1313) phases of $BaCl_2$ can be identified, indicating the presence of both crystal types. There are also several large peaks present from an, as yet unidentified, crystal phase. Schweizer et al., found this phase to have hexagonal symmetry and lattice parameters of a = 0.39 nm and c = 0.407 nm, but did not report chemical composition [20]. The unidentified phase may play a role in storage phosphor performance and is the subject of ongoing research. Unknown phases have also been found in other FCZ glasses [9, 12].

Because there is much overlap between the diffraction peaks of hexagonal $BaCl_2$ and the other phases, it is difficult to ascertain its relative concentration in the sample. Although, the diffraction peak at approximately 34° would seem to indicate a significant amount of hexagonal $BaCl_2$ in the sample, care must be taken because some peak intensity may be due to diffraction from an unidentified phase. For this reason, phosphorimetry was also used to provide a better estimate of hexagonal content.

Phosphorimetry

The photoluminescent emission spectrum can give insight into the phase of $BaCl_2$ present in FCZ glass ceramic samples [7, 74, 79]. It is particularly useful because trace amounts of crystal that are not detectable by XRD can produce an observable emission peak. A single emission peak centered at approximately 402 nm is associated with $BaCl_2$:Eu^{2+} in the orthorhombic phase; emissions at 410 and 470 nm are associated with $BaCl_2$ in the hexagonal phase [12]. The emissions centered at 402 and 410 nm for the orthorhombic and hexagonal phases, respectively, are attributed to the 5d-4f band emission of Eu^{2+}, with the difference in wavelength position being due to the different crystal environments [1, 80]. For the hexagonal phase, emission at 470 nm is attributed directly to the $BaCl_2$ crystal itself and will occur regardless of whether or not Eu^{2+} is present with the FCZ glass matrix, although the presence of Eu^{2+} will change the

excitation spectrum [66]. The luminescent properties of hexagonal $BaCl_2$ outside of a glass matrix have not been studied extensively because it is metastable and cannot be grown as bulk crystals [63, 81].

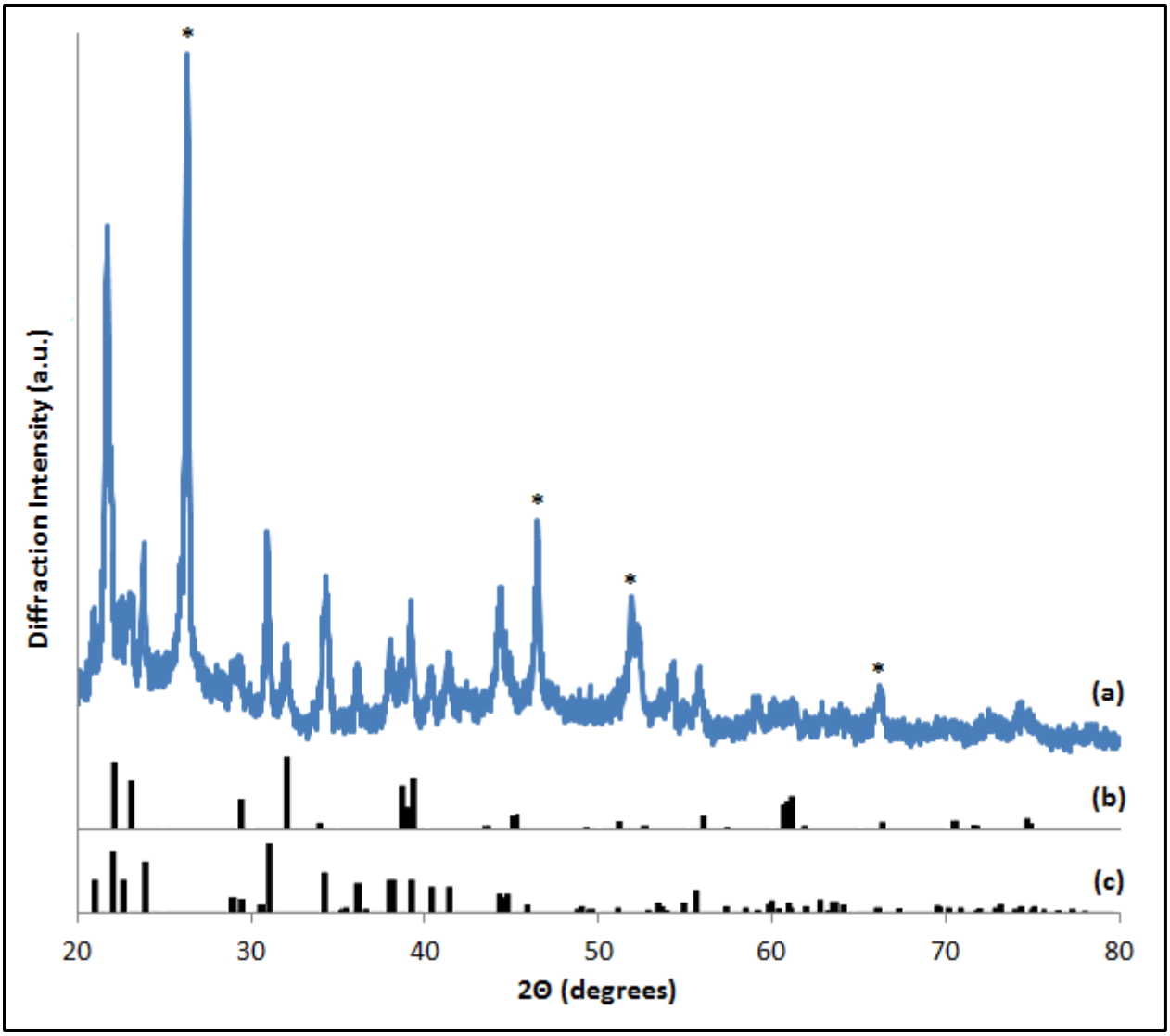

Figure 44. (a) The X-ray diffractogram for the sample glass ceramic, (b) the pattern for orthorhombic phase $BaCl_2$ (PDF 24-0094), and (c) the pattern for hexagonal phase $BaCl_2$ (PDF 45-1313). The "*" indicates major diffraction peaks of an unidentified phase.

The emission and excitation spectra for the sample are shown in Figure 45. The emission spectrum includes a large peak centered at 402 nm, indicating the presence of significant quantities of $BaCl_2$ in the orthorhombic phase. There is, however, a small shoulder extending from the large peak at 402 nm to about 550 nm; this is a sign that a small volume of hexagonal $BaCl_2$ is also present in the sample. These findings are in agreement with the XRD results, although the hexagonal content appears to be much smaller than that suggested by XRD. It is important to have a high ratio of orthorhombic-to-hexagonal phase crystals in the imaging plate, because the hexagonal phase does not significantly contribute to storage phosphor emission [79].

SEM and TEM

The backscattered electron image in Figure 46a highlights the location of the $BaCl_2$ crystals within the glass matrix. The crystals show up with bright contrast. The glass ceramic has a high density of randomly orientated $BaCl_2$ crystals. Because it is difficult to infer the morphology using only SEM, a focused ion beam system was used to view a cross section of the glass ceramic. The FIB system was also used to make the TEM specimen, with the TEM lamella sectioned out of the same specimen from which the cross-section was made. The cross section lamella highlights the random orientation of the crystals and their rounded disc shape (Figure 46b).

Dark-field TEM imaging was used to locate and characterize the structure and morphology of the crystals. The bright and dark contrast in the image, as shown in Figure 47a, corresponds to crystals in the matrix. The crystals vary in size, but generally are ~0.5-0.7 μm rounded discs that are ~0.2 μm thick. The difference in density of crystals between the TEM and SEM images is due to the large increase in magnification. The TEM specimen was tilted to multiple orientations to identify the crystal structure of the embedded crystals. Figure 47b shows an SAED pattern recorded down the [001] zone axis of an orthorhombic $BaCl_2$ crystal. For comparison, a simulated pattern with the same orientation is also shown in Figure 47c. The simulated pattern contains both the allowed reflections (black) and forbidden reflections (white). The SAED patterns from the orthorhombic $BaCl_2$ crystals also contain both the allowed and

forbidden reflections; this is due to the high thickness of the crystals that leads to the formation of double diffraction spots. The pattern shown in Figure 47b indicates that the precipitate from which it is recorded is a single crystal. Additionally, the SAED patterns show that the crystals go through the thickness of the TEM lamella, because of the lack of any amorphous diffraction from the glass matrix.

The size of the embedded crystals (~0.5-0.7 μm) is much larger than reported in similar work [79]. The size of the crystals is of the same order as the stimulating laser wavelength (532 nm), which will lead to reduced resolution in imaging applications, due to scattering. Future work will focus on optimization of the heat-treatment process to reduce the crystal size for increased resolution.

It should be noted that the TEM characterization did not reveal the presence of any hexagonal phase $BaCl_2$ in the sample. This indicates that the volume of the hexagonal phase is very small in the sample, in agreement with the phosphorimetry results.

Photostimulated Emission Measurements

After exposure to 1 MeV radiation, the light emission under constant stimulation was observed as a function of time for the sample, (see Figure 48). For ease of comparison, the PSL data can be fitted to an exponential decay curve (see equation 1), where I_0 is the initial signal intensity and λ is the stimulation speed (decay rate).

$$I(t) = I_0 \times \exp(-\lambda t) \quad (2)$$

The initial intensity is proportional to the fraction of the absorbed energy stored, optical cross-section, laser stimulating power, and the system gain. The decay rate is proportional to the optical cross-section of the storage states in the material. Faster decay times (larger values of λ) reduce the readout times and are desirable in storage phosphor materials used in imaging applications. Another important attribute is the gain (the number of stimulated photons per absorbed x-ray), which is proportional to the area

under the decay curve, I_0/λ. Higher gains reduce exposure time (dose) and improve the signal-to-noise ratio.

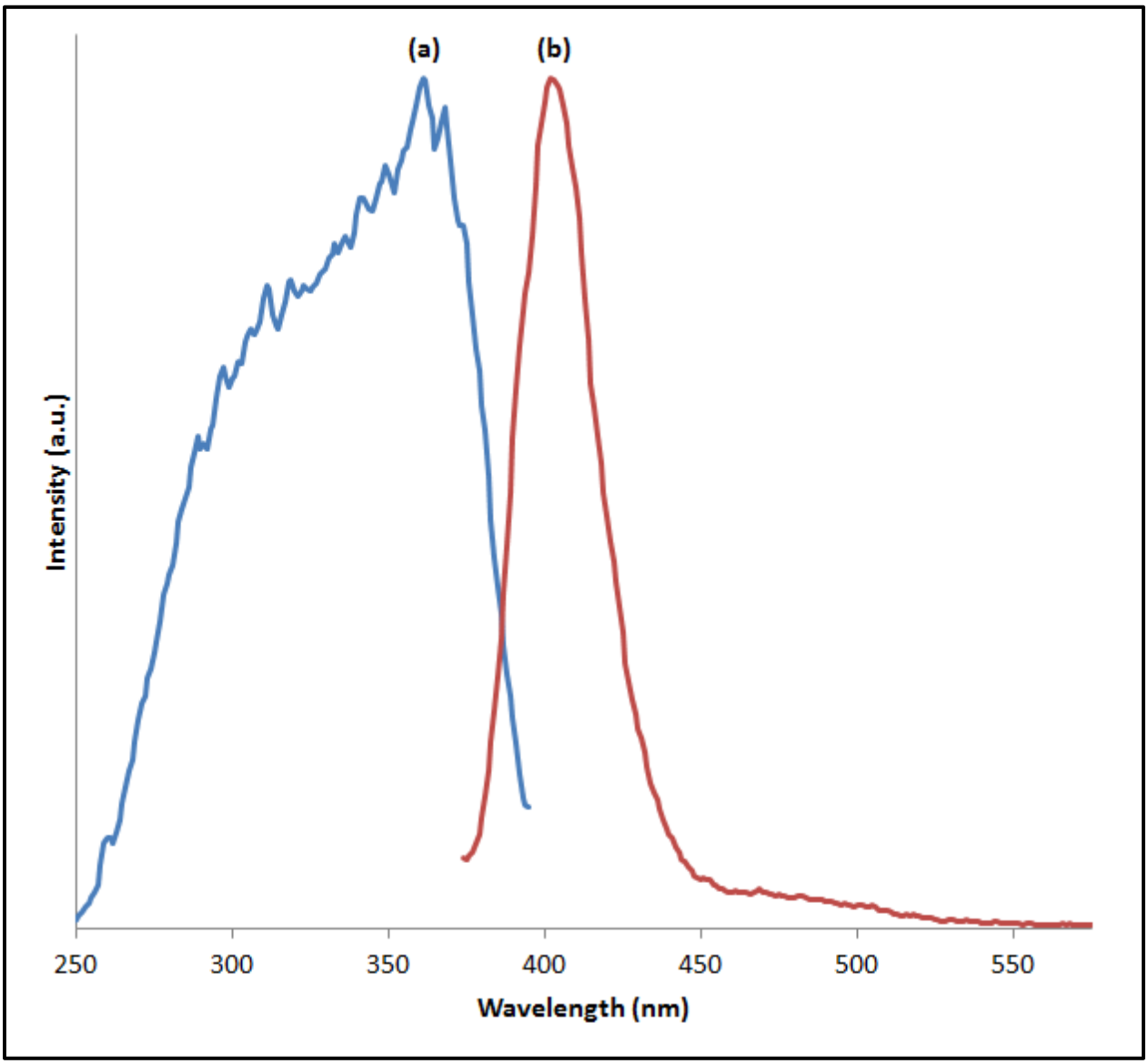

Figure 45. (a) The excitation spectrum and (b) emission spectrum for the sample FCZ glass-ceramic imaging plate. The emission wavelength was 410 nm for the excitation scan. The excitation wavelength was 360 nm for the emission scan.

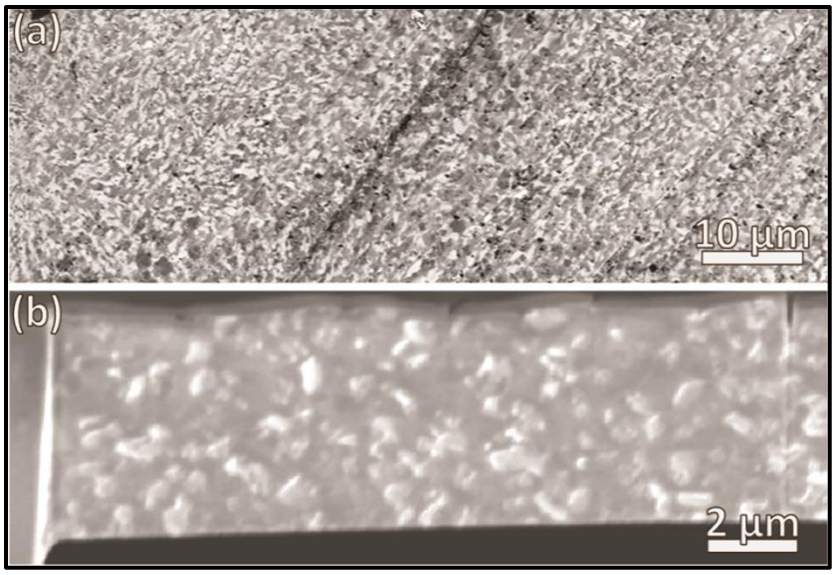

Figure 46. (a) Backscattered electron image of the heat-treated specimen (uncoated). (b) SEM image of heat-treated FIB lift-out specimen during the final milling process.

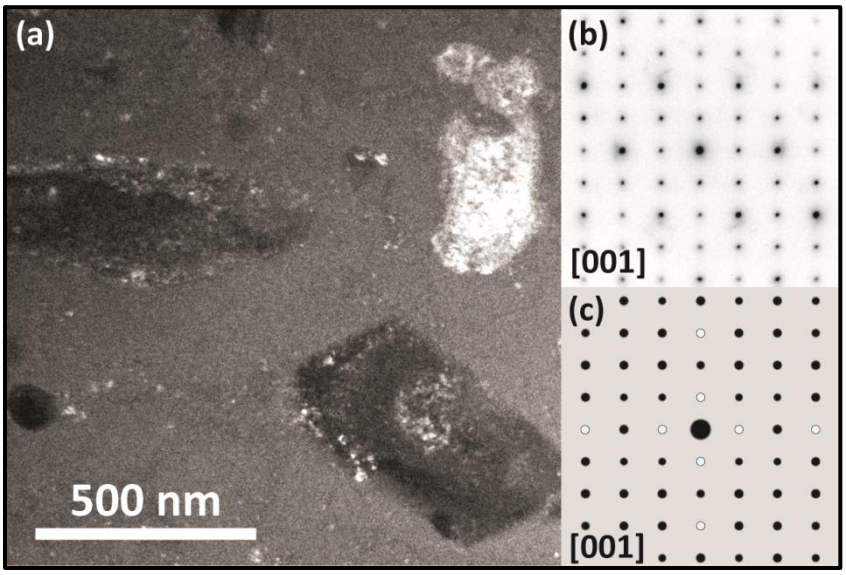

Figure 47. (a) Dark-field TEM image of orthorhombic $BaCl_2$ crystals in the FCZ glass matrix. (b) The SAED pattern of the [001] zone axis of one of the orthorhombic $BaCl_2$ crystals and corresponding (c) simulated SAED pattern with forbidden reflections shown (white spots).

The results from the FCZ glass ceramic were compared to those from a Fuji commercial storage phosphor plate used for medical imaging, which contains barium fluorobromide crystals doped with divalent europium ($BaFBr:Eu^{2+}$). The well-known storage phosphor properties of $BaFBr:Eu^{2+}$ make it an excellent benchmark [36].It should be noted that, although satisfactory for the general comparison purposes described here, the fitted decay curve for $BaFBr:Eu^{2+}$ with a single decay constant, as expected, deviates somewhat from the measured PSL decay curve because the material possesses two types of F-centers (F^- and Br^-). The FCZ glass ceramic sample had 26.7% of the gain and 28.1% of the stimulating speed of the commercial storage phosphor. The system gain in storage phosphors arises from a series of several processes: storage, stimulation, light escape, collection, and detection. Since the last two were kept constant in the experiments, the authors conclude that some or all of the first three processes are more efficient in the commercial material. The increased stimulating speed may be due to a larger optical cross-section (generally assumed to be F-centers in the commercial material), or to increased scattering of the stimulating light. The attributes of the sample plate, however, are quite sufficient to allow for imaging at 1 MeV; test images are shown in the subsequent section.

The total integrated photon flux from the sample may be calculated with the PMT quantum efficiency at the emitted wavelength (24%), filter transmittance (75%), PMT gain ($1.3x10^5$), and current amplifier transimpedence ($1x10^6$ ohm). From this value, the conversion efficiency (CE), defined as the total released photon energy per incident x-ray dose, may be estimated [78]:

$$CE = \frac{I_0}{\lambda \times absorbed\ x{-}ray\ dose} \qquad [3]$$

For the sample measured here, with an incident dose of 40 R at 1 MeV and 1.3 mm tantalum filtration, CE is estimated as 0.11 nJ/(R-mm^2).

The stimulation exposure (SE) was calculated using the incident stimulating laser power (P = 60 μW), and the measured time for 1/e decay of the PSL signal [78]:

$$SE = \frac{P}{\lambda} \quad [4]$$

For the FCZ glass-ceramic image plate, at the exposure conditions as above, SE is estimated as 2.5 x 10^{-4} J/mm^2.

The above results were obtained by measuring the light output from the side of the phosphors which faced the impinging radiation (front face). By exposing two identical portions of the sample image plate at the same time, it was possible to compare the light output from the side facing the radiation source (front face) with the opposite side (back face) as shown in Figure 49. Evidently, significantly more energy is stored towards the back of the sample, under the 1 MeV exposure conditions. At high incident photon energies, the extended range of the energetic charged particles created is expected to result in a dose “build-up” region extending from the front of the plate to a depth equal to the particle range. An alternate explanation is that as the impeded radiation inelastically scatters forward through the sample, the reduced energy of the photons is more conducive to the creation of the electron-hole pairs necessary for PSL.

Gamma-Ray Computed Radiography

A sample image recorded under 2 MeV exposure conditions using the gap phantom is shown in Figure 50a. In the image, the 101.6, 203.2, and 508.0 μm wide gaps in the phantom are visible. Figures 50b, 50c and 50d, show the average profile across each gap in the areas detailed in Figure 50a. The features in the image measured wider than their actual dimensions in the phantom. Some widening of features in the image is due to Compton scattering within the tantalum filter and the image plate. Photoelectric interactions within the image plate also add to the spreading, due to the emission of x-rays and their subsequent re-absorption at other locations. Other factors such as large sampling pixel size and scattering of the stimulating light by the relatively large crystals in the glass matrix can also contribute to the spreading. Parameters were not optimized,

so it would be reasonable to expect features on the order of tens of microns to be imaged following further optimization. One simple way to reduce scattering would be to use thinner image plates, although a drop in light output would be expected to accompany the increased resolution. Future studies will use a more advanced telecentric scanner, capable of fully realizing the resolution potential of the samples [69].

There is a non-zero baseline in each profile due to partial transmission of the incident radiation through the stainless steel phantom plate. Each profile has a different value for the baseline that is attributed to partial recombination of electron-hole pairs before readout: this varies with time and therefore readout position–the portion of the plate scanned last experiences the most unwanted recombinations. In CR, stimulating light can be reflected off the sample, and then further reflected back onto the sample by the imaging system's collector assembly to create recombination in regions of the sample not yet scanned, thus, reducing the signal. In addition, even in complete darkness, storage phosphor plates will experience some recombination at room temperature due to thermal stimulation, a phenomenon known as dark decay. Because the number of electron hole pairs is reduced, light output will diminish over time. The effects of these two phenomena are especially evident in this image due to the relatively large vertical distance between profiles and the slow vertical scan rate in the readout system used, which exacerbates both problems. The estimated time between the first profile, Figure 50b and the last, Figure 50d, is considerable: at 8 minutes and 45 seconds. Again, future studies will be conducted with a faster, more advanced telecentric scanner which should greatly reduce these issues [69]. Nonuniform exposure can also lead to changes in baseline values. However, the exposure distance was sufficiently long (1.8 meters) in the experimental setup, so that nonuniformity is not believed to be a significant contributing factor.

A sample image of the depleted uranium step wedge phantom is shown in Figure 51. Assuming Kramers' law for the bremsstrahlung radiation emitted from the W anode of the Varian Linatron-M3 source, the intensity spectrum transmitted though the various thicknesses of the step wedge and the tantalum filter, and incident on the storage

phosphor can be calculated. This was done for several energies between 0 and 2 MeV, and for each of the five steps (including zero thickness) illustrated in the image shown in Figure 51. The NIST tables of x-ray mass attenuation were used for the calculations. The PSL signal produced by the sample for each step was measured, with a variability of about 5%. By integration of the incident spectra over energy, the total energy and the total number of photons incident on the sample can be calculated, for each step of the image. The resultant PSL signal is plotted as a function of incident energy, photon number, and step thickness in Figures 52, 53, and 54. In addition, the estimated absorbed dose, shown in Figure 55, was calculated based upon a 120 R exposure at the tantalum filter and the calculated transmitted energy spectrum. The PSL response is found to be linear versus the total incident energy and absorbed dose, but not linear versus photon number or phantom step thickness. The linear response to incident energy and absorbed dose shows that the plates also have potential for dosimetry verification in portal imaging and for additional dosimetry applications, as a large area, two-dimensional reusable detector [82, 83].

Conclusions

The FCZ glass-ceramic storage phosphor plate showed potential for use as an imaging plate for gamma-ray computed radiography and dosimetry applications. Although the sample has only 26.7% of the gain and 28.1% of the stimulating speed of a commercial storage phosphor, its attributes are quite sufficient to allow for imaging at MeV energies. Gaps as small as 101.6 μm in a 440 stainless steel phantom were imaged using the sample plate. Analysis of an image created using a depleted uranium step wedge phantom showed that photostimulated emission is proportional to incident energy at the sample and also to the estimated absorbed dose. The sample was found to contain large (0.5-0.7 μm) orthorhombic $BaCl_2$ crystals in an FCZ glass matrix, which may account for the limited image resolution. Optimization of the heat treatment process should lead to a reduction in crystal size and increased resolution in imaging applications. Future studies will use a more advanced telecentric scanner, capable of

fully realizing the resolution potential of the samples. The ability of the plate to generate an image at MeV energies with complementary dosimetry information indicates potential for use in portal imaging applications.

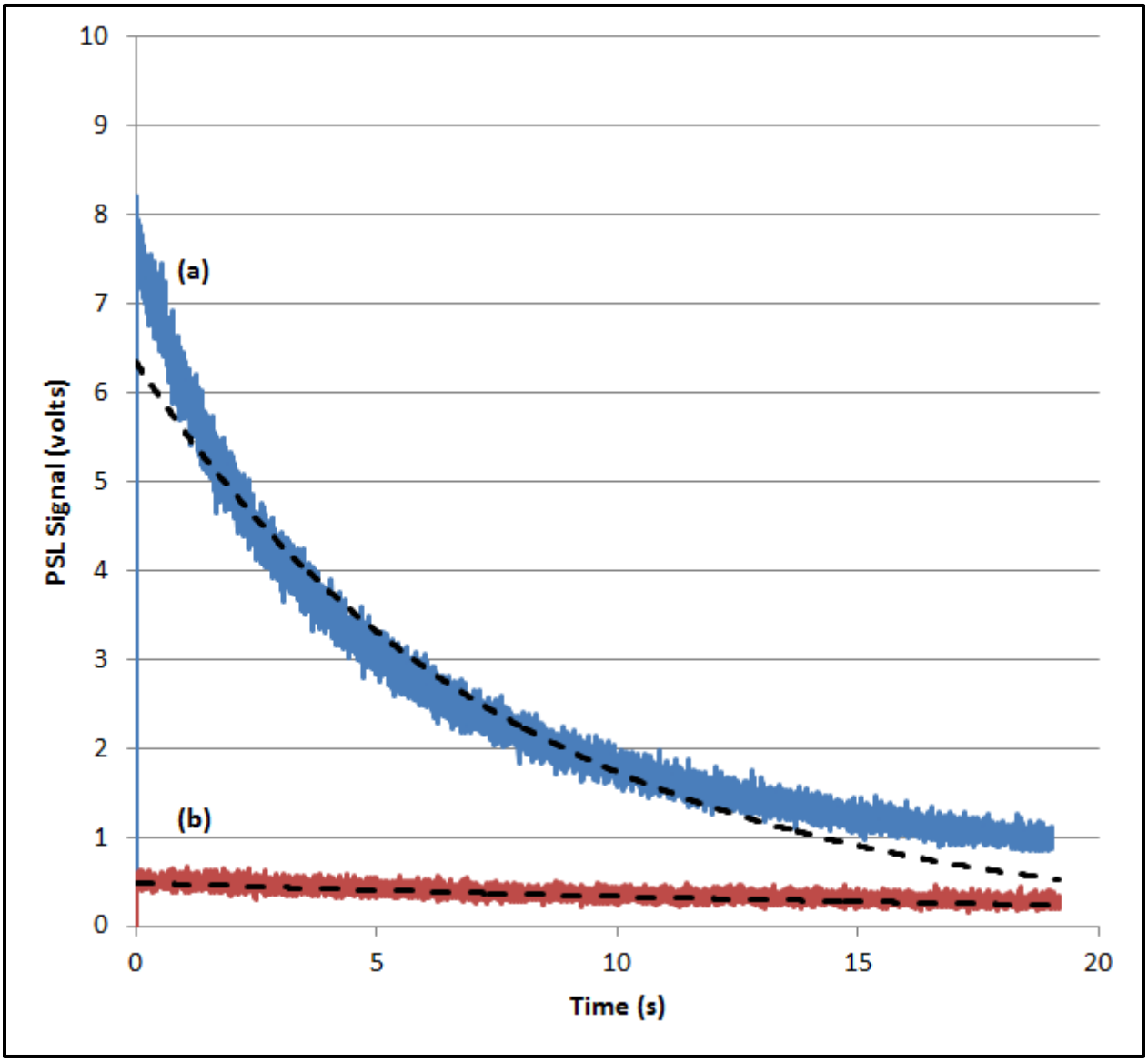

Figure 48. PSL decay curves for a) the commercial storage phosphor plate and b) the sample FCZ glass-ceramic imaging plate. Curve fits are shown with a dashed line.

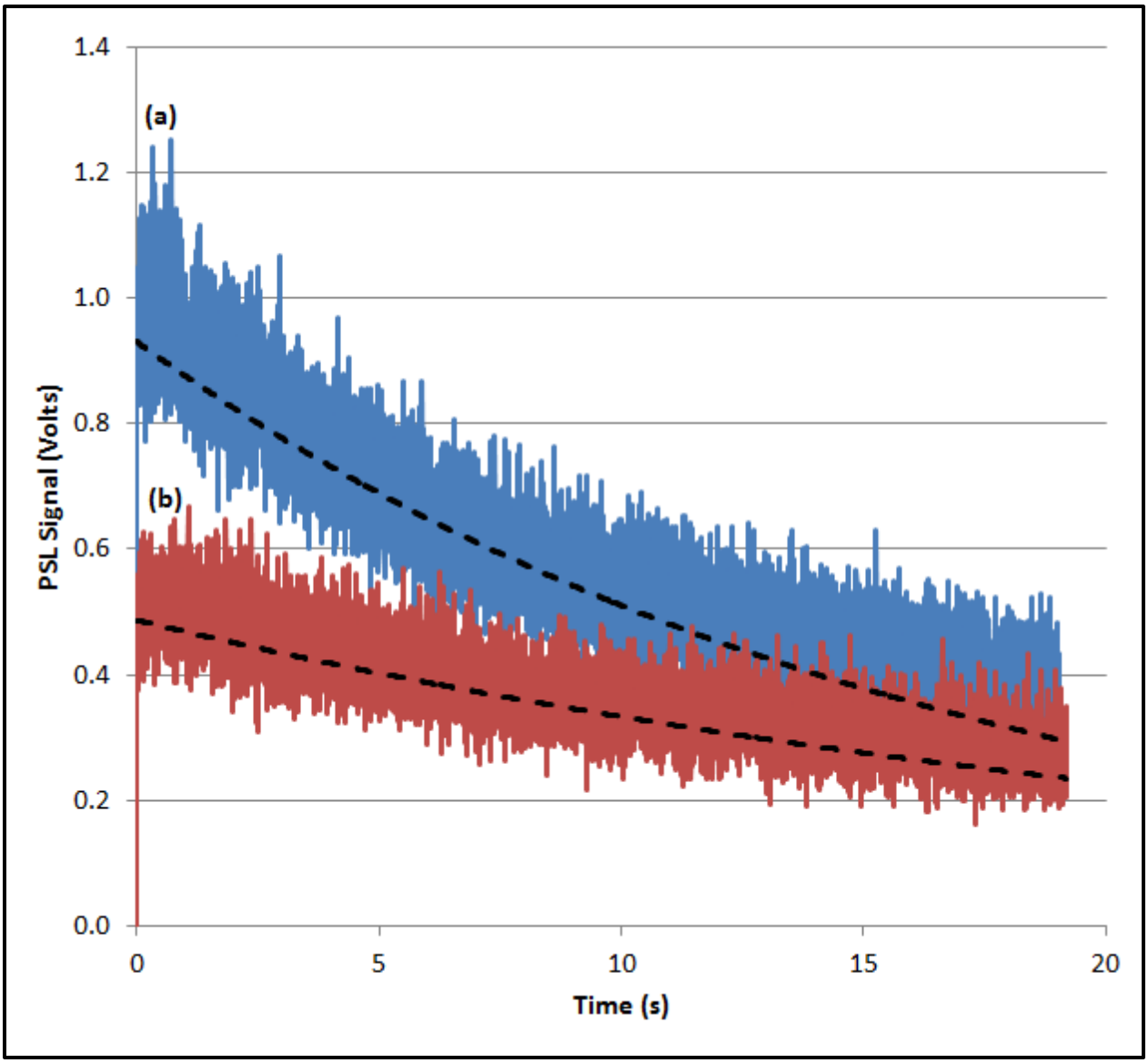

Figure 49. Comparison of PSL decays curves from the (a) back face and (b) front face of the sample imaging plate in relationship to the radiation source. Curve fits are shown with a dashed line.

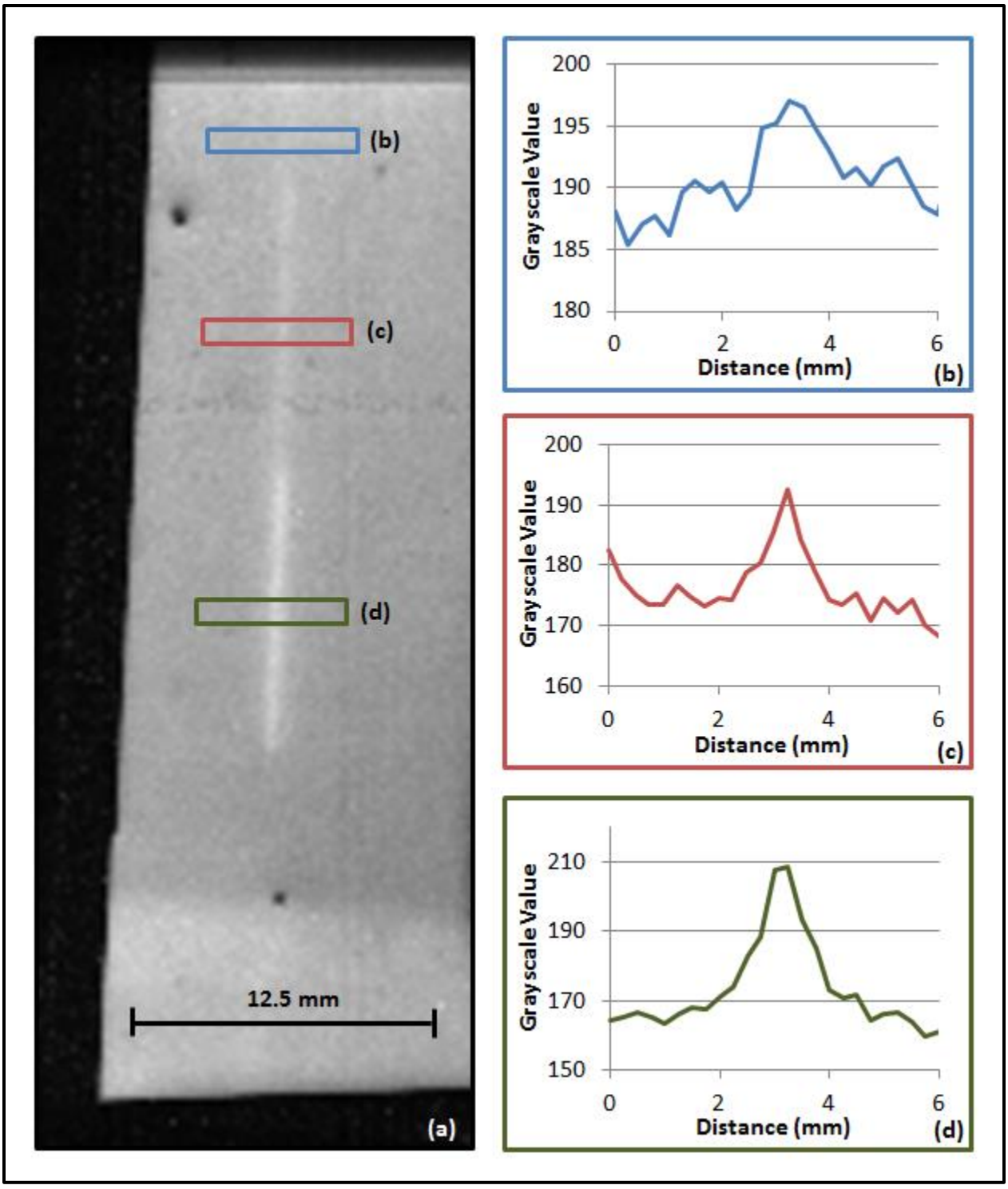

Figure 50. (a) Image of the 440 stainless steel gap phantom using the sample imaging plate with corresponding profiles taken at the (b) 101.6, (c) 203.2, and (d) 508.0 µm thick gaps.

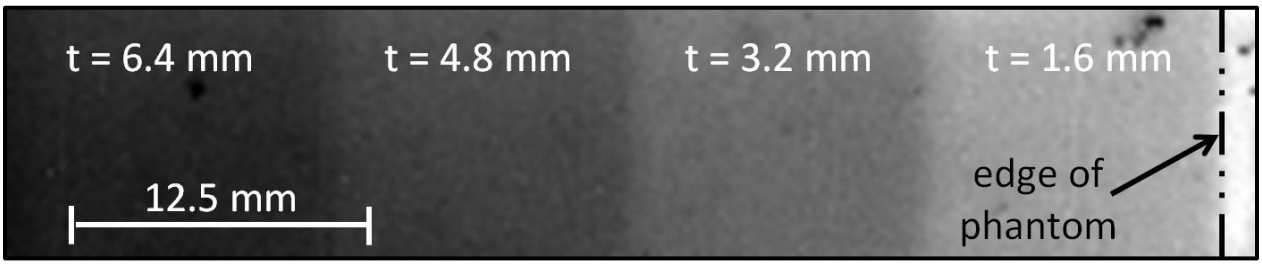

Figure 51. Image of a portion of the depleted uranium step wedge phantom using the sample imaging plate, with the thickness of each step of the phantom indicated.

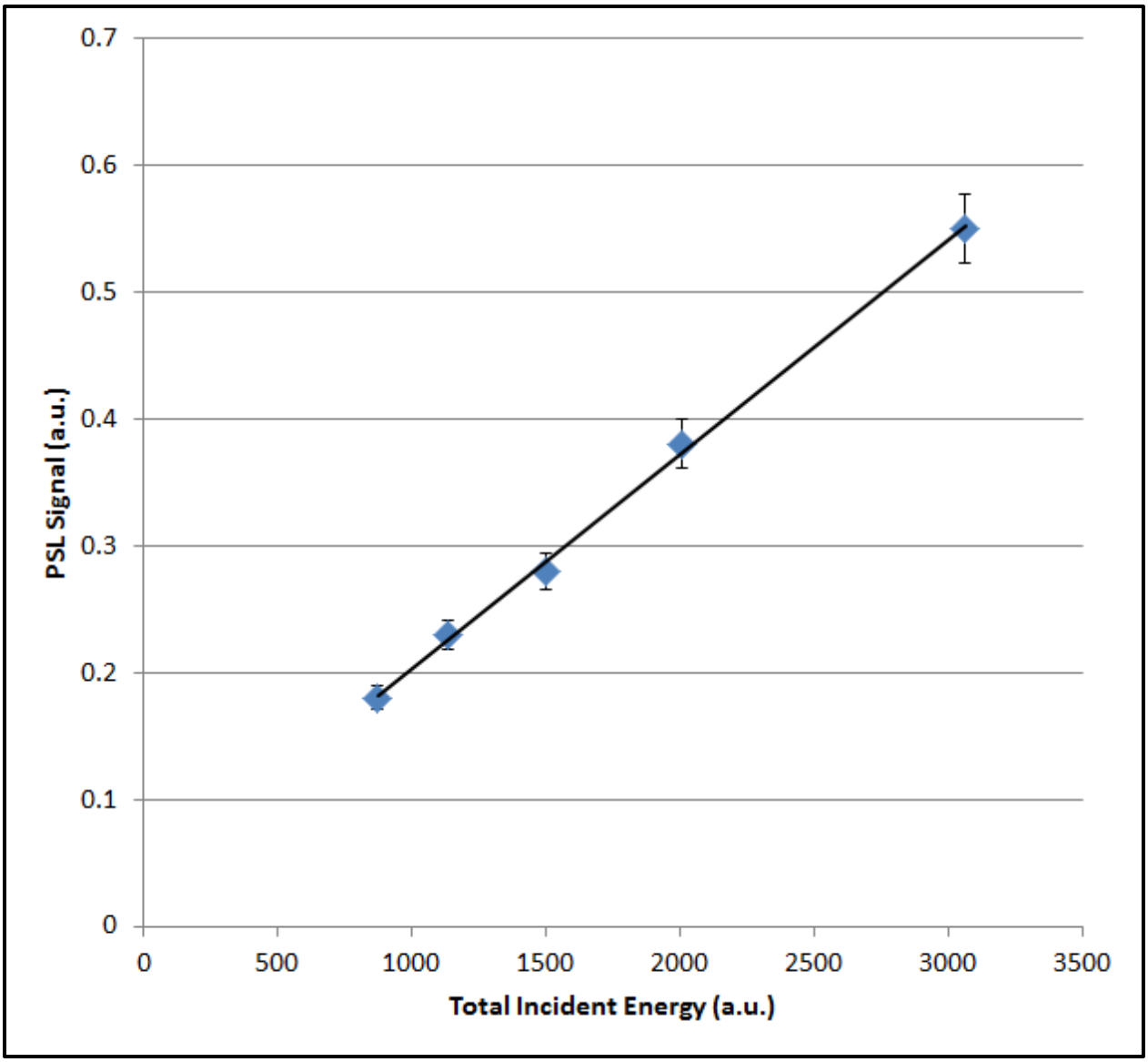

Figure 52. PSL signal versus incident energy derived from an image of the step wedge phantom using the sample imaging plate. A linear trendline is shown in black.

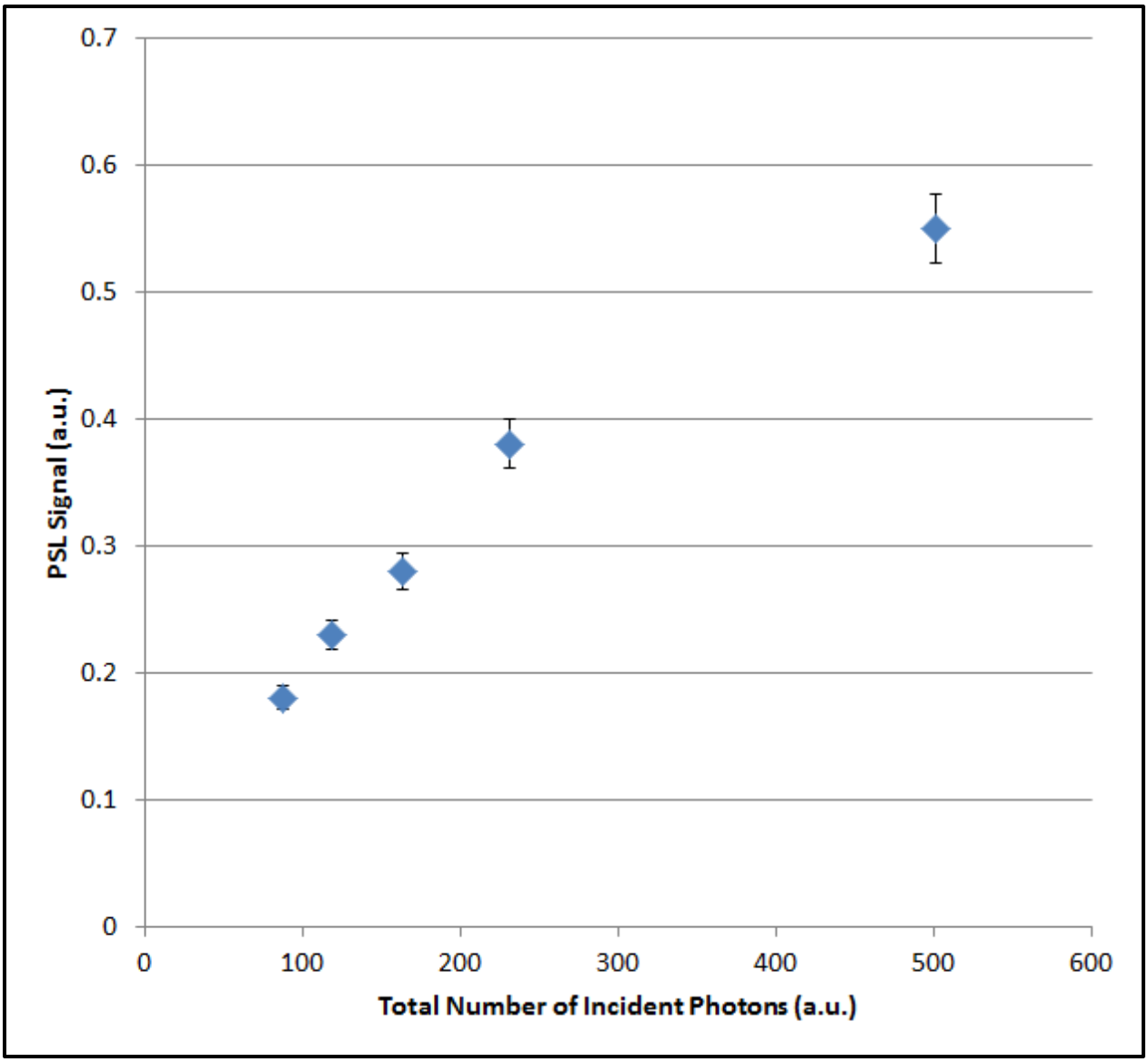

Figure 53. PSL signal versus the number of incident photons derived from an image of the step wedge phantom using the sample imaging plate.

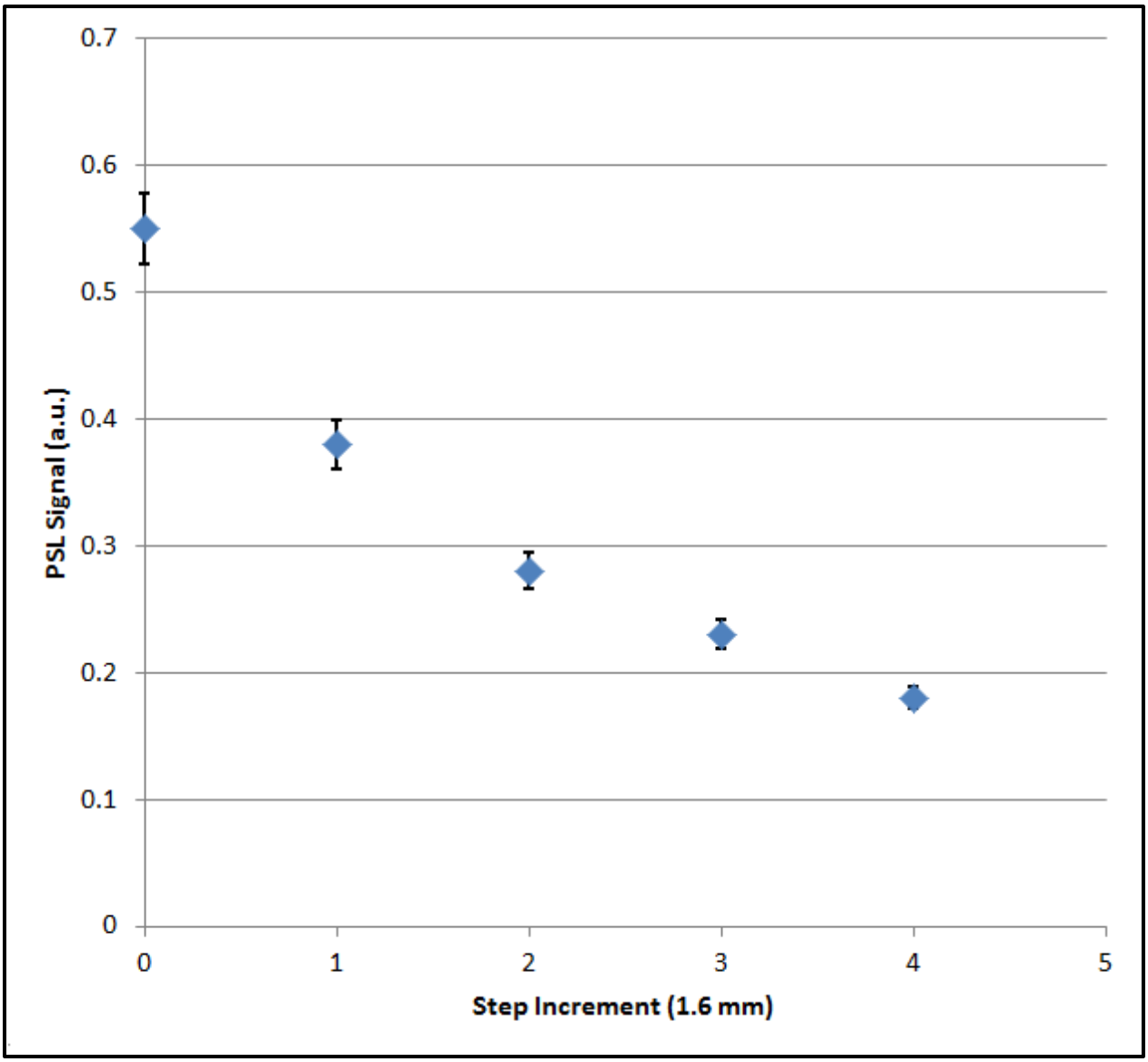

Figure 54. PSL signal versus the step increment derived from an image of the step wedge phantom using the sample imaging plate.

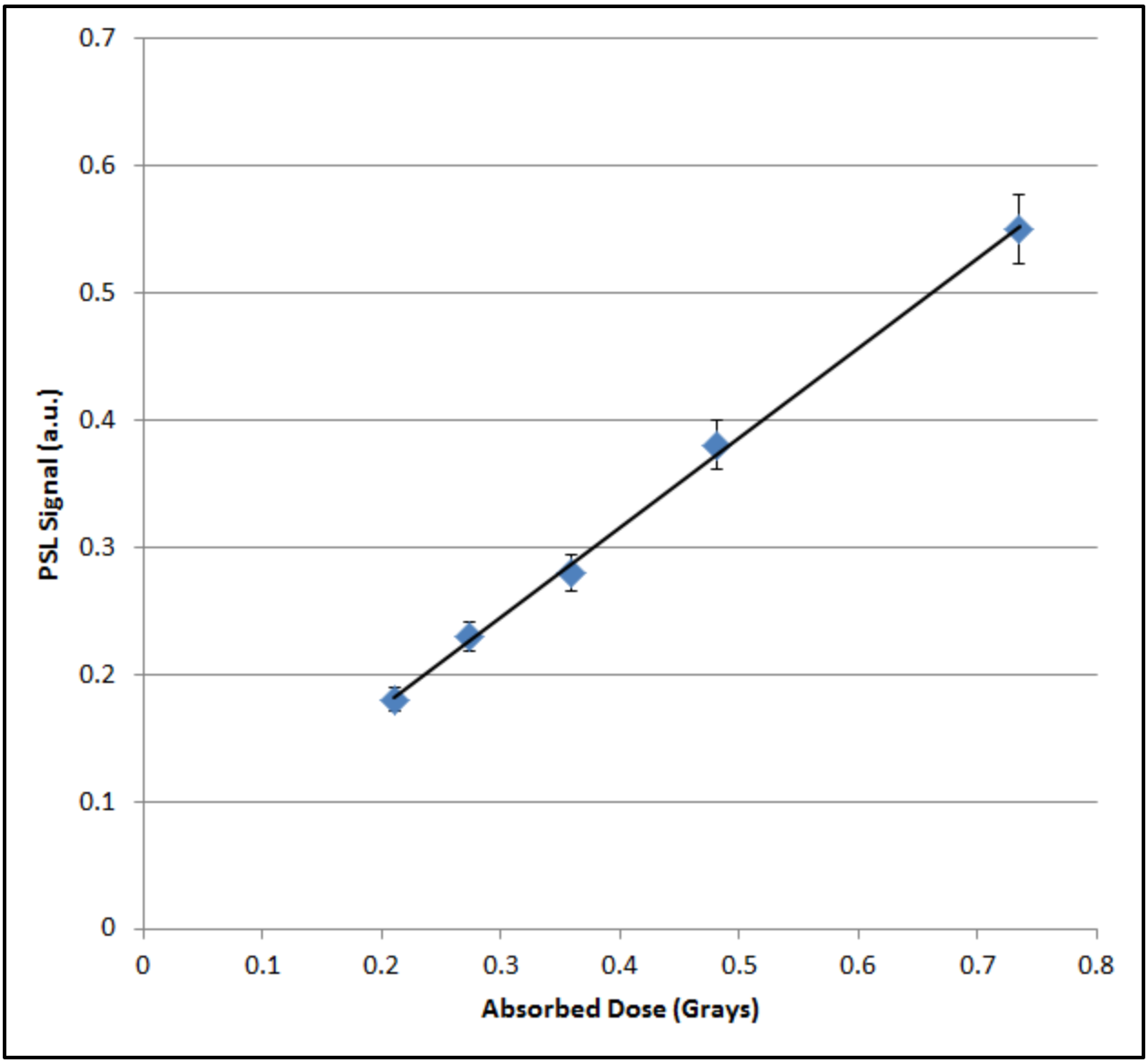

Figure 55. PSL signal versus the estimated absorbed dose derived from an image of the step wedge phantom using the sample imaging plate. A linear trendline is shown in black.

CHAPTER V: CONCLUSION

FCZ glass ceramics were successfully synthesized for both photovoltaic and computed radiography applications, demonstrating the versatility of these materials. Characteristics of the materials were tailored through the use of dopants and other compositional changes. The phase of the $BaCl_2$ crystals, hexagonal or orthorhombic, present in the glass matrix, was critical to each application and was controlled by the heat treatment process.

FCZ glass ceramics containing hexagonal $BaCl_2$ nanocrystals were shown to effectively downshift ultraviolet light, resulting in emissions in the visible portion of the spectrum, that are more favorable for polycrystalline silicon photovoltaic cells. Doping with Eu^{2+} altered the excitation spectrum of the materials, making it more closely match the incident solar spectrum at the earth's surface. Ho^{3+} co-doping gave rise to additional emissions at higher wavelengths and nearer to the band gap energy of polycrystalline silicon photovoltaic cells. Using these materials as outer layers for solar cells may increase their efficiency.

The percentage of NaF used in the preparation of FCZ glass ceramics was shown to have a great effect on material properties. With increased NaF content, the molten glass was more stable during synthesis, with significantly reduced losses due to evaporation. Thermal properties were affected, with glass transition, crystallization, and phase transformation temperatures generally reduced with increased NaF content. The amount of NaF used in the synthesis of the samples affected the formation of additional phases at high temperatures that are believed to consume the orthorhombic phase $BaCl_2$:Eu^{2+} crystals responsible for the materials' storage phosphor properties. This result in turn limited the maximum PSL light output achievable after the heat treatment process.

Although the PSL light output of the samples was considerably less than that of commercial storage phosphors at energies typical for intraoral dental radiography, the materials show potential for nondestructive testing, where dose is not a primary concern. Gaps as small as 101.6 μm in a 440 stainless steel phantom were successfully imaged using a sample FCZ glass-ceramic computed radiography imaging plate containing orthorhombic phase $BaCl_2:Eu^{2+}$ crystals after exposure with a source operating at 2 MeV. It was also shown that PSL light output for the imaging plate was proportional to incident energy and estimated absorbed dose, suggesting that these materials may find use in dosimetry applications. The ability of these materials to generate an image at MeV energies with complementary dosimetry information indicates potential for use in portal imaging applications.

REFERENCES

1. Brixner, L.H. and A. Ferretti, *Eu^{2+} fluorescence in $BaCl_2$.* Journal of Solid State Chemistry, 1976. **18**(2): p. 111-116.
2. Onodera, K., M. Koshimizu, and K. Asai, *Luminescent properties of $BaCl_2$ under VUV excitation.* Radiation Physics and Chemistry, 2009. **78**(12): p. 1031-1033.
3. Selling, J., et al., *Europium-doped barium halide X-ray scintillators.* Physica Status Solidi (C), 2007. **4**(3): p. 976-979.
4. Zych, A., et al., *Luminescence properties of lanthanide doped alkaline earth chlorides under (V)UV and X-ray excitation.* Journal of Alloys and Compounds, 2011. **509**(13): p. 4445-4451.
5. Kobayasi, T., et al., *Fluorescence lifetime and quantum efficiency for 5d → 4f transitions in Eu^{2+} doped chloride and fluoride crystals.* Journal of Luminescence, 1980. **21**(3): p. 247-257.
6. Johnson, J.A., et al., *Eu-activated fluorochlorozirconate glass-ceramic scintillators.* Journal of Applied Physics, 2006. **100**(3): p. 034701.
7. Koughia, C., et al., *Samarium-doped fluorochlorozirconate glass–ceramics as red-emitting x-ray phosphors.* Journal of the American Ceramic Society, 2011. **94**(2): p. 543-550.
8. Koughia, C., et al., *Optical and selected thermal properties of samarium-doped fluorochlorozirconate (FCZ) glass-ceramics: formation and growth of $BaCl_2$ nanocrystals in FCZ glass-ceramics.* Journal of Non-Crystalline Solids, 2011. **357**(11–13): p. 2272-2277.
9. Pei, Z., et al., *Luminescence property of Eu-doped fluorochlorozirconate glass-ceramics.* Journal of Rare Earths, 2009. **27**(2): p. 338-340.
10. Pfau, C., et al., *Multiphonon relaxation in rare-earth doped fluorozirconate-based glasses containing $BaCl_2$ nanocrystals.* Journal of Physics: Condensed Matter, 2014. **26**(2): p. 025406.
11. Schweizer, S., et al., *Photostimulated luminescence in Eu-doped fluorochlorozirconate glass ceramics.* Applied Physics Letters, 2003. **83**(3): p. 449.

12. Schweizer, S., et al., *Photostimulated luminescence from fluorochlorozirconate glass ceramics and the effect of crystallite size.* Journal of Applied Physics, 2005. **97**(8): p. 083522.
13. Soga, K., et al., *Site-dependent study of the optical properties of Eu^{3+} in pure and chlorine-doped fluorozirconate glasses.* Journal of the American Ceramic Society, 1995. **78**(1): p. 129-132.
14. Elyamani, A., et al., *Properties of chlorofluorozirconate glasses.* Journal of Non-Crystalline Solids, 1990. **119**(2): p. 187-194.
15. Henke, B., et al., *Erbium- and chlorine-doped fluorozirconate-based glasses for up-converted fluorescence.* Journal of Non-Crystalline Solids, 2009. **355**(37-42): p. 1916-1918.
16. Paßlick, C., et al., *Advances in up- and down-converted fluorescence for high efficiency solar cells using rare-earth doped fluorozirconate-based glasses and glass ceramics.* Next Generation (Nano) Photonic and Cell Technologies for Solar Energy Conversion, 2010. **7772**.
17. Schweizer, S., et al., *Progress on up- and down-converted fluorescence in rare-earth doped fluorozirconate-based glass ceramics for high efficiency solar cells.* Photonics for Solar Energy Systems III, 2010. **7725**.
18. Chen, G., et al., *Fluorozirconate-based nanophase glass ceramics for high-resolution medical X-ray imaging.* Journal of Non-Crystalline Solids, 2006. **352**(6–7): p. 610-614.
19. Johnson, J.A., S. Schweizer, and A.R. Lubinsky, *A glass-ceramic plate for mammography.* Journal of the American Ceramic Society, 2007. **90**(3): p. 693-698.
20. Schweizer, S., et al., *Photostimulated luminescence in Eu-doped fluorochlorozirconate glass ceramics.* Applied Physics Letters, 2003. **83**(3): p. 449-451.
21. Schweizer, S. and J.A. Johnson, *Fluorozirconate-based glass ceramic x-ray detectors for digital radiography.* Radiation Measurements, 2007. **42**(4–5): p. 632-637.

22. Andrews, L.J.H., B.T.; Folweiler, R. C.; Moynihan, C. T. , *In situ oxidation of heavy metal fluoride glasses.* Materials Science Forum, 1991. **32-33**: p. 43-48.
23. Alvarez, C.J., et al., *Structural and kinetic analysis of $BaCl_2$ nanocrystals in fluorochlorozirconate glass-ceramics.* Journal of the American Ceramic Society, 2015. **98**(4): p. 1099-1104.
24. Alvarez, C.J., et al., *Nanocrystallization in fluorochlorozirconate glass-ceramics.* Journal of the American Ceramic Society, 2013. **96**(11): p. 3617-3621.
25. Johnson, J.A., et al., *Crystallization in heat-treated fluorochlorozirconate glasses.* Journal of Physics-Condensed Matter, 2009. **21**(37).
26. Avrutin, V., N. Izyumskaya, and H. Morkoc, *Semiconductor solar cells: recent progress in terrestrial applications.* Superlattices and Microstructures, 2011. **49**(4): p. 337-364.
27. Razykov, T.M., et al., *Solar photovoltaic electricity: current status and future prospects.* Solar Energy, 2011. **85**(8): p. 1580-1608.
28. *Reference solar spectral irradiance: air mass 1.5*. Available from: http://rredc.nrel.gov/solar/spectra/am1.5/.
29. Klampaftis, E., et al., *Enhancing the performance of solar cells via luminescent down-shifting of the incident spectrum: a review.* Solar Energy Materials and Solar Cells, 2009. **93**(8): p. 1182-1194.
30. Lian, H., et al., *Rare earth ions doped phosphors for improving efficiencies of solar cells.* Energy, 2013. **57**: p. 270-283.
31. Strümpel, C., et al., *Modifying the solar spectrum to enhance silicon solar cell efficiency—an overview of available materials.* Solar Energy Materials and Solar Cells, 2007. **91**(4): p. 238-249.
32. Cowen, A.R., A.G. Davies, and S.M. Kengyelics, *Advances in computed radiography systems and their physical imaging characteristics.* Clinical Radiology, 2007. **62**(12): p. 1132-1141.
33. Kang, S.M., et al., *Comparison to images from a computed radiography system for non-destructive testing using selenium-75, iridium-192, and x-rays.* Journal of the Korean Physical Society, 2011. **59**(2): p. 717-720.

34. Kasban, H., et al., *Welding defect detection from radiography images with a cepstral approach.* NDT & E International, 2011. **44**(2): p. 226-231.
35. Rakvin, M., D. Markučič, and B. Hižman, *Evaluation of pipe wall thickness based on contrast measurement using computed radiography (CR).* Procedia Engineering, 2014. **69**: p. 1216-1224.
36. Sonoda, M., et al., *Computed radiography utilizing scanning laser stimulated luminescence.* Radiology, 1983. **148**(3): p. 833-838.
37. Appleby, G.A., et al., *Photostimulated luminescence from $BaCl_2:Eu^{2+}$ nanocrystals in lithium borate glasses following neutron irradiation.* Applied Physics Letters, 2006. **89**(10): p. 101902.
38. Stotzka, R., J. Haase, and T.O. Muller, *3D reconstruction of clustered microcalcifications from two mammograms: information preservation*, in *Medical Imaging 1999: Image Processing, Pts 1 and 2*, K.M. Hanson, Editor 1999, Spie-Int Soc Optical Engineering: Bellingham. p. 1361-1366.
39. Udupa, H., et al., *Evaluation of image quality parameters of representative intraoral digital radiographic systems.* Oral Surgery, Oral Medicine, Oral Pathology and Oral Radiology, 2013. **116**(6): p. 774-783.
40. Vandenberghe, B., R. Jacobs, and H. Bosmans, *Modern dental imaging: a review of the current technology and clinical applications in dental practice.* European Radiology, 2010. **20**(11): p. 2637-2655.
41. Farman, A.G., et al., *In practice - How going digital will affect the dental office.* Journal of the American Dental Association, 2008. **139**: p. 14S-19S.
42. Borg, E., A. Attaelmanan, and H.G. Grondahl, *Subjective image quality of solid-state and photostimulable phosphor systems for digital intra-oral radiography.* Dentomaxillofacial Radiology, 2000. **29**(2): p. 70-75.
43. Farman, A.G. and T.T. Farman, *A comparison of 18 different x-ray detectors currently used in dentistry.* Oral Surgery Oral Medicine Oral Pathology Oral Radiology and Endodontology, 2005. **99**(4): p. 485-489.
44. Farrier, S.L., et al., *A comparative study of image quality and radiation exposure for dental radiographs produced using a charge-coupled device and a phosphor plate system.* International Endodontic Journal, 2009. **42**(10): p. 900-907.

45. Şenel, B., et al., *Diagnostic accuracy of different imaging modalities in detection of proximal caries.* Dentomaxillofacial Radiology, 2010. **39**(8): p. 501-511.
46. Shintaku, W.H., et al., *Comparison between intraoral indirect and conventional film-based imaging for the detection of dental root fractures: an ex vivo study.* Dental Traumatology, 2013. **29**(6): p. 445-449.
47. Kirby, M.C. and A.G. Glendinning, *Developments in electronic portal imaging systems.* The British Journal of Radiology, 2006. **79**(special issue 1): p. S50-S65.
48. Langmack, K.A., *Portal imaging.* The British Journal of Radiology, 2001. **74**(885): p. 789-804.
49. Boyer, A.L., et al., *A review of electronic portal imaging devices (EPIDS).* Medical Physics, 1992. **19**(1): p. 1-16.
50. Das, I.J., et al., *A quality assurance phantom for electronic portal imaging devices*. 2011. Vol. 12. 2011.
51. Gur, D., et al., *The use of storage phosphors for portal imaging in radiation-therapy - therapists perception of image quality.* Medical Physics, 1989. **16**(1): p. 132-136.
52. Partridge, M., B.M. Hesse, and L. Muller, *A performance comparison of direct- and indirect-detection flat-panel imagers.* Nuclear Instruments & Methods in Physics Research Section a-Accelerators Spectrometers Detectors and Associated Equipment, 2002. **484**(1-3): p. 351-363.
53. Schweizer, S., et al., *Multi-functionality of fluorescent nanocrystals in glass ceramics.* Radiation Measurements, 2010. **45**(3-6): p. 485-489.
54. Herrmann, A., S. Fibikar, and D. Ehrt, *Time-resolved fluorescence measurements on Eu^{3+}- and Eu^{2+} -doped glasses.* Journal of Non-Crystalline Solids, 2009. **355**(43-44): p. 2093-2101.
55. Feng, L., et al., *Optical properties of Ho^{3+}-doped novel oxyfluoride glasses.* Journal of Luminescence, 2007. **124**(2): p. 187-194.
56. Paßlick, C., et al., *Differential scanning calorimetry investigations on Eu-doped fluorozirconate-based glass ceramics.* Journal of Non-Crystalline Solids, 2010. **356**(52-54): p. 3085-3089.

57. Paßlick, C., et al., *Crystallization behavior of rare-earth doped fluorochlorozirconate glasses.* Journal of Non-Crystalline Solids, 2011. **357**(11-13): p. 2450-2452.
58. Chen, G., et al., *Insights into phase formation in fluorochlorozirconate glass-ceramic storage phosphors.* Applied Physics Letters, 2006. **88**(19).
59. Ahrens, B., et al., *Structural and optical investigations of Nd-doped fluorozirconate-based glass ceramics for enhanced upconverted fluorescence.* Applied Physics Letters, 2008. **92**(6).
60. Schweizer, S., et al., *Glass ceramics as x-ray storage phosphors for high spatial resolution.* Radiation Measurements, 2001. **33**(5): p. 487-490.
61. Schweizer, S., et al., *Photostimulated luminescence from fluorochlorozirconate glass ceramics and the effect of crystallite size.* Journal of Applied Physics, 2005. **97**(8).
62. Pfau, C., et al., *Structural phase transitions of barium halide nanocrystals in fluorozirconate glasses studied by Raman spectroscopy.* Journal of Applied Physics, 2011. **109**(8).
63. Beck, H.P., *A structure refinement of the high-pressure modification BaI_2-II.* Journal of Solid State Chemistry, 1983. **47**(3): p. 328-332.
64. Ansari, A.A., H.A. Hussain, and K. Iftikhar, *Optical absorption spectroscopic studies on holmium(III) complexes with beta-diketone and heterocyclic amines the environment effect on 4f-4f hypersensitive transitions.* Spectrochimica Acta Part a-Molecular and Biomolecular Spectroscopy, 2007. **68**(5): p. 1305-1312.
65. Henke, B., et al., *Eu oxidation state in fluorozirconate-based glass ceramics.* Journal of Applied Physics, 2009. **106**(11).
66. Leonard, R.L., et al., *Rare earth doped downshifting glass ceramics for photovoltaic applications.* Journal of Non-Crystalline Solids, 2013. **366**: p. 1-5.
67. Leonard, R.L., et al., *Evaluation of a fluorochlorozirconate glass-ceramic storage phosphor plate for gamma-ray computed radiography.* Journal of the American Ceramic Society **98**(8), 2015: p. 2541-2547
68. Alvarez, C.J., et al., *Nanocrystallization in fluorochlorozirconate glass-ceramics.* Journal of the American Ceramic Society, 2013. **96**(11): p. 3617-3621.

69. Lubinsky, A.R., et al. *Scanning translucent glass-ceramic x-ray storage phosphors*. Proc. SPIE, 7622, 76223W (2010).
70. Ohsawa, K. and T. Shibata, *Preparation and characterization of ZrF_4 -BaF_2-LaF_3-NaF-AlF_3 glass optical fibers.* Lightwave Technology, Journal of, 1984. **2**(5): p. 602-606.
71. Aasland, S. and T. Grande, *Crystallization of ZBLAN glass.* Journal of the American Ceramic Society, 1996. **79**(8): p. 2205-2206.
72. Babitsyna, A.A., T.A. Emel'yanova, and V.A. Fedorov, *Glass formation in quaternary systems of group I-IV fluorides.* Inorganic Materials, 2008. **44**(12): p. 1378-1385.
73. Babitsyna, A.A., et al., *Glass formation in the fluorozirconate systems containing lead fluoride.* Glass Physics and Chemistry, 2007. **33**(6): p. 545-549.
74. Alvarez, C.J., *Crystallization kinetics in fluorochloroziroconate glass-ceramics*, in *materials science and engineering,* 2015, Northwestern University: Evanston, Illinois. Dissertation
75. Fujita, H., et al., *Evaluation of image quality in portal imaging using a combination of a storage phosphor plate and diagnostic cassette.* British Journal of Radiology, 2009. **82**(978): p. 504-508.
76. Seggern, H.V., *Photostimulable x-ray storage phosphors: a review of present understanding.* Brazilian Journal of Physics, 1999. **29**: p. 254-268.
77. Paßlick, C., J.A. Johnson, and S. Schweizer, *Crystallization studies on rare-earth co-doped fluorozirconate-based glasses.* Journal of Non-Crystalline Solids, 2013. **371–372**: p. 33-36.
78. Schweizer, S., *Physics and current understanding of X-ray storage phosphors.* Physica Status Solidi A-Applications and Materials Science, 2001. **187**(2): p. 335-393.
79. Schweizer, S., et al., *Photostimulated luminescence from fluorochlorozirconate glass ceramics and the effect of crystallite size.* Journal of Applied Physics, 2005. **97**(8): p. 083522

80. Koughia, C., et al., *Samarium-doped fluorochlorozirconate glass-ceramics as red-emitting x-ray phosphors.* Journal of the American Ceramic Society, 2011. **94**(2): p. 543-550.
81. Pfau, C., et al., *Structural phase transitions of barium halide nanocrystals in fluorozirconate glasses studied by Raman spectroscopy.* Journal of Applied Physics, 2011. **109**(8): p. 083545.
82. O' Keeffe, D.S. and R.W. McLeod, *Computed radiography as a gamma ray detector—dose response and applications.* Physics in Medicine and Biology, 2004. **49**(16): p. 3559.
83. Miyamaru, H., et al., *Gamma-ray transmission evaluation using imaging plate designed for x-ray radiography.* Progress in Nuclear Science and Technology, 2014. **4**: p. 699-703.

APPENDIX

Figure A1. An argon atmosphere glovebox with attached tube furnace.

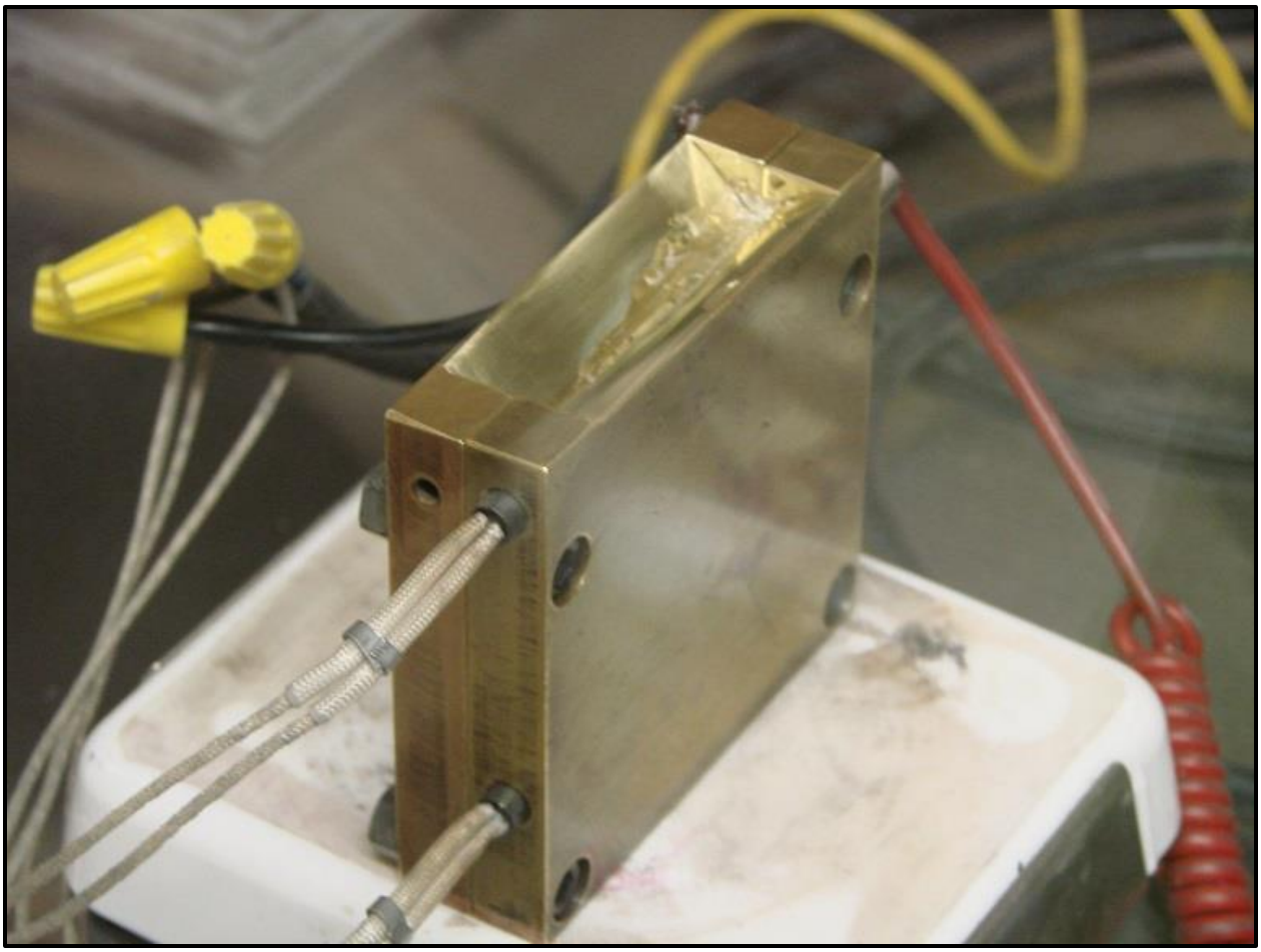

Figure A2. A brass mold with inserted cartridge heaters and thermocouple. A portion of a sample can be seen in the top of the mold.

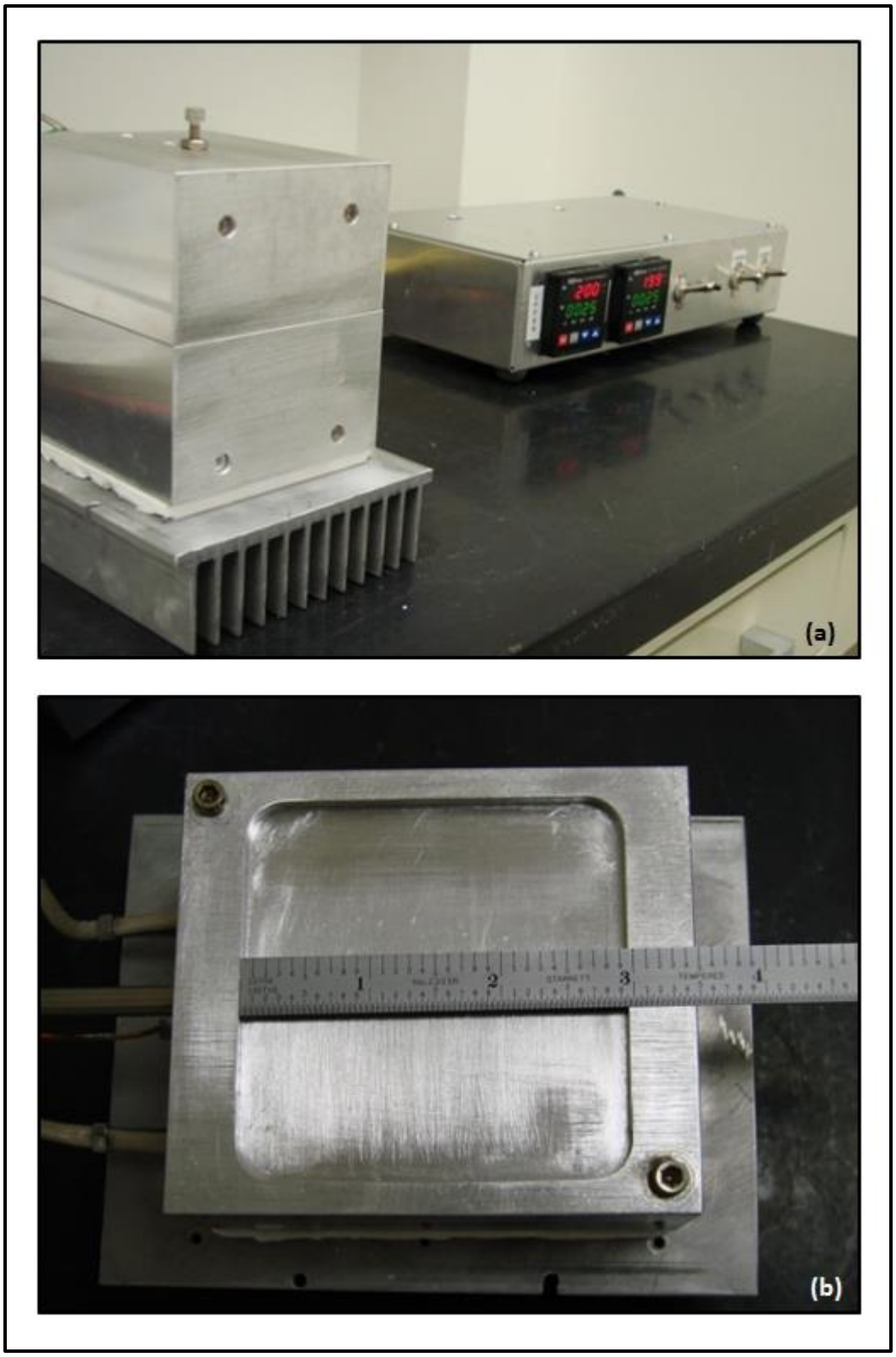

Figure A3. (a) A programmable heat treatment system and (b) the interior of the heat treatment chamber.

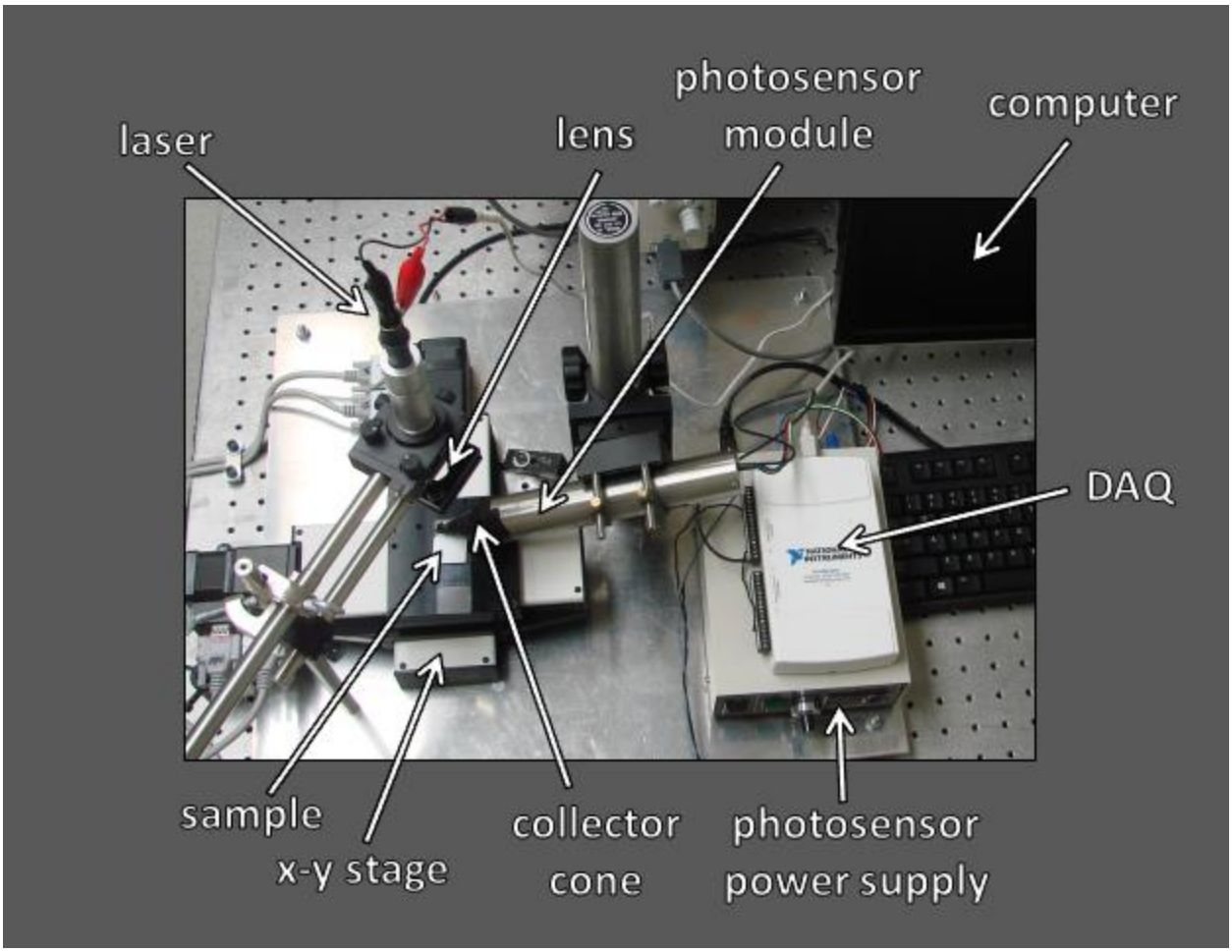

Figure A4. Schematic of a custom benchtop computed radiography scanner. Note: The controller for the x-y stage is not shown.

Table A1. Mass loss caused by evaporation during glass synthesis as a function of NaF content.

NaF (%)	10	15	20	25	30
mass of crucible and ingredients before 1st melt (grams)	52.86	52.97	52.97	52.17	53.04
mass of crucible and ingredients after 1st melt (grams)	51.37	51.77	52.19	51.39	52.58
material lost during 1st melt (grams)	1.49	1.20	0.78	0.77	0.45
mass of crucible and ingredients before 2nd melt (grams)	54.54	54.91	55.27	54.41	55.56
mass crucible plus residue after pour (grams)	47.67	47.29	46.84	46.40	46.93
sample mass (grams)	5.88	6.87	7.83	7.53	8.26
material lost during 2nd melt (grams)	0.99	0.75	0.59	0.48	0.37
total material lost (grams)	2.48	1.95	1.37	1.26	0.82

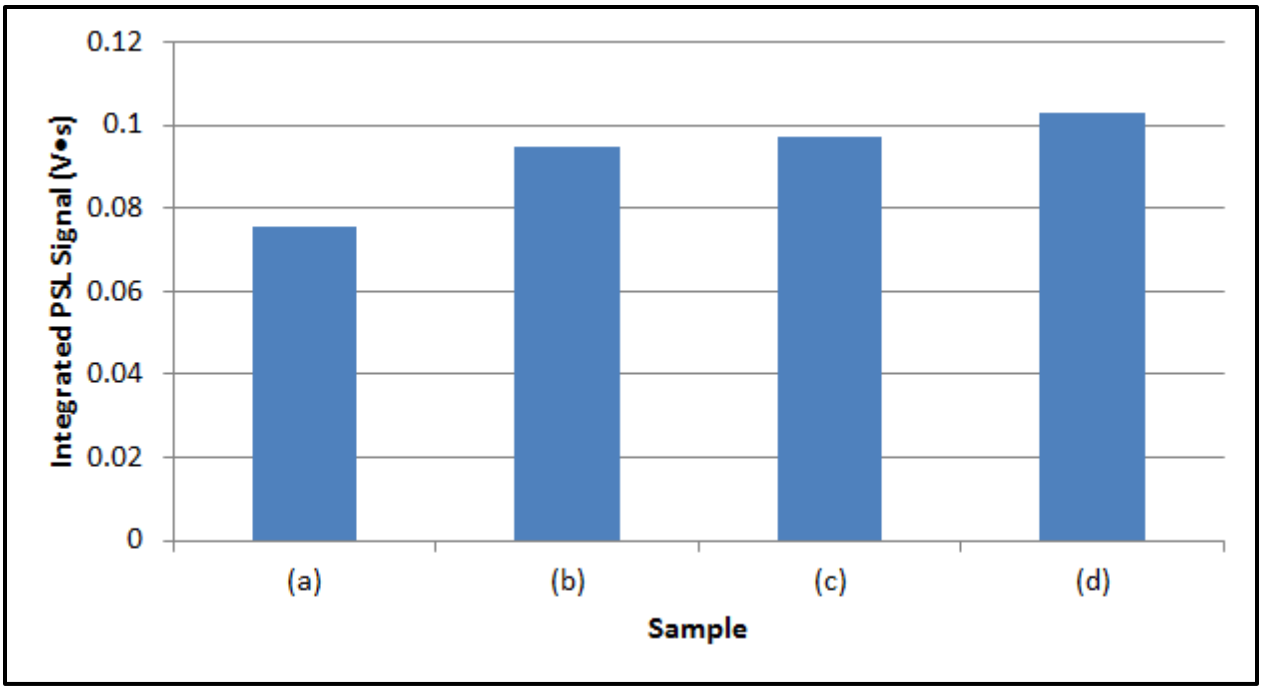

Figure A5. Integrated PSL signal for two portions of the 25% NaF sample, heat treated to 315 °C, based upon integration of the raw data over 10 seconds: (a) sample portion #1, measurement #1, (b) sample portion #1, measurement #2, (c) sample portion #1, measurement #3 , and (d) sample portion #2, measurement #1.

Figure A6. A gap phantom consisting of the assembly of two, 25.4 mm thick, 440 stainless steel plates, with one plate machined to create a series of small gaps with widths of 5.1, 10.2, 25.4, 50.8, 101.6, 203.2, and 508.0 µm between the two plates.

VITA

Russell Lee Leonard was born in Columbia, Tennessee on June 14, 1973. He was raised in Lewisburg, TN where he graduated from Marshall County High School in 1991. He graduated from Tennessee Technological University with a Bachelor of Science Degree in Mechanical Engineering in 1995. After twelve years working as a project engineer in the die casting industry, he returned to school at the University of Tennessee Space Institute in 2009 to pursue a Master's Degree in Materials Science and Engineering. After obtaining his Master's Degree, Leonard was hired full-time by the institute, working as a research associate, while pursuing a Doctor of Philosophy Degree in Biomedical Engineering.